

Aligned Ion Implantation
using
Scanning Probes

Dissertation
zur Erlangung des Doktorgrades
der Naturwissenschaften

vorgelegt beim Fachbereich Physik
der Johann Wolfgang Goethe - Universität
in Frankfurt am Main

von Arun Persaud
aus Frankfurt am Main

Frankfurt am Main und Berkeley (Kalifornien)

2006-12-12

vom Fachbereich Physik der Johann Wolfgang Goethe - Universität
als Dissertation angenommen.

Dekan: Prof. Dr. Wolf Aßmus

Gutachter: Prof. Dr. Horst Schmidt-Böcking und
Prof. Dr. Reinhard Dörner

Datum der Dissertation:

Abstract

A new technique for precision ion implantation has been developed. A scanning probe has been equipped with a small aperture and incorporated into an ion beamline, so that ions can be implanted through the aperture into a sample. By using a scanning probe the target can be imaged in a non-destructive way prior to implantation and the probe together with the aperture can be placed at the desired location with nanometer precision.

In this work first results of a scanning probe integrated into an ion beamline are presented. A placement resolution of about 120 nm is reported.

The final placement accuracy is determined by the size of the aperture hole and by the straggle of the implanted ion inside the target material. The limits of this technology are expected to be set by the latter, which is of the order of 10 nm for low energy ions.

This research has been carried out in the context of a larger program concerned with the development of quantum computer test structures. For that the placement accuracy needs to be increased and a detector for single ion detection has to be integrated into the setup. Both issues are discussed in this thesis.

To achieve single ion detection highly charged ions are used for the implantation, as in addition to their kinetic energy they also deposit their potential energy in the target material, therefore making detection easier. A special ion source for producing these highly charged ions was used and their creation and interactions with solids of are discussed in detail.

Contents

1	Introduction	1
2	Motivation	3
2.1	Quantum Computers	3
2.1.1	The power of quantum computers	4
2.1.2	The Deutsch-Josza algorithm	4
2.2	Requirements	6
2.3	The Kane Proposal	7
2.4	Developments & Further Reading	9
3	Highly Charged Ions	11
3.1	The Electron Beam Ion Trap	11
3.1.1	A short historical review	11
3.1.2	How it works	12
3.1.3	The beamline	16
3.1.4	Charge separation	17
3.1.5	Emittance	18
3.1.6	Summary	19
3.2	Interactions with Solids	20
3.2.1	Above surface relaxation - The classical over the barrier model	20
3.2.2	Below surface relaxation	23
4	Scanning Probe Microscopes	27
4.1	The AFM	28
4.1.1	Optical readout	28
4.1.2	Standard modes of operation	28
4.1.3	Piezo-resistive readout	30
4.2	The AFM setup	31
4.3	Cantilevers	33
4.3.1	Piezo-resistive cantilevers	33

4.3.2	Tips	34
4.3.3	Holes	34
4.4	Operation	36
4.5	Characteristics	37
4.5.1	Noise considerations	37
4.5.2	Vertical resolution	40
4.5.3	Lateral resolution	44
4.5.4	Drift	44
4.5.5	Tip lifetime	45
4.6	Summary	47
5	Experimental Setup	49
5.1	Final Beamline Section	49
5.2	Sample Holder and Sample	50
5.2.1	Resist	51
5.3	Additional Ion Source	52
5.4	The Experiments	52
6	Lithographic Results	55
6.1	Lithographic Patterns in Different Resists	55
6.1.1	PMMA	55
6.1.2	HSQ	56
6.1.3	Beam shape	56
6.1.4	Higher resolution, smaller features	57
6.2	Highly Charged Ions	59
7	Outlook	63
7.1	Integrating Single Ion Detection	63
7.1.1	Secondary electrons	63
7.1.2	Transistors	66
7.2	Possible Improvements of the Scanning Probe	67
7.2.1	Vibration isolation	68
7.2.2	Lock-in read-out	68
7.2.3	Non-contact mode	68
7.2.4	Smaller feature size	68
8	Similar Work & Future Developments	71
8.1	Scanning Probes without Ion Beams	71
8.1.1	Material deposition	71
8.1.2	Localized etching	72
8.2	Scanning Probes with Ion Beams	72

8.2.1	Cluster jet	72
8.2.2	Single atoms via ion traps	72
9	Conclusions	73
10	German Summary — Zusammenfassung	75
10.1	Einführung und Motivation	75
10.2	Hochgeladene Ionen	76
10.3	Rasterkraftmikroskop	77
10.4	Experimenteller Aufbau	78
10.5	Ergebnisse	79
10.6	Ausblick	79
A	Spin measurements on implanted samples	81
A.1	Quick Review of some ESR Basics	82
A.2	Measurements and Results	83
	List of Figures	87
	List of Tables	91
	Bibliography	93
	Acknowledgments	99
	Curriculum Vitae	101

Acronyms

AC alternating current

AFM Atomic Force Microscope

CMOS Complementary Metal Oxide Semiconductor

ECR Electron Cyclotron Resonance

EBIS Electron Beam Ion Source

EBIT Electron Beam Ion Trap

EBL Electron Beam Lithography

ESR Electron Spin Resonance

FIB Focused Ion Beam

FWHM full width half maximum

HCI highly charged ion

HSQ hydrogen silsesquioxane

LBNL E. O. Lawrence Berkeley National Laboratory

LLNL Lawrence Livermore National Laboratory

MCP multi-channel plate

MIBK methylisobutylketone

MOSFET Metal Oxide Semiconductor Field Effect Transistor

NCEM National Center for Electron Microscopy

NIST National Institute of Standards and Technology

PMMA	polymethylmethacrylate
PMT	photomultiplier tube
QC	quantum computer
qubit	quantum bit
rms	root-mean-square
IBIC	ion beam induced charge
SEM	Scanning Electron Microscope
SET	Single Electron Transistor
SIMS	Secondary Ion Mass Spectroscopy
SRA	Spreading Resistance Analysis
SPM	Scanning Probe Microscope
STM	Scanning Tunneling Microscope
TEM	Transmission Electron Microscopy
TMAH	tetramethylammonium hydroxide
UCB	University of California, Berkeley

Chapter 1

Introduction

Ion implantation has become a very standard and well understood process. It has many applications, the most significant being in the silicon industry. However, although transistors are getting smaller and smaller, the implantation is carried out as a bulk implant with the number of ions implanted into a certain region following a Poissonian distribution. It would be desirable to be able to control the number and position of implanted ions or even to be able to implant only a single ion. The moment single ions/atoms can be placed at a precise location a whole new plethora of applications becomes thinkable. One of the most prominent ideas involving single atoms placed at precise positions inside a target material is a quantum computer, realized by using single atoms placed into a silicon crystal.

The field of quantum computation began in 1980 when Benioff introduced *quantum Turing machines* [Benioff, 1980]. Manin [Manin, 1980] and Feynman [Feynman, 1982] discussed the use of a quantum computer (QC) to simulate physical systems. However, only after Peter Shor found a quantum algorithm to factorize large numbers [Shor, 1994, Shor, 1997], did the field of quantum computation receive a lot of attention. Many different proposals for building a quantum computer were put forward (for example [Cirac and Zoller, 1995, Kane, 1998]) and even implemented (for example [Vandersypen *et al.*, 2001, Gulde *et al.*, 2003]), but the building of a scalable quantum computer has not yet been achieved.

The program at E. O. Lawrence Berkeley National Laboratory (LBNL) (where the work presented here was carried out) focuses on building prototype devices for solid state quantum bits (qubits) in silicon.

This work describes the setup of an ion implanter combined with a scanning probe for aligned ion implantation with the goal of single ion implantation. The basic idea of operation is as follows: highly charged ions (HCIs) are transported through a very small beam-limiting aperture (which will be

responsible for the placement accuracy). The alignment of the target with the hole is achieved by an integrated Scanning Probe Microscope (SPM).

As with many projects the work described in this thesis is a group effort. Nevertheless, the results shown here (if not stated otherwise in the text) have been obtained by my own effort. Other people who should be mentioned at this point are: Thomas Schenkel for starting the project, doing all the Focused Ion Beam (FIB) processing and in general giving lots of positive input on many issues; Frederic Gicquel for doing most of the design work; Ivo Rangelow for invaluable tips on setting up an Atomic Force Microscope (AFM), and our technicians Tom McVeigh, Steve Wilde, Jerry Fischer and Paul Wong.

The thesis is organized as follows: First the motivation is given, briefly reviewing the basic ideas and requirements of a solid state quantum computer. Then the two main components of the ion implanter at LBNL, HCIs and the SPM, are presented. Next the complete setup for the experiment is described followed by results and discussion. An outlook on future experiments and towards implementing single ion detection is given, followed by a brief look at the work undertaken by other groups. Finally, the thesis is summarized and conclusions are drawn.

Chapter 2

Motivation

This thesis is strongly motivated by the task of building a test device for solid state quantum computing. Although the work presented here is just one of many steps towards a solid state quantum computer and many other challenges still lie ahead, I would first like to take the time to present the larger concept behind our project.

This chapter will give a very brief overview of quantum computing and the solid state approach leading to the project at E. O. Lawrence Berkeley National Laboratory (LBNL). It will present a quantum computing scheme requiring the placement of *single* ions at precise locations, which is the reason for investigating precise ion implantation.

2.1 Quantum Computers

The field of quantum computing began in the early 1980s with Benioff theorizing about quantum mechanical Turing machines [Benioff, 1980] and Feynman showing that a computer based on the principles of quantum mechanics would be able to simulate or solve quantum mechanical problems better than a classical computer [Feynman, 1982]. In the mid 1980s Deutsch published a paper [Deutsch, 1985] describing the first quantum algorithm that solved a problem which cannot be solved with the same efficiency on a classical computer. The breakthrough then came in 1994 with Shor’s algorithm for finding prime factors of (large) integers [Shor, 1994, Shor, 1997], which can be seen as a “killer” application for QCs, since most modern encryption codes are based on the fact that precisely this problem is very hard to solve. Afterwards further algorithms were found which run better on a QC, but Shor’s algorithm is still the most prominent one, and the one with the most drastic increase in speed compared to a classical computer. From a physicist’s point

of view, however, the ability to simulate quantum systems effectively seems to be more appealing [Feynman, 1982, Aspuru-Guzik *et al.*, 2005].

2.1.1 The power of quantum computers

There are several factors distinguishing a QC from a classical one. The most important ones are the following:

A QC uses qubits which can be in a superposition state such as $\frac{|0\rangle+|1\rangle}{\sqrt{2}}$, whereas a classical computer can only be in one of the states 0 or 1. As a result of this, when evaluating a function with a QC it might be enough to prepare an input state that is a superposition of different input values and then only calculate the function once to obtain an output state that consists of a superposition of several different function values. This is in contrast to a classical computer, where different function values have to be calculated. Furthermore quantum states can be entangled which is a feature of quantum mechanics without a classical analogy.

For a QC any function that needs to be calculated has to have a representation as a unitarian matrix and therefore computation turns out to be reversible which is something not encountered in classical computing.

At the end of the computation, when the quantum state is measured, only one state out of a superposition of states is measured. Thus one could think that although with a QC one can make use of what is called *quantum parallelism* (to calculate many function values via just one evaluation of that function by feeding in a superposition of states), one can never measure more than one result of that evaluation. That this is not true will be shown in the following.

2.1.2 The Deutsch-Josza algorithm

As an example I will discuss the Deutsch Josza algorithm as presented in [Nielsen and Chuang, 2000, p. 34]. Given a function f defined as:

$$f : \{0, 1, \dots, 2^n - 1\} \mapsto \{0, 1\} \quad n \in \mathbb{N}, \quad (2.1)$$

which is either constant for all input values or has a balanced outcome (meaning the results 0 and 1 each appear for 50% of the input values), the algorithm solves the problem of finding out which one of these two possibilities is the case.

For an n -bit input value one would need to evaluate the function $2^{n-1} + 1$ times to be able to answer this question classically without doubt. Let us see how fast a QC can answer this.

The circuit diagram for the algorithm is shown in Figure 2.1. The diagram is to be read from left to right, showing the input states on the left and the output on the right. Two different *gates* are used: The one-qubit Hadamard gate $\boxed{\text{H}}$ which is defined as:

$$\begin{aligned} |0\rangle &\mapsto \frac{|0\rangle + |1\rangle}{\sqrt{2}} \\ |1\rangle &\mapsto \frac{|0\rangle - |1\rangle}{\sqrt{2}} \end{aligned} \quad (2.2)$$

or in a more compact notation

$$H|x\rangle = \sum_{z \in \{0,1\}} \frac{(-1)^{xz} |z\rangle}{\sqrt{2}}. \quad (2.3)$$

And a many-qubit gate U_f , which performs the following evaluation:

$$|x\rangle \otimes |y\rangle \mapsto |x\rangle \otimes |y + f(x)\rangle. \quad (2.4)$$

The state $|x\rangle$ is defined as $|x\rangle = |x_0 x_1 x_2 \dots x_{n-1}\rangle$, that is it is made out of n qubits. Let us now go through the computation of the algorithm and have

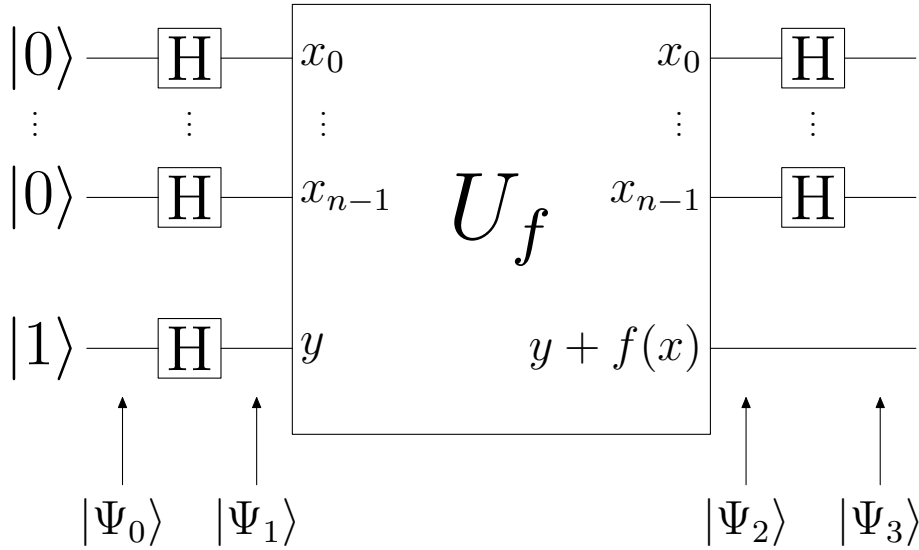


Figure 2.1: Circuit diagram for the Deutsch-Josza algorithm.

a look at the quantum state Ψ_i at different stages during execution. The algorithm starts with an input state of

$$|\Psi_0\rangle = |0 \dots 0\rangle \otimes |1\rangle. \quad (2.5)$$

Then the Hadamard gates are used to translate this state into

$$|\Psi_1\rangle = \sum_{x \in \{0,1\}^n} \frac{|x\rangle}{\sqrt{2^n}} \otimes \frac{|0\rangle - |1\rangle}{\sqrt{2}}. \quad (2.6)$$

With $U_f|x\rangle \otimes \frac{|0\rangle - |1\rangle}{\sqrt{2}} = -1^{f(x)}|x\rangle \otimes \frac{|0\rangle - |1\rangle}{\sqrt{2}}$ one can calculate the step invoking the U_f gate

$$|\Psi_2\rangle = \sum_{x \in \{0,1\}^n} \frac{(-1)^{f(x)}|x\rangle}{\sqrt{2^n}} \otimes \frac{|0\rangle - |1\rangle}{\sqrt{2}}. \quad (2.7)$$

Using equation (2.3) the final Hadamard gates result in

$$|\Psi_3\rangle = \sum_{z \in \{0,1\}^n} \sum_{x \in \{0,1\}^n} \frac{(-1)^{x \cdot z + f(x)}|z\rangle}{2^n} \otimes \frac{|0\rangle - |1\rangle}{\sqrt{2}}. \quad (2.8)$$

In the final equation $x \cdot z$ is to be understood as the bitwise inner product, that is $x \cdot z = \sum_{i=0}^{n-1} x_i z_i$.

The last state already holds the answer to the question of whether the function f is balanced or constant: If the final state of the input register $|x\rangle$ is measured, the amplitude of measuring $|0 \dots 0\rangle$ is given by

$$\sum_{x \in \{0,1\}^n} \frac{(-1)^{x \cdot z + f(x)}}{2^n} = \sum_{x \in \{0,1\}^n} \frac{(-1)^{f(x)}}{2^n}. \quad (2.9)$$

Therefore if the function f is constant the amplitude for measuring zeros in all input registers is unity and if the function is balanced the amplitude will be zero, which means that one of the other possible outcomes must have a non-zero probability. Therefore to decide what kind of function f is, all that needs to be done is to measure the input registers. Instead of evaluating the functions $2^{n-1} + 1$ times as in the worst case classical scenario, we only need to calculate it once.

2.2 Requirements

To build a working QC several requirements have to be met. The criteria have been summarized by DiVincenzo [DiVincenzo, 2000]:

- A scalable physical system with well characterized qubits
i.e. being able to build enough qubits and address them all individually.

- The ability to initialize the system to a known state
e.g. set all qubits to $|000\dots\rangle$.
- The decoherence times of the relevant system need to be much longer than the gate operation time
i.e. all necessary operations for an algorithm must be performed before quantum information is lost due to decoherence. Due to the fact that error correction codes can be applied, the current threshold to achieve usable quantum computation is set by being able to do 10^4 gate operations before the state would normally decohere.
- A universal set of gates
i.e. being able to construct any unitarian matrix to an adequate precision by using the gates available. A one-qubit gate in combination with a two-qubit gate can already be *universal*.
- A way to measure single qubits
i.e. the result of the computation must be able to be read out.

Most of these points sound very simple and basic, but nevertheless up to now no implementation of a QC has been able to fulfill all of them. All working qubit schemes fail because of the lacking scalability. The best hope for scalability is given by a solid state approach in silicon, but for this the readout and manipulation of qubits has unfortunately not yet been achieved.

2.3 The Kane Proposal

As mentioned in the last section a QC built in silicon would be desirable. The main reason behind this is that it is believed that once a single or two-qubit solid state QC has been demonstrated it will be relatively easy to build a computer with many qubits. This is mainly due to the fact that silicon has been the standard workhorse of the computer industry over the last decades and is therefore very well understood and the tools for mass production are readily available. Apart from scalability issues, silicon also lends itself to quantum computing because silicon crystals can be created spin free, consisting of only one isotope ^{28}Si and therefore qubits in silicon can have a very long decoherence time [Schenkel *et al.*, 2005, Tyryshkin *et al.*, 2003].

In 1998 Kane proposed a solid state QC-scheme utilizing the nuclear spin of phosphorus atoms as qubits in a silicon matrix [Kane, 1998], receiving a lot

of attention in the field. Several years and many publications later, Kane's first proposal is no longer valid in its original version, but it still shares many similar ideas with current proposals and shows the basic concept. Kane's idea

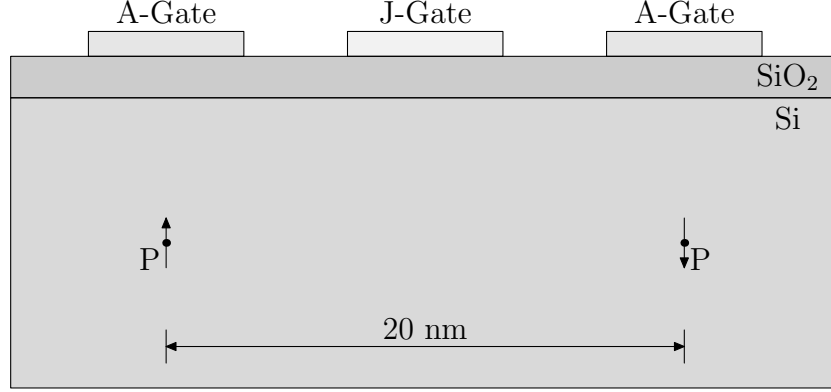


Figure 2.2: Kane's proposal for a solid state quantum computer using phosphorus spins in silicon. A magnetic field is used to address the spin states and top gates are used to control the interaction.

featuring the phosphorus atom nuclear spin qubits is presented in Figure 2.2. Phosphorus is chosen for several reasons, the most important one being that the nuclear spin of the ^{31}P phosphorus atom has a very long decoherence time and as a two level system is therefore well suited to store binary information. Natural phosphorus also only exists as one isotope, so that no extra selection has to be performed, and it is convenient for silicon processes as it is one of the standard donor materials in the computer industry. Furthermore, it is a group V element, which means it is an electron donor in silicon and this extra electron is used in Kane's scheme to provide a mechanism for two or more qubits to interact.

To build a QC for this scheme phosphorus atoms have to be placed at precise locations in the silicon material. The silicon needs to be isotopically pure to avoid ^{29}Si as a source of decoherence due to coupling of the qubits to randomly located nuclear spins. In addition gates have to be placed on the silicon surface above each phosphorus atom and between neighboring phosphorus atoms.

The QC needs to be run at very low temperatures (0.1-1 K), one of the reasons being that the extra electron of the phosphorus atom has to be bound to the donor, another reason being the longer decoherence time at low temperatures (see Appendix A.2). The gate on top of the atoms enables the overlap of the electron wave function with the nucleus to be changed, thereby controlling the strength of the hyperfine interaction. This is used

to transfer the quantum information from the nucleus to the electron and back. To exchange information between adjacent atoms, the information from both nuclei is transferred to the corresponding electrons and then by using the gate in between the two atoms the overlap of the wave function of the two electrons is turned on or off. Hereby an exchange interaction between neighboring electron spins can be used in a controllable fashion. The separation between two phosphorus atoms has to be small enough to allow for a direct wave function overlap, requiring a distance of about 20 nm.

The readout scheme put forward in the Kane proposal is based on spin-sensitive charge transfer followed by a charge-sensitive readout using a Single Electron Transistor (SET).

2.4 Developments & Further Reading

Since the first proposal by Kane many problems have been identified, for example concerning the spacing between two phosphorus atoms [Koiller *et al.*, 2001] which led to a refined Kane scheme [Kane, 2000, Skinner *et al.*, 2002]. Furthermore, many other schemes for a solid state QC in silicon have been proposed [Loss and DiVincenzo, 1998, Vrijen *et al.*, 2000, Friesen *et al.*, 2003, de Sousa *et al.*, 2004].

This chapter is meant as a very brief overview of quantum computation, in particular solid state quantum computing. An excellent source of further information about quantum computing and the status of different approaches (not only solid state) is the *Quantum Information Science and Technology Roadmap* [ARD, 2004]. Also the book by Nielson & Chuang [Nielson and Chuang, 2000] gives a good overview of many aspects of quantum computing.

Chapter 3

Highly Charged Ions

HCIs have an enhanced secondary electron and electron/hole pair yield when impinging on surfaces compared to singly charged ions. This makes detecting HCI hits easier. To make use of this feature a special ion source that produces HCIs is needed. An Electron Beam Ion Trap (EBIT) is very well suited for this task, since it can produce fully stripped light ions and even neon-like heavy ions. The first part of this chapter reviews the basic principles of an EBIT and data from beam analysis is shown. The rest of the chapter deals with the interaction of HCIs with solids.

Other devices that produce highly or multiply charged ions include Electron Cyclotron Resonance (ECR) sources and the Electron Beam Ion Source (EBIS), or large particle accelerators. The first two of these are not able to produce the very high charge states of heavy ions that an EBIT can and the last one requires a very large and expensive machine.

3.1 The Electron Beam Ion Trap

3.1.1 A short historical review

The first EBIT was built at Lawrence Livermore National Laboratory (LLNL) in 1986 [Levine *et al.*, 1988]. The idea came from the work of Donets *et al.* on EBIS dating back to 1969 [Donets *et al.*, 1969] and 1981 [Donets and Ovsyannikov, 1981]. Today about a dozen EBITs exist all around the world. The original purpose of the EBIT was to investigate the x-ray emission of trapped HCIs. In 1990 Schneider *et al.* developed an extraction mechanism [Schneider *et al.*, 1990] so that HCIs could be transported through a beam-line to a target area. This opened the door to study the interaction of HCIs with solid surfaces, in addition to the interactions in the trap region. Pre-

viously such studies were only possible with large particle accelerators, and for medium charge state ions with ECR sources.

A short historical description of EBISs and EBITs can be found in the paper by Donets [Donets, 1998].

3.1.2 How it works

In the following the EBIT at LBNL is described. It was originally located at LLNL, where it was known as EBIT-II, and was transferred to Berkeley in the year 2000. The description is valid for most existing EBITs. A schematic drawing of the EBIT device and the most important part, the drift tube assembly, can be seen in Figure 3.1 and Figure 3.2, respectively.

The basic idea is to trap ions in an electron beam where they are repeatedly ionized via electron impacts. To achieve the high charge states the ions have to be trapped for a sufficient length of time, the electron beam energy has to be high enough to be able to ionize inner shell electrons, and the electron density has to be high. Then there has to be a way of extracting the HCIs.

Let us now have a closer look at the machine and first follow the electrons through the EBIT.

The electrons are created by thermionic emission in a Pierce-type gun at zero potential. An anode voltage typically of 2 kV pre-accelerates the electrons and pulls them out of the electron source area, controlling the beam current. The beam then enters the main chamber containing three drift tubes which are biased at a high voltage of several kV. This voltage has two purposes: it accelerates the electrons so that they have enough energy to remove even inner shell electrons from the ions in the trap to form HCIs and it defines the beam energy of the ion beam.

A typical beam current is of the order of 50 mA. Unfortunately, the current density of a normal electron beam created in this way is not high enough to generate enough electron-ion collisions to create HCIs. Therefore the three drift tubes are surrounded by a pair of superconducting Helmholtz coils, which create a 3 T magnetic field parallel to the beam axis. This has the effect of compressing the electron beam to a radius of about $50\,\mu\text{m}$, about the diameter of a human hair, giving rise to an electron beam current density of $2000\,\text{A}/\text{cm}^2$.

In the trap area, constituting the drift tubes, the electrons interact with the ions creating HCIs as will be discussed below. After the drift tubes the electrons are decelerated and absorbed by the collector. To achieve this, the collector is biased typically at 1.5 kV and a magnetic field is applied, so that the electron beam is distributed over the whole collector area and not

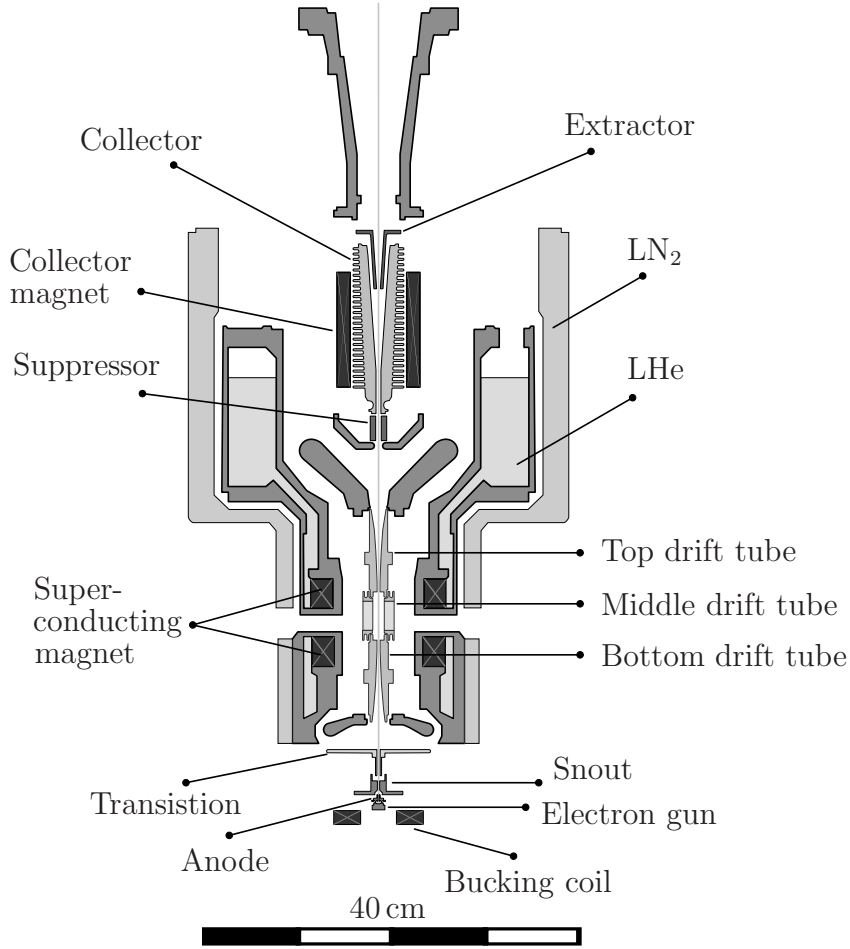


Figure 3.1: Concept of an EBIT.

absorbed at only one spot. A negatively biased extractor makes sure that only positive ions can leave the collector area and a suppressor at the entrance to the collector area is used to prevent secondary electrons reentering the trap area.

A few more elements are used to influence the electrons. A magnet is installed around the electron gun that counteracts the magnetic field from the superconducting magnet, since the magnetic field near the electron-emitting filament should be zero. Furthermore four low-current coils are mounted outside the vacuum chamber which are used to align the electron beam to the main axis.

Now we will focus on the creation of the ion beam. The desired atom species has to be transported directly to the trap region. The easiest way to do this is to inject a gas into the trap region from the side, which is obviously

the choice for elements like argon and xenon. At LBNL a particle beam can alternatively be created using an oven, which is the method used for elements such as phosphorus and bismuth. In both cases the species to be ionized enters the middle drift tube as neutral particles. When these pass through the electron beam there is a chance that they are ionized through impact ionization. Once an atom becomes positively charged it will be trapped radially by the space charge of the electron beam, so only an additional confinement in the axial direction is needed to completely trap the ion. Here the three drift tubes come into play. By biasing the middle drift tube lower than the outer ones an axial trapping potential can be generated. The trapped ions now move in the high magnetic field of the Helmholtz coils, trapped axially by the drift tubes (the trap region is about 2 cm long) and radially by the space charge of the electron beam. Many different processes can now occur: the ions can interact with the electron beam again, which can lead to another ionization process and therefore to higher charge states or just to an energy transfer (heating) of the ions. However, it is also possible for the ions to cap-

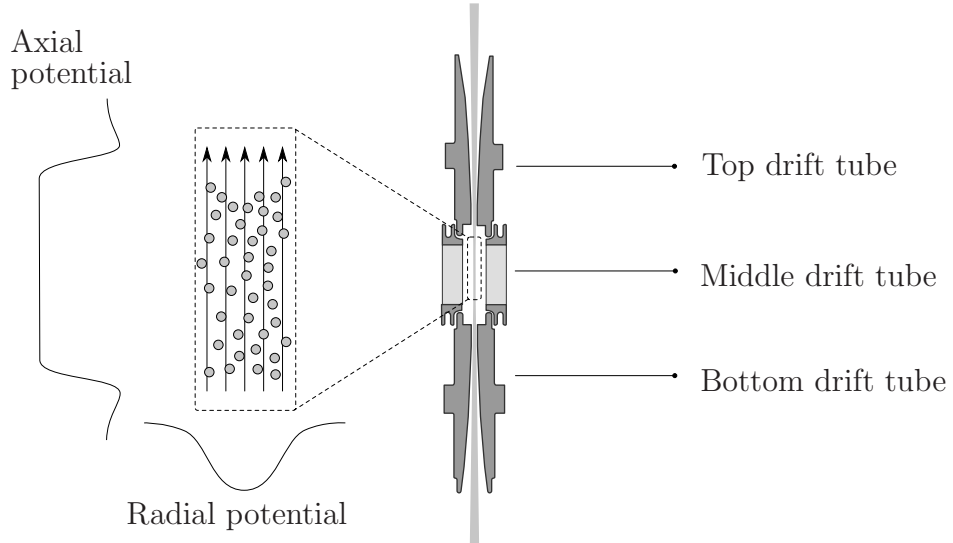


Figure 3.2: The drift tubes generating the axial trap for the ions in addition to the radial trapping by the electron beam.

ture an electron and therefore lower their charge state. Ions can exchange charge with other atoms, and if their velocity is high enough they can even escape the trap. All these processes happen continuously on different time scales and at different rates inside the trap region. The result is a charge state distribution rather than a well-defined charge state for all ions in the trap. To complicate matters further there will be other atoms/ions present in

the trap due to background gases or for example fluorine from the injection of phosphorus trifluoride (PF_3) to produce phosphorus ions. Sometimes this can have positive effects, although most of the time these other species are unwanted. One positive effect is ion evaporative cooling: ions in the trap have enough time to equilibrate their kinetic energy through ion-ion collisions. If lighter ions are present, they can achieve higher velocities and can therefore escape the trap more easily. If they escape they take away some energy from the high end of the velocity distribution and therefore cool the remaining ions. Another positive side effect comes in the analysis of charge state spectra, where the positions of peaks from background ions can be used for calibration. On the other hand every unwanted ion in the trap takes away space for ions of the desired species, since the number of ions in the trap is limited by the space charge of the electron beam and therefore any other ion species will decrease the ion beam current. To roughly estimate how many ions can be expected the space charge of the electron beam in the trap area can be calculated,

$$Q = i_e \frac{L}{v_e} \quad (3.1)$$

$$= i_e L \sqrt{\frac{m_e}{2eU}}, \quad (3.2)$$

where Q is the total negative charge in the trap area, i_e is the electron current, L the trap length (2 cm), v_e the electron velocity, e the electron charge, U the acceleration voltage and m_e the electron mass. For a 6 keV, 50 mA electron beam, the total charge in units of electron charge is about $10^8 e$, so that one can expect of the order of a few million ions per charge state in the trap. The actual number of extracted ions also depends on how often ions are extracted from the trap and how long it takes to ionize them to the desired charge state.

There are two different modes to extract the ions from the trap: pulsed mode and leaky mode. Both modes make use of the fact that the bottom drift tube (the one closer to the electron gun) is biased slightly higher than the top one, a fact that does not change the trapping characteristics. In pulsed mode the potential of the middle drift tube is raised in a short time interval above the value of the top drift tube (but below the value of the bottom one), so that all ions are pushed out of the trap area towards the top. The potential of the middle drift tube is then lowered back and new atoms will be ionized and trapped. The time the ions spend in the trap (the “*cooking*” time) can be varied to achieve a maximum in the charge state distribution for the desired species and is normally of the order of 100 ms to 3 s. In leaky mode the middle drift tube is not pulsed and the ions in the

trap can only leave when they reach a velocity which allows them to pass the top drift tube. This leads to a continuous beam of HCIs. However, in this case the ions will have a higher temperature and therefore the beam quality will be worse than in pulsed mode.

Since the ions are created at the higher positive drift tube potential, they will be accelerated on their way to the collector where they are focused by the suppressor and the extractor. They then leave the EBIT and enter the beamline, which is described in the next section.

The following textbooks [Gillaspy, 2001, Currell, 2003] give further information about the physics of EBITs.

3.1.3 The beamline

After the ions are generated they pass through an Einzel lens to focus and a deflector setup to steer the beam into an electrostatic bender. The bender

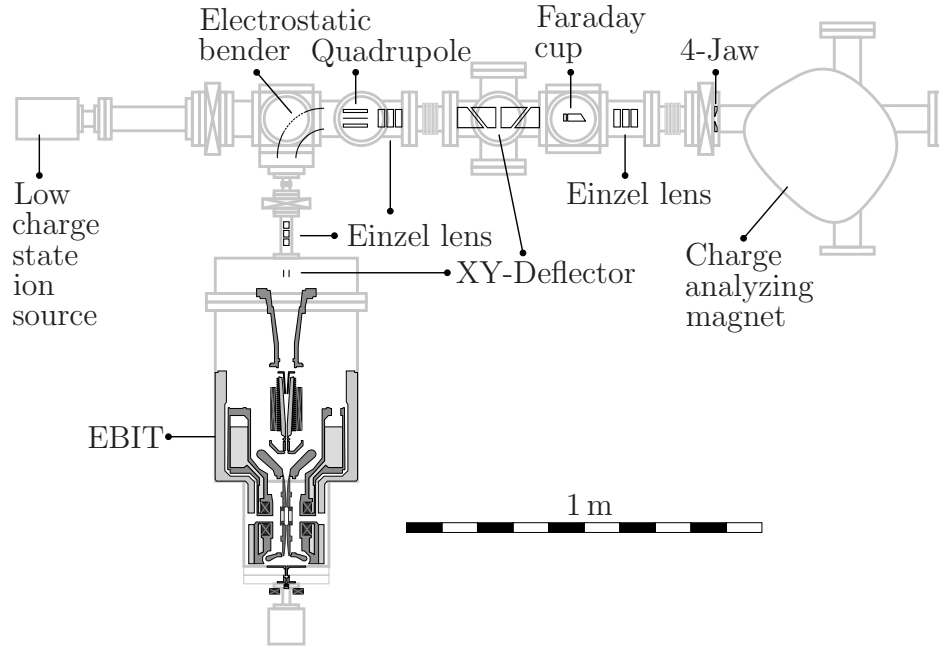


Figure 3.3: The EBIT beamline at LBNL.

consists of two parallel plates with a bend of 90° . Since this is an electrostatic element all charge states created by the EBIT will be deflected at the same rate. The outer plate also features a fine metal mesh so that if the bender is not in use a beam from another ion gun can be injected into the beamline. In the following section the beam is transported through several elements to

a bending magnet, which is used for charge state separation. These elements include a quadrupole lens, an Einzel lens, a set of deflectors, an extractable Faraday cup for beam current diagnostics, another Einzel lens to focus the beam into the magnet and a set of slits (4 jaws).

The beam then enters the analyzing magnet that can be scanned in the range of 0-0.3 T. The magnet separates the ions according to their mass-to-charge $\frac{m}{q}$ value, so that a single charge state can be selected. The selected charge state is then transported into the experiment chamber by passing through an iris, an extractable beam-profiler, a quadrupole lens and an Einzel lens, which then focuses the beam into the experiment setup. Another Faraday cup is normally mounted after the final Einzel lens, so that the beam current can be measured while scanning the magnet.

3.1.4 Charge separation

The stiffness of the beam can be calculated from the centripetal force and the Lorentz force giving:

$$Br = \frac{m}{q}v, \quad (3.3)$$

where B is the magnetic field, r the radius of curvature, m the mass of the particle, q the charge and v its velocity. For non-relativistic energies the velocity is given by

$$v = \sqrt{\frac{2qU}{m}}, \quad (3.4)$$

where U the potential used to accelerate the particles. Therefore the magnetic field is proportional to the square root of the mass-to-charge value

$$B = \frac{\sqrt{2U}}{r} \cdot \sqrt{\frac{m}{q}}. \quad (3.5)$$

By scanning the magnetic field of the bending magnet, spectra as the one in Figure 3.4 are obtained. In addition to the Faraday cup after the magnet, more sensitive detectors, for example multi-channel plates, can be used to record the beam intensity. Figure 3.4 shows that the different charge states can be distinguished clearly. The distribution of charge states depends on many parameters: the trapping time, the extraction potential (which is at the same time responsible for the energy of the electron beam), the ionization energies of the different electrons in the shells of the ion, the trap depth, the extraction mode, etc. [Schneider *et al.*, 1990, Currell, 2003, Gillaspy, 2001]. Also seen in the figure is the presence of residual gases, which can have the same or a similar mass-to-charge value as a charge state of the HCl. Most

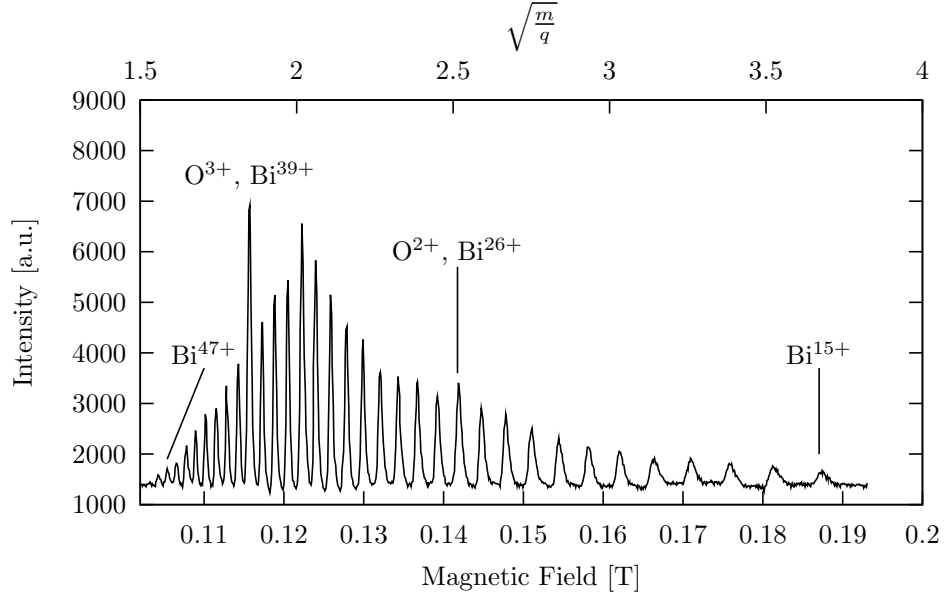


Figure 3.4: Separating different charge states of a bismuth beam extracted at 3.5 kV using the bending magnet.

of the time these are just background gases from for example water vapor or air in the beamline. Although these impurities are unwanted they can also help in calibrating the spectrum, as previously mentioned.

3.1.5 Emittance

The emittance of the ion beam was measured after the bending magnet using two knife-edges which were positioned along the beamline and could both be inserted in the same direction into the beamline, as shown in Figure 3.5. By using just one knife-edge and a detector behind it (for example a Faraday cup) the beam profile can be measured, or to be more precise the integrated beam current can be measured and the beam profile can be calculated by differentiating the measured curve. By using a second knife-edge further down the beamline the angular dependence of the beam profile can be measured and thereby an emittance plot can be created. For an Ar^{14+} beam at an extraction potential of 6.5 kV the emittance is shown in Figure 3.6. The root-mean-square (rms) value for the emittance was determined to be:

$$\epsilon_{rms} = 2.4 \pi \cdot \text{mm} \cdot \text{mrad}. \quad (3.6)$$

The normalized emittance is smaller by a factor of approximately 500, since the ions are relatively slow, at 0.2% of the velocity of light ($v = 660000 \text{ m/s}$).

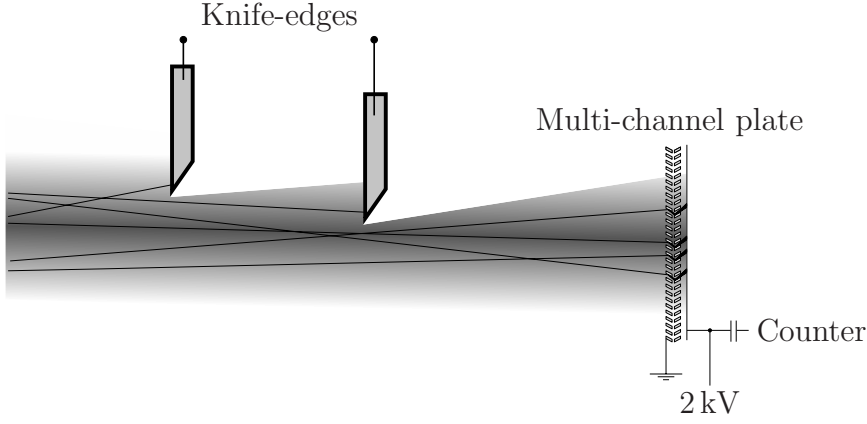


Figure 3.5: Two knife-edges are used to measure the emittance of the beam.

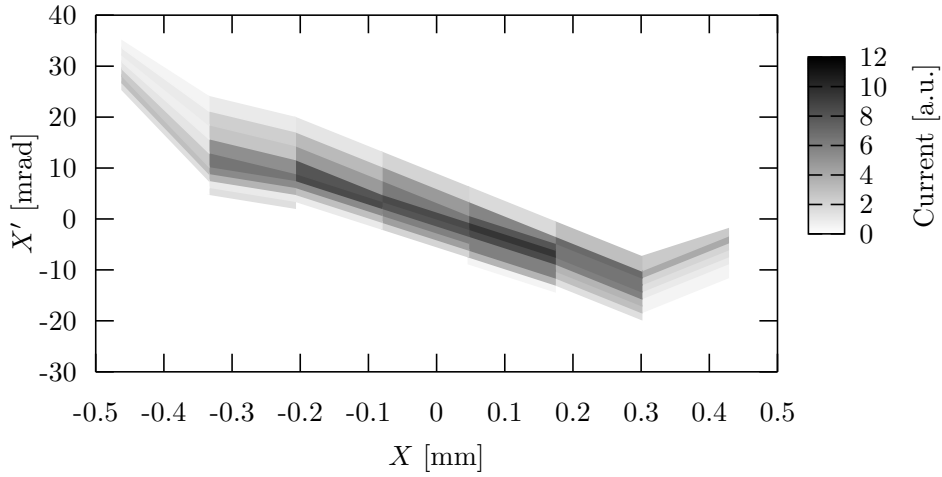


Figure 3.6: Measured emittance of an Ar^{14+} beam.

Similar values have been measured previously [Marrs *et al.*, 1998] and are characteristic for an EBIT.

3.1.6 Summary

The EBIT produces a beam of HCIs which is well suited for our purposes. The beam has a low emittance, but also a low beam current. The latter is not a problem for our setup since the ultimate goal is to implant single ions and a rate of one ion every few seconds would be sufficient.

3.2 Interactions with Solids

The interaction of a HCI with a surface is a process that is hard to describe analytically, because it is very dynamic. A quick look at some of the experimental data reveals the astonishing amount of energy that is released when a single HCI hits a surface, here is an example: a highly charged xenon ion, say Xe^{44+} , carries about 51 keV potential energy, that is the sum of all the binding energies of the 44 removed electrons. When it impacts on the surface the HCI creates a crater with a diameter smaller than 100 nm (see Section 6.2). It also deposits most of its potential energy within a few nanometers, say less than 10 nm [Schenkel, 1997]. Since the whole process only takes several femto-seconds, it gives rise to a power density of $10^{22} \text{ J/m}^3\text{s}$. Releasing this amount of energy leads to the sputtering of many secondary ions and electrons, damage in the material and x-ray and phonon production, all of the aforementioned being part of a very dynamic and complex many-body process.

Nevertheless some simple models have been proposed that actually describe part of the interaction process quite well. One of these is the *classical over the barrier model* which explains the capture of electrons into the HCI and the neutralization process that already starts above the surface. Furthermore, experimental studies and simulations have helped to understand the amount of secondary ions and electrons that are released during a HCI impact. In the following sections we will have a closer look at these processes of above surface neutralization and sputtering.

3.2.1 Above surface relaxation - The classical over the barrier model

The *classical over the barrier model* deals with the transfer of electrons from a material (or other atoms in the case of a gas target) to the HCI. The version discussed here is actually only valid for metals as the target material, since it includes the effects of image charges both from the HCI and the electron that is transferred.

Let us imagine an electron in between the HCI and the surface, as shown in Figure 3.7. This electron will see its own image charge, the potential of the incoming ion and the image charge of that ion. Without the presence of the HCI it would be attracted towards the surface by its own image charge. When the HCI is still far away from the surface and the electron the situation should be the same, but at one point the HCI will be so close to the electron that the electron will move towards the HCI instead.

For a rough estimate of this distance all three potentials can be described

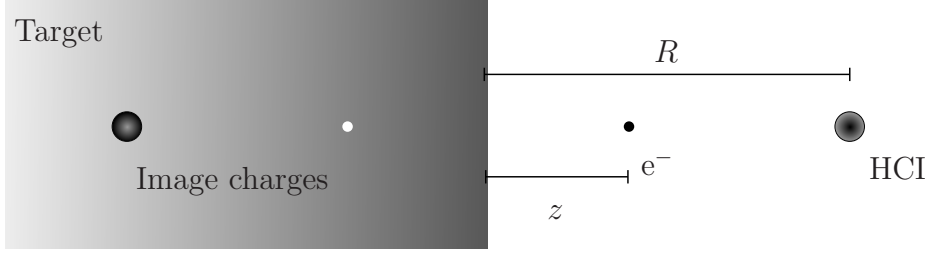


Figure 3.7: HCl above a surface.

by Coulomb potentials. The overall potential $V(z)$ will be the sum of these and will have a maximum somewhere between the HCl and the surface:

$$V(z) = -\frac{1}{4|z|} - \frac{Q}{|R-z|} + \frac{Q}{|R+z|}, \quad (3.7)$$

with Q being the charge of the HCl, R the distance of the ion to the surface and z the position of the electron with respect to the surface.

The closer the ion moves towards the surface, the smaller the absolute value of the potential maximum will become. The electrons that are available for transfer are bound in the material. The binding energy is called the *work function*, W_ϕ . For electrons to transfer from the material to the HCl the maximum value of the potential must be larger than the work function. The distance of the ion from the surface at which these two energies are equal is called the *critical distance*, d_c . To calculate the critical distance the maximum of the potential at z_{max} needs to be calculated first. With it we can use the following equation to obtain the critical distance

$$V(z_{max}) = W_\phi. \quad (3.8)$$

Once this condition is met, the electrons in the material will not see the maximum potential as a barrier between the material and the HCl anymore and can transfer easily to the HCl. This normally happens a few nm above the surface. The situation where the electrons can transfer into the HCl is shown in Figure 3.8. For HCl's one can assume $Q \gg 1$ and with this the following approximation can be calculated from Equation (3.7):

$$z_{max} \simeq \frac{R}{\sqrt{8Q-1}}. \quad (3.9)$$

Inserting this back into Equation (3.7) and using Equation (3.8), one obtains

$$d_c \simeq \frac{\sqrt{8Q-1}}{2W_\phi} \approx \frac{\sqrt{2Q}}{W_\phi}. \quad (3.10)$$

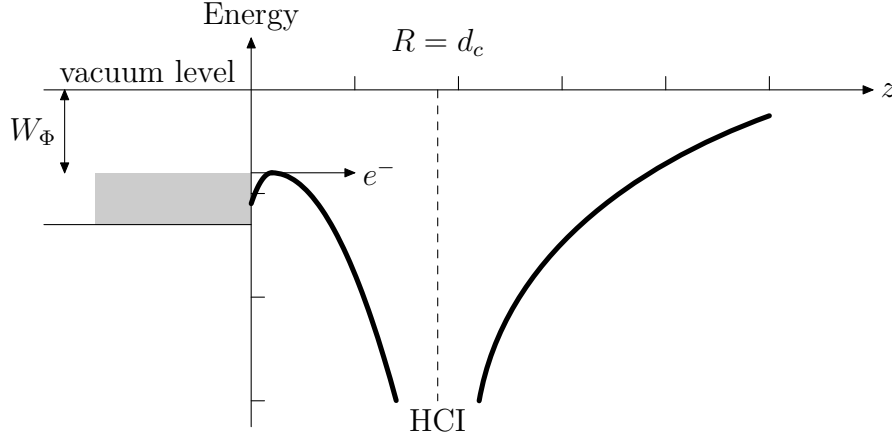


Figure 3.8: Potential distribution for a HCl at the critical distance for resonant electron capture close to a metal surface.

In principle electrons can also tunnel through the barrier even before the HCl has reached the critical distance, but the tunneling rates are slow in comparison with the speed of the ion approaching the surface, so that transfer over the barrier is the dominant process [Burgdörfer *et al.*, 1991].

The electrons that transfer through this channel will have an energy close to the Fermi energy of the material and therefore can only reach levels in the HCl with a similar energy. The process is also called resonant capture, for that very reason. For a typical HCl the electrons are captured into states with high quantum numbers or classically with large radii.

The HCl can only capture electrons until it is neutralized, but when this happens most of the captured electrons will be in states with high quantum numbers as just explained. Looking at the classical picture of the HCl, the ion will have some electrons close the nucleus (unless all electrons were removed when creating the HCl) and the remaining electrons will be in states with large radii. Thus there is a gap in between the two groups of electrons, which is why this state of an atom has been termed *a hollow ion/atom*, though some people prefer to call it a highly excited ion/atom.

If this hollow atom were now left undisturbed, the electrons in the excited states would relax over time either by emitting x-rays or via Auger processes, releasing an electron and therefore ionizing the atom. However, in our case the atom will also enter the material after the short time it needs to travel from the critical distance to the surface. On entering the dense material electrons are stripped back off the atom and then the ion captures more electrons until it comes to rest, completely neutralized with all electrons in their ground state.

The formulae presented in this section only give very rough estimates. The paper by Burgdörfer *et al.* [Burgdörfer *et al.*, 1991] includes a better approximation for the surface (including plasmon dispersion). It also includes rate equations and simulations for the formation of hollow atoms. Models for insulators are also available [Ducrée *et al.*, 1998, Hägg *et al.*, 1997], though the basic idea of resonant electron capture remains the same.

3.2.2 Below surface relaxation

The time the ion spends above the surface is not sufficient to fully relax the electrons, that is a hollow atom is formed which is still in an excited state possessing most of its initial potential energy. Once it hits the material, the atom relaxes into an equilibrium charge state very quickly (for our beam conditions this is mostly a singly charged ion) and finally comes to rest as a neutral particle. The whole process only takes a few femtoseconds [Schenkel, 1997] and during that time the potential energy is imparted to the ion's environment, the target material. There are many processes into which the energy can be channeled, for example, Auger electrons can carry away some of the energy. These can either escape the material and would then be counted as secondary electrons or they can pass their energy via inelastic scattering to other processes in the material. The lattice can absorb some of the energy (phonons), and in metals the electron gas can also absorb some of it (plasmons). A certain percentage of the energy will be transferred to further secondary electrons and ions can also receive enough energy to break their bonds with the lattice and leave the material. The latter leave as neutral or charged particles, even clusters of atoms can be sputtered away. Three different mechanisms have been discussed in the literature [Schenkel *et al.*, 1999b] as being responsible for the high yield of secondary particles resulting from HCI impact on surfaces.

- Defect-mediated desorption

During the interaction of the HCI with the material localized defects are formed. These can diffuse to the surface and lead to the release of neutral atoms at the surface.

- Coulomb explosion

A HCI can capture many electrons from the surface during its neutralization. If the target material is an insulator the material might not be able to supply enough electrons to the relatively small volume. If the timescale for the neutralization of this volume is too large the charged atoms in the material can repel each other, leading to a so called *Coulomb explosion*.

- Intense, ultrafast electronic excitations

Structural instabilities can also arise if enough bonds in the lattice are broken and can lead to a repulsive force between the atoms. Intense, ultrafast electronic excitations were originally modeled for femtosecond lasers, but since the energy density deposited by HCIs can exceed that from these lasers, the effect might also contribute here.

Due to a combination of these processes the secondary particle yield can be as high as, for example 150 electrons/ion for Xe^{52+} on SiO_2 [Schenkel, 1997].

The kinetic energy of the ion is normally absorbed through inelastic electronic or nuclear scattering. The first process creates electron/hole pairs and the latter displaces atoms from the lattice, creating damage to the material. However, even for nuclear stopping some energy is used to create electron/hole pairs through secondary processes (recoils). For the energy ranges of ions created with the EBIT nuclear stopping is the dominant process. For example, only at energies above 3 MeV does the electronic stopping for bismuth become more important, for phosphorus this energy lies at 100 keV. According to Biersack and Ziegler [Biersack and Ziegler, 2003], for bismuth the nuclear stopping power at an energy of 300 keV is a factor of 3-4 times greater than the electronic stopping power. A typical plot of the stopping powers is shown in Figure 3.9, in which the nuclear and electronic stopping powers for bismuth in silicon are plotted as calculated by SRIM [Biersack and Ziegler, 2003].

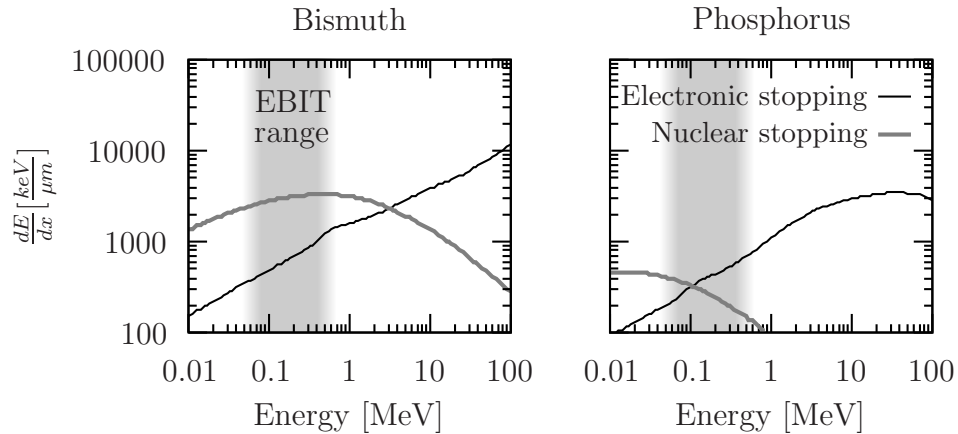


Figure 3.9: Stopping powers of bismuth and phosphorus in silicon.

The bottom line is that a lot of the potential energy of a HCI can also be used to create electron/hole pairs, even if at first the energy is channeled into other processes, for example fast electrons. The cumulative effect of these

secondary processes leads to an enhancement in the creation of electron/hole pairs compared to a singly charged ion with the same kinetic energy. Schenkel *et al.* found that for Au^{69+} about a third of the potential energy is converted into electron/hole pairs [Schenkel *et al.*, 1999a], which in that case provided an extra 60 keV towards the creation of electrons and holes. In silicon this corresponds to about 15000 electron/hole pairs.

At the end of this thesis (see Section 7.1) an experimental setup is presented that makes use of exactly this effect to detect single ions during implantation.

Chapter 4

Scanning Probe Microscopes

Scanning probes are used to examine the surface or surface properties of a material. The principle of operation is the same for all SPMs: A small very sharp tip is positioned above a surface and then scanned over an area. While scanning, a signal from the tip-surface interaction is sampled and by correlating the position with the signal a line-by-line image of a surface property can be obtained.

The first scanning probe, a Scanning Tunneling Microscope (STM), was built by Binnig and Rohrer in 1981 [Binnig *et al.*, 1982], followed a few years later by the first Atomic Force Microscope (AFM) [Binnig *et al.*, 1986]. Now many different scanning probes have been built, utilizing different signal sources. Some examples of various SPMs are listed in Table 4.1. If the signal depends on the distance of the tip to the surface, as for example for STMs and AFMs, two different modes of operation can be used: The position of the tip can be held constant so that the signal changes according to the surface properties, or a feedback loop can be applied to keep the signal constant by actively changing the distance of the tip from the surface and monitoring the changes applied. The latter is normally achieved by controlling a piezo-stage on which either the tip or the sample is mounted. Using a feedback loop has the advantage that the cantilever on which the tip is placed will experience a smaller range of distances to the surface and non-linear effects will be smaller. Crushing the tip into the surface can also easily be avoided by using a feedback loop.

In this chapter the basic principles of AFMs will be discussed, followed by the setup of the AFM used for the experiments carried out in this thesis. In addition, the fabrication of the special cantilevers used for this experiment will be briefly described. Results from the operation of the AFM will be presented, that show the current limitations of the setup.

Type of SPM	Signal source	Property measured
Scanning Tunneling Microscope	tunneling current between tip and surface	density of states
Atomic Force Microscope (contact mode)	deflection of the cantilever	topography
Atomic Force Microscope (non-contact mode)	change in resonance frequency	topography
Scanning Capacitance Microscope	capacity between tip and sample (separated by e.g. an oxide layer)	carrier concentration
Magnetic Force Microscope	deflection of the cantilever	magnetic fields at the surface

Table 4.1: Various existing SPMs (incomplete).

4.1 The AFM

4.1.1 Optical readout

The standard way to detect a change in height with an AFM is to look at the bending of the cantilever beam on which the tip is mounted, using an optical readout. To accomplish this a small laser beam is positioned so that it reflects off the back side of the beam into a segmented photo diode. To increase the signal the rear side of the beam is often coated with a metal for better laser beam reflection. If the bending of the cantilever beam changes, the laser beam will be reflected in a slightly different direction and the difference between the signals in the split photo diode is a measure of this. For small deflections the angle of deflection is proportional to the change in height. A schematic of the setup is shown in Figure 4.1.

4.1.2 Standard modes of operation

There are three standard methods of operation for AFMs: A) *Contact mode*, B) *Non-contact mode* and C) *Tapping-mode*. Some of these modes also apply to other SPMs.

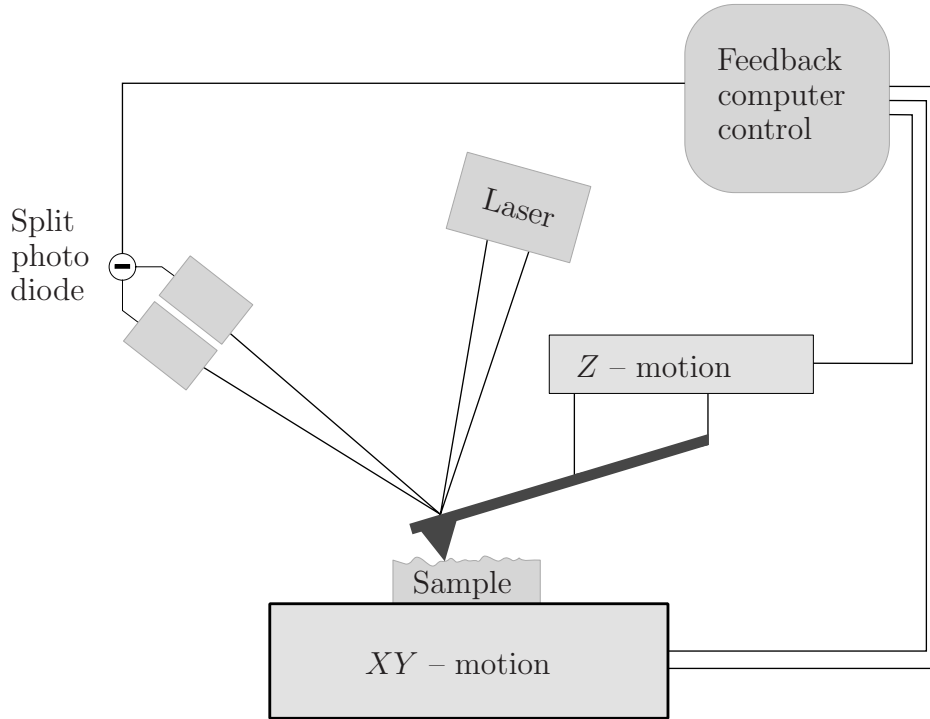


Figure 4.1: SPM setup using a laser readout.

Contact mode

In this mode the tip of the cantilever is brought into contact with the sample. While scanning the sample, the tip will be forced to move up and down according to the topography, which causes a deflection of the beam. In feedback mode the stage is moved such that the deflection of the beam will remain constant. Thus in contact mode there is a constant repulsive force between the tip and the surface. One can think of the cantilever as a spring that is preloaded, so that the tip will always stay in contact with the surface. The force that is applied can normally be set through the control unit of the AFM and is in the range of several nN. The spring constant for contact mode cantilevers is rather small, so that the cantilevers are soft and not too much pressure is applied to the sample. Typically the spring constant for contact mode cantilevers is in the range of $0.05\text{-}5\text{ N/m}$.

Non-contact mode

As the name suggests the tip does not touch the surface in this mode, but is held constantly at a few nm above the surface. To achieve this, forces such as van der Waals forces are monitored. Since these forces are normally very weak, of the order of pN, they cannot be measured directly. The trick is to measure a change in resonant frequency which can be done very precisely. To do this, the cantilever is oscillated with a small amplitude (a few nm) near its resonant frequency. The cantilever chips are therefore designed to have a sharp resonance peak. Now one can force the beam to oscillate at a frequency very close to the resonant frequency, by for example mounting the cantilever on a piezo-stage that is driven at that frequency. The narrow resonance peak means that the resulting amplitude of the oscillation depends strongly on the frequency. Since the tip oscillates very close to the surface it still feels the long range interaction of the force between the tip and the surface (force gradient), which results in a frequency shift of the resonance curve. This small shift results in a large amplitude change because of the near-resonance condition. A feedback loop can now be built that tries to keep the amplitude of the oscillation constant. The amplitude is measured in the same way as the deflection in contact mode and is then normally fed into a *Lock-In amplifier*, so that the rms-value of the oscillation is measured. Instead of measuring the frequency shift one can also use the phase of the signal for the feedback loop.

Tapping mode

Tapping mode is a combination of both of the modes just described. The cantilever is oscillated above the surface, but the distance between the tip and the surface and the amplitude of oscillation are chosen such that the tip touches the surface once during each cycle. This way the tip is not dragged across the surface during scanning which excludes frictional forces and in addition potential damage on the sample is less likely. On the other hand the amplitude of the oscillation can be quite large which makes feedback control easier and more stable.

4.1.3 Piezo-resistive readout

In our setup space requirements made it hard to implement a laser deflection scheme and the fact that the beamline is under vacuum also makes the integration of a laser and the necessary optics more difficult. Therefore an alternative approach to reading out the deflection signal of the cantilever is

utilized. Piezo-resistive sensors in the cantilever are used to sense the stress in the material when the cantilever is deflected. One way to read out the piezo-resistive resistors is with a Wheatstone bridge, which converts a change in resistance into a voltage difference. This technique was first used by Tortonese *et al.* [Tortonese *et al.*, 1991] and the method has been improved by Rangelow *et al.* [Rangelow *et al.*, 1996] by implementing the complete Wheatstone bridge into the cantilever itself. The integration of the Wheatstone bridge reduces thermal drift and the use of four piezo-resistive sensors gives a stronger signal.

The piezo-resistive readout has the advantage that no optics are needed and therefore no alignment of optical components has to be carried out. In addition, it allows for a very compact setup. Piezo-resistive sensors would also allow for a parallel setup of cantilevers to allow for a faster scan speed or a larger scan area. Furthermore, the accuracy achieved with piezo-resistors is the same as with a laser readout.

In the following the piezo-resistive cantilevers and the setup for the SPM will be discussed.

4.2 The AFM setup

A schematic of the setup is shown in Figure 4.2. The Wheatstone bridge is biased at 1 V. The signal from the Wheatstone bridge is fed into a fast settling pre-amplifier (INA110). The pre-amplifier is mounted in vacuum very close to the signal source and results in 10-fold amplification. This is done to prevent electronic pickup of noise which would otherwise interfere with the signal and by placing the pre-amplifier as close to the signal source as possible a better signal-to-noise ratio is achieved. The signal is then taken outside the vacuum chamber to a second low-noise pre-amplifier (Stanford model SR560). The SR560 has a gain between 1 and 50000 and the ability to add high-pass and low-pass filters to the signal processing at different cut-off frequencies. It also has the option of adding an offset to the amplified signal, which is important to zero the Wheatstone bridge. Both pre-amplifiers and the Wheatstone bridge are powered by batteries to avoid 60 Hz noise.

The signal itself is then fed into the feedback loop which is provided by a RHK SPM-1000. A piezo-flexure nanopositioner from Physical Instruments (PI) with $100\text{ }\mu\text{m} \times 100\text{ }\mu\text{m} \times 10\text{ }\mu\text{m}$ travel and nanometer resolution is controlled by the feedback loop to keep the deflection signal constant at a given set-point.

The sample is mounted onto the nanopositioning stage. The cantilever is mounted on a flexure stage with X, Y and Z motion for coarse positioning

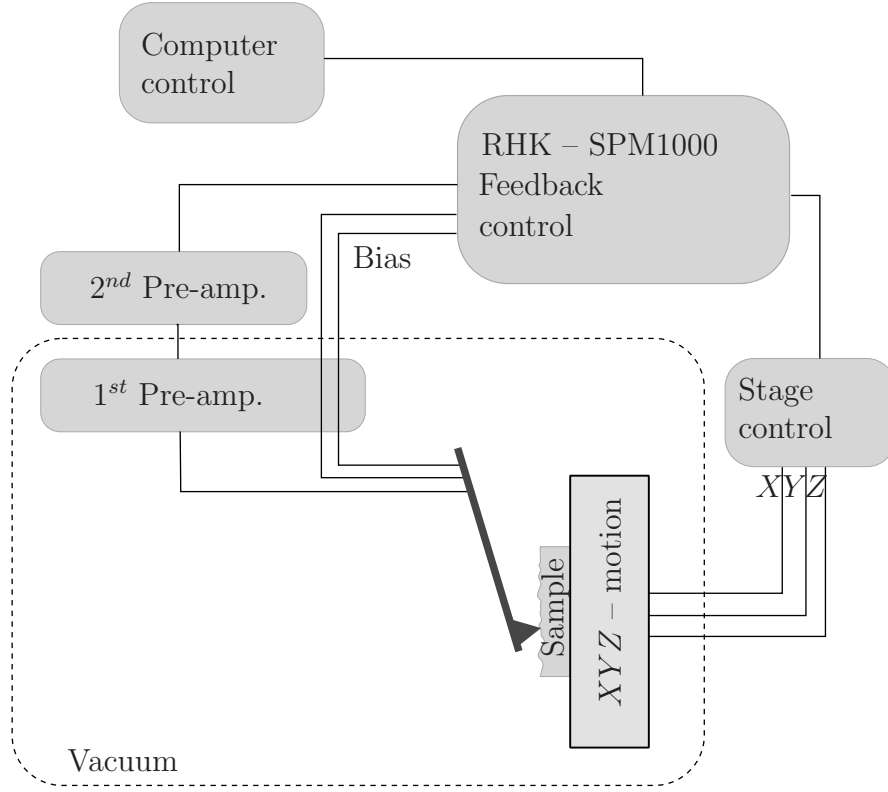


Figure 4.2: Schematic setup of the piezo-resistive SPM.

and approach above the sample. During scans the cantilever is kept at a fixed position. To prevent the cantilever from interfering with the sample it is mounted at 10° , so that only the tip touches the sample even if the sample or the cantilever is not completely flat or mounted incorrectly. A photograph of the setup can be seen in Figure 4.3. It shows the last beam-limiting aperture before the cantilever, the cantilever with a tip, and the target holder that is mounted on the piezo stage. The target holder is made so that it can be easily dismantled without removing the whole stage. As can be seen, the space between the last beam aperture and the target has been kept small. This was done so that a beam decelerating scheme might be added in the future to be able to implant with very low kinetic energy to keep the straggling of the implanted ion within the target material to a minimum.

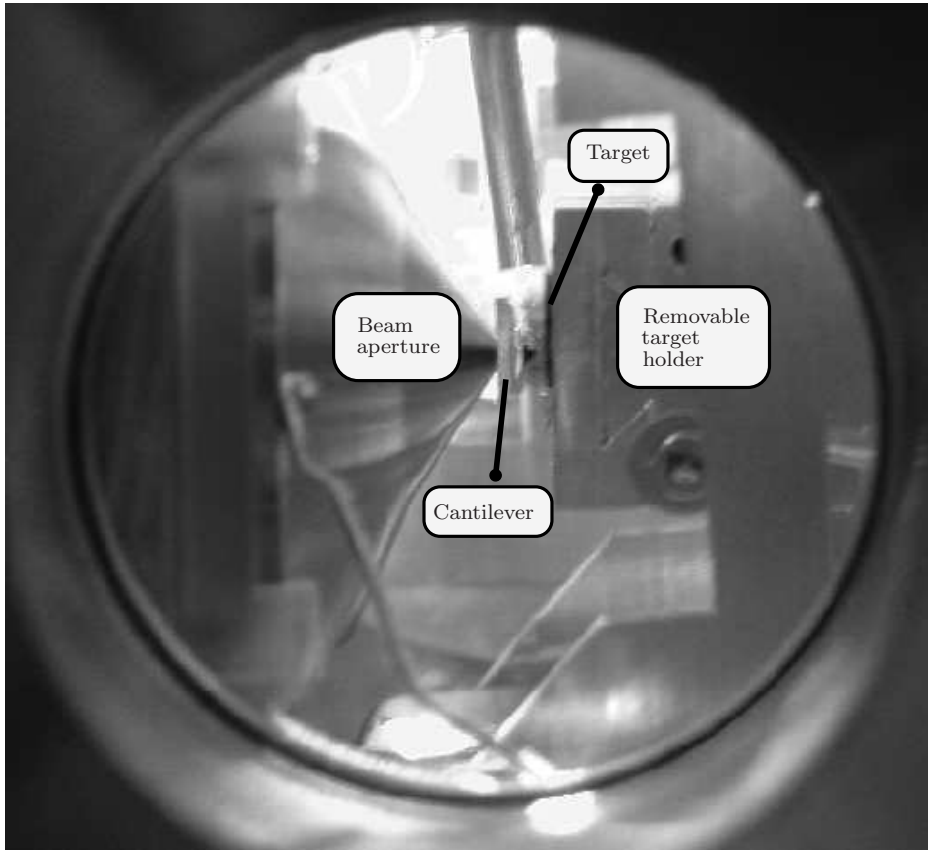


Figure 4.3: Photo of the SPM setup in the 8 in. cube taken through one of the viewports in the cube.

4.3 Cantilevers

4.3.1 Piezo-resistive cantilevers

The piezo-resistive cantilevers used are made by Rangelow *et al.* at the University of Kassel, Germany. They are produced by standard Complementary Metal Oxide Semiconductor (CMOS) processing of silicon wafers. The complete fabrication steps are described in [Gotszalk *et al.*, 2000]. Standard cantilevers used in our experiment have dimensions of $600\text{ }\mu\text{m}$ in length, $100\text{ }\mu\text{m}$ in width and a thickness of $5\text{ }\mu\text{m}$. The calculated force sensitivity of these cantilevers is $2.2\text{ }\mu\text{V}/\text{nm}$, using a Wheatstone bridge readout scheme.

The piezo-resistive elements are placed at the base of the cantilever beam, where the stress introduced by bending the beam is extreme and therefore the largest signal can be measured. Also, by building the Wheatstone bridge into the cantilever the thermal stability (all sensors in the same area) and

sensitivity (four resistors instead of one) could be increased in comparison to other piezo-resistive designs which utilize an external bridge.

The cantilevers were designed without an integrated tip which would have presented an additional lithography step and complicated the following processing steps. In the next section the different methods used to add a tip are discussed.

4.3.2 Tips

Two different techniques for adding sharp tips to the cantilevers were implemented. The first is to grow tips using ion beam assisted deposition with a FEI *Strata 235* Dual Beam Focused Ion Beam (FIB) at the National Center for Electron Microscopy (NCEM) at LBNL. Since the cantilevers are mounted in the AFM at an angle and the tips are not grown right at the edge of the beam, the tips need to have a certain height. This makes growing tips with a FIB a time-consuming task.

To produce sharp tips, first a wide base was deposited and on top of that a narrow pole was grown. An example can be seen in Figure 4.4.

Another possibility is to glue the tip of a commercially available cantilever onto a piezo-resistive one. Due to the larger dimension of the piezo-resistive cantilever there is enough space available to do this. The beam of a commercial cantilever is broken off and the tip together with part of the old beam is then glued onto the piezo-resistive cantilever with silver epoxy. This challenging task is done in a very precise way by the group in Kassel, Germany.

The advantage of this method is to be able to use all the positive features of a commercial tip (i.e. sharpness and lifetime) without having to add extra processing steps for tip etching in the fabrication of the piezo-cantilevers. In the long run, however, including a tip into the cantilever design would be the preferred option, since glueing on tips has a rather low yield and was only used to produce good tips in a short time without having to change the fabrication process. A picture of a glued on tip can be seen in Figure 4.5, which shows the whole piezo-resistive cantilever including the Wheatstone bridge at the bottom, the beam and the glued on tip at the top.

4.3.3 Holes

In order to have an ion beam-limiting aperture, small holes in the cantilever are needed. This was also achieved using the dual beam FIB. First tests were carried out using silicon nitride membranes. Holes with a diameter of around $1\text{ }\mu\text{m}$ are drilled and then closed down to several nanometers in diameter using ion beam assisted deposition of platinum.

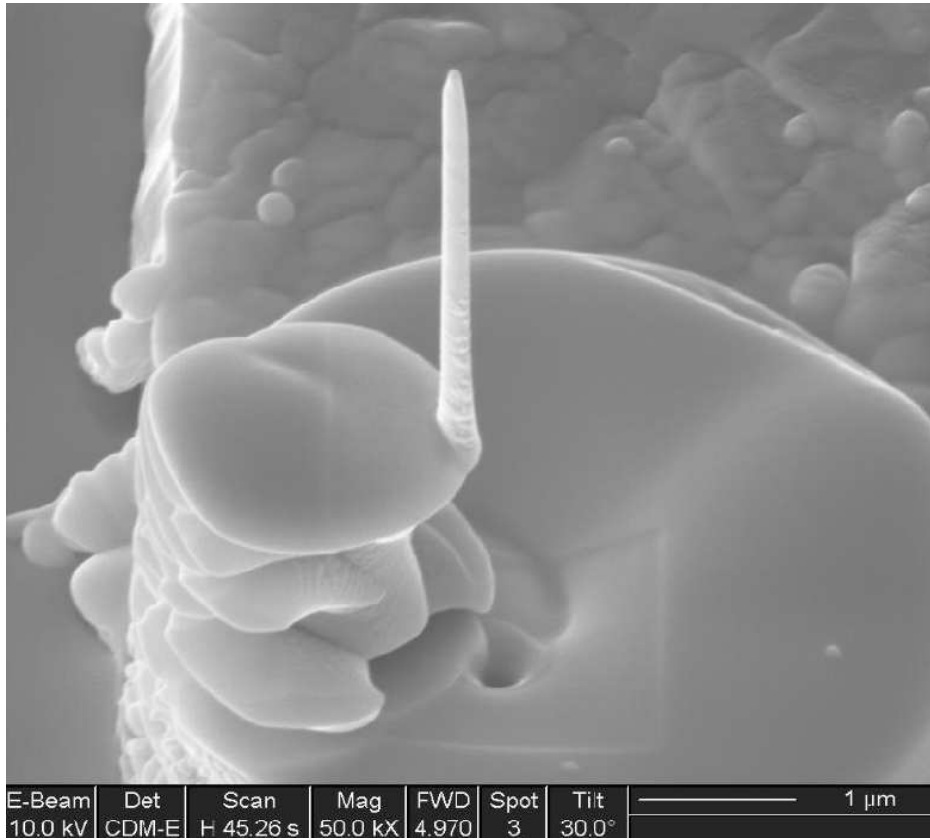


Figure 4.4: Self-grown tip by ion beam assisted deposition.

Figure 4.6 shows a line scan from a Transmission Electron Microscopy (TEM) image of a 4.3 nm wide hole after platinum deposition.

The advantage of this method is that the hole closing can be monitored online with the help of the Scanning Electron Microscope (SEM) incorporated in the FIB. This enables the reproducible production of small holes.

Figure 4.7 shows a cantilever into which three holes of different sizes were drilled. The central hole was drilled with the FIB directly and has a diameter of $3\text{ }\mu\text{m}$. The hole below and the one right next to the tip were closed down via platinum deposition to diameters of 300 nm and 100 nm, respectively.

More details about this method can be found in the paper by Schenkel *et al.* [Schenkel *et al.*, 2003].

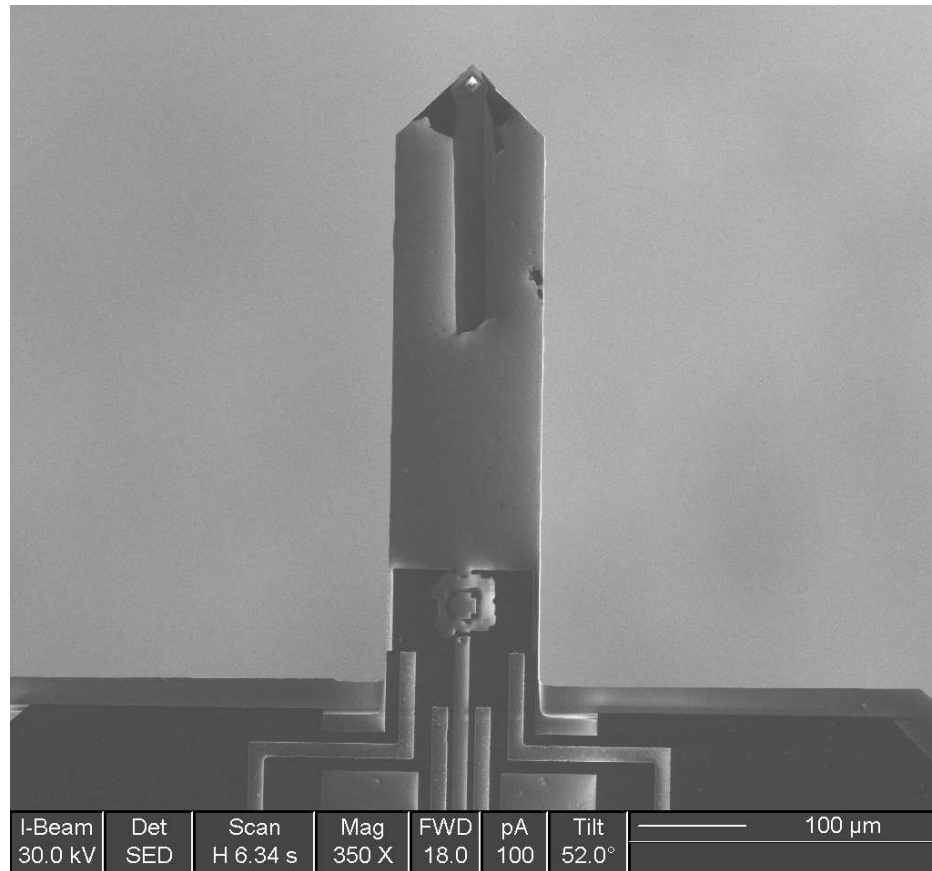


Figure 4.5: Piezo-resistive cantilever with a glued on commercial tip.

4.4 Operation

The SPM is operated in contact mode, although non-contact mode would also be possible since the cantilevers can be equipped with actuators as shown in the paper by Ivanov *et al.* [Ivanov *et al.*, 2003]. For actuated cantilevers, instead of using a piezo-driven stage to move the whole holder on which the cantilever is mounted, only the beam itself is forced to oscillate. This has the advantage of having to move less mass during the oscillation, which makes oscillating the beam at higher frequencies easier. To achieve this the beam is equipped with a bimorph material combination and via an alternating heating current supplied through an actuator on the beam, it is forced to oscillate at the frequency of the heating power.

The SPM can be used at air or in vacuum. Data shown in this thesis have been taken in vacuum at a pressure below 10^{-5} Pa (10^{-7} Torr).

The cantilever is positioned by a flexure stage which has a range of

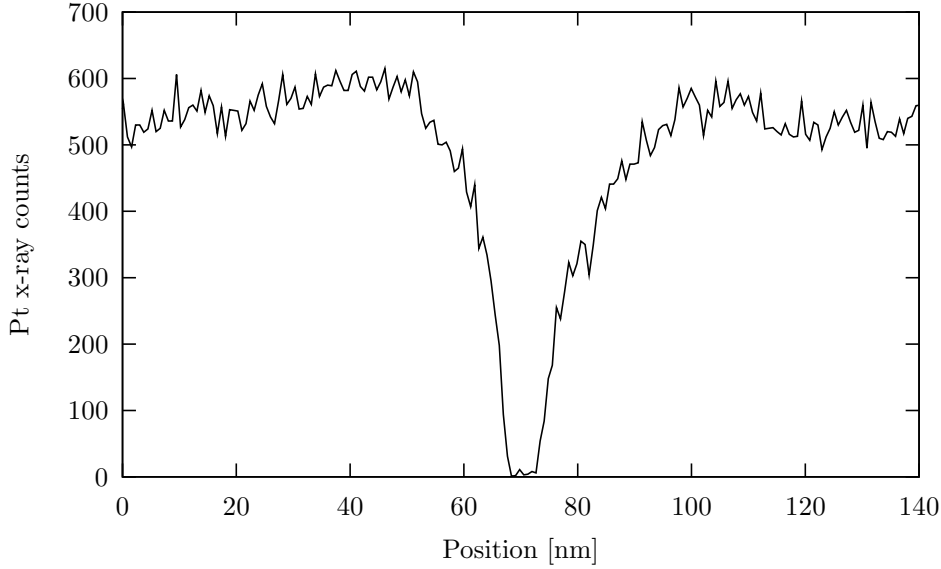


Figure 4.6: TEM image of a FIB-drilled hole in a silicon nitride membrane.

2 mm above the sample at the region of interest, using micromanipulators. Full control of all three dimensions is possible with the flexure stage setup implemented. Coarse approach is achieved by hand using one axis of the micromanipulator-controlled flexure stage and can be monitored by an optical microscope. Contact is made by bringing the tip within a few micrometers of the sample and then raising the sample stage. This way a controlled approach can be achieved and crashing of the tip into the surface can be avoided.

The set-point, scan area size and the feedback loop are controlled by the RHK SPM-1000 electronics.

4.5 Characteristics

In the following some of the characteristics of the SPM that influence the accuracy of the apparatus are discussed. Calibrated test samples were used to probe the resolution limits of the setup.

4.5.1 Noise considerations

Any measurement will be accompanied by noise, in particular the measurement of small signals can be difficult because of too much background noise. In our case we have to differentiate between two different types of noise:

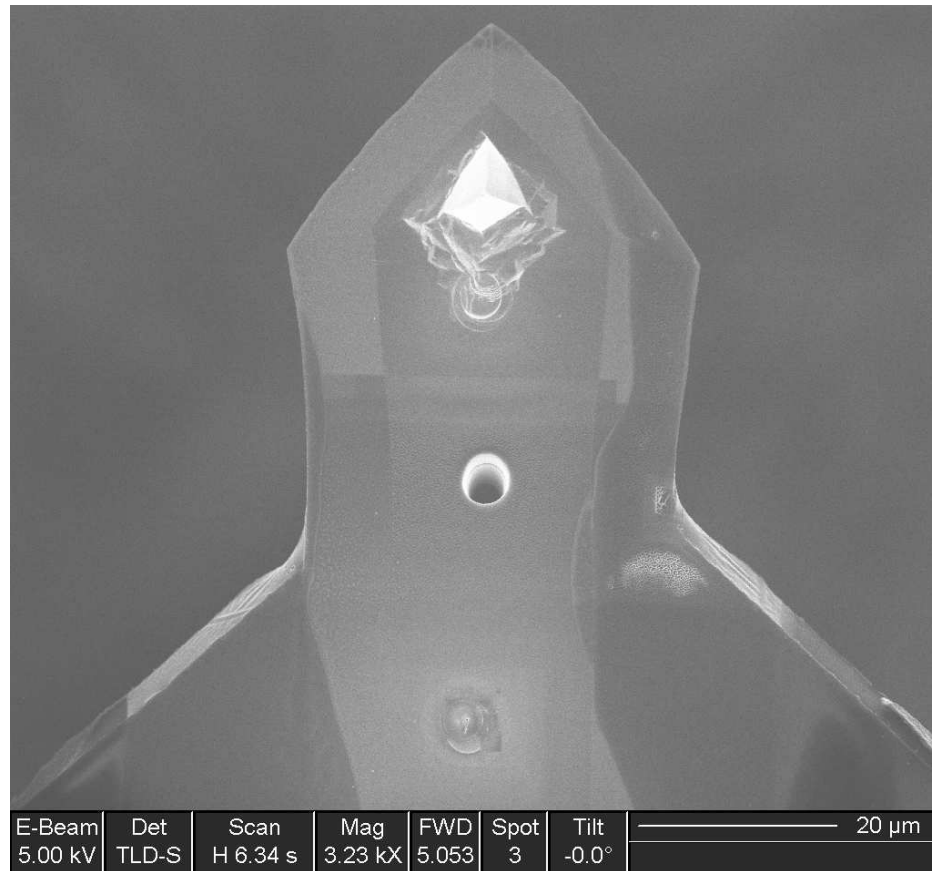


Figure 4.7: Cantilever with three FIB-drilled holes, two of them closed down by local platinum deposition. The sizes of the holes are 100 nm, 3 μm and 300 nm (top to bottom).

- Electrical noise

The signal we want to measure is an electric signal and therefore electrical components are used to measure it. These include amplifiers, filters, cables, etc. All of these add noise to the signal. The most common noise source here is pickup from other electric signals through cable connections, for example the 60 Hz noise from power supplies and power lines. Other sources include radio signals, mobile phones, etc. Often the electrical signal is also influenced by temperature, for example the amplifier output can vary with temperature. Cables can also add electrical noise through piezoelectric effects and triboelectric effects. Furthermore, leakage currents can occur and ground loops can act as big antennas for all kinds of signals.

- Vibrational noise

We want to detect the deflection of the cantilever due to surface topology, but there are other noise sources that can also lead to a bending of the cantilever which then produce a noisy signal. In air in particular the beam of the cantilever acts like a microphone: Any sound wave that reaches the cantilever will lead to a signal. This is not a problem for us since our experiments are carried out in vacuum, but other vibrational sources also exist in vacuum. In our case there are several turbo-molecular pumps connected to the beamline which rotate at different frequencies and can cause a resonant vibration in either the cantilever or the stage. In both cases the cantilever will pick up a signal. The beamline will also pick up other vibrations from the room and transfer them to the AFM.

Some of these noise sources can be reduced or excluded easily, others are harder to eliminate. Many electrical problems can be reduced or completely removed by a good setup. Ground loops, for example, can be prohibited by only having one common ground to all measurement equipment. Tying down the cables helps to reduce noise from piezo- and triboelectric effects. Also, amplifying the signal as early as possible helps to increase the signal-to-noise ratio. In our case this means implementing a first pre-amplification stage as close to the Wheatstone bridge as possible. Many other sources of electrical noise, however, cannot be eliminated as easily. For example, to operate the beamline many power supplies are needed which generate 60 Hz noise.

Vibrational sources are harder to eliminate, since the setup cannot be changed so that all turbo-molecular pumps could be switched off during operation. In addition, isolating the stage and the cantilever was not feasible. For possible improvements see Section 7.2.1.

Nevertheless operating the SPM was possible, since the desired resolution of 5-10 nm is over an order of magnitude higher than the atomic resolution (0.2 nm) that can be achieved with SPMs today, thus not too much noise reduction is needed.

A typical *noisy* spectrum taken in vacuum with the tip in contact with a silicon sample is shown in Figure 4.8. Some electrical noise at 60 Hz and the harmonics at multiples of 60 Hz can be seen. Several higher frequency peaks are also visible. The stage itself has a resonant frequency of around 400 Hz. The high frequency peaks can be safely filtered out with a low-pass filter without sacrificing resolution. The peak at 1 kHz was identified as a vibrational mode excited by a nearby turbo-molecular pump. This conclusion was reached by turning the pump off and following the noise spectrum over time. The result of this experiment can be seen in Figure 4.9, where different

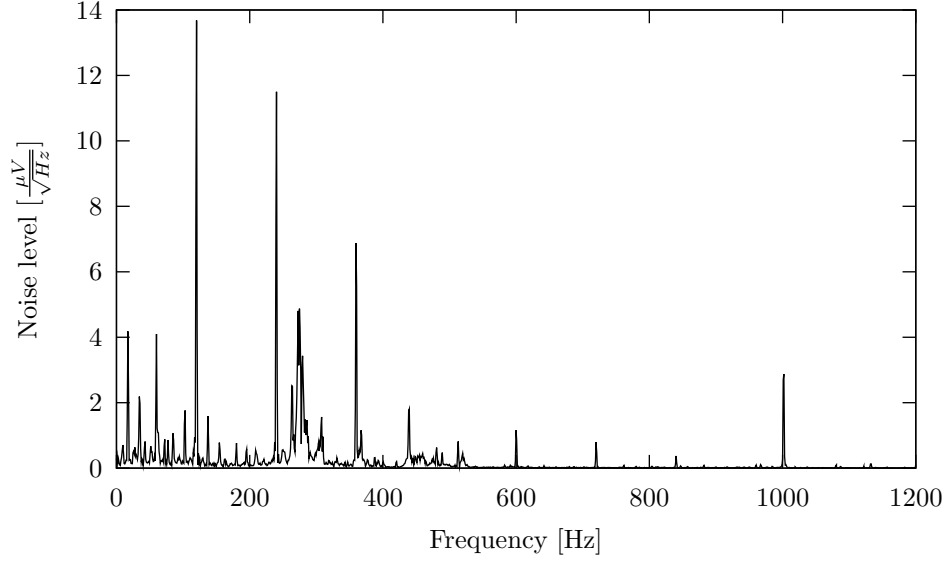


Figure 4.8: A typical noise spectrum taken under high vacuum conditions in contact mode.

noise spectra are shown at different times. The turbo-molecular pump can be seen to spin down, that is, the peak at 1 kHz at $t = 0$ drifts towards zero and then disappears. One can also see several other resonances being excited while the pump is spinning down. By turning off this particular turbo-molecular pump during operation the noise level decreased considerably as can be seen from the data presented in the following paragraphs.

4.5.2 Vertical resolution

A good way to determine the vertical resolution of an AFM is to look at force-distance (F - Z) curves during the approach of the tip to the surface. An F - Z curve is measured by changing the distance between the cantilever and the sample and recording the output signal of the Wheatstone bridge which is proportional to the force between the tip and the surface. The curve consists of three different segments: First the tip is located above the surface and a constant input signal should be detected (no force), then there is the *jump to contact* region, where the tip feels the attractive potential of the surface (for example van der Waals forces) and finally a contact region where the output signal is almost linear to the distance. The noise level can also be clearly seen in an F - Z curve. Furthermore, as the data for F - Z curves is taken with the feedback loop off, no filtering by the feedback loop takes place. In normal operating mode the feedback loop also acts as a filter, since

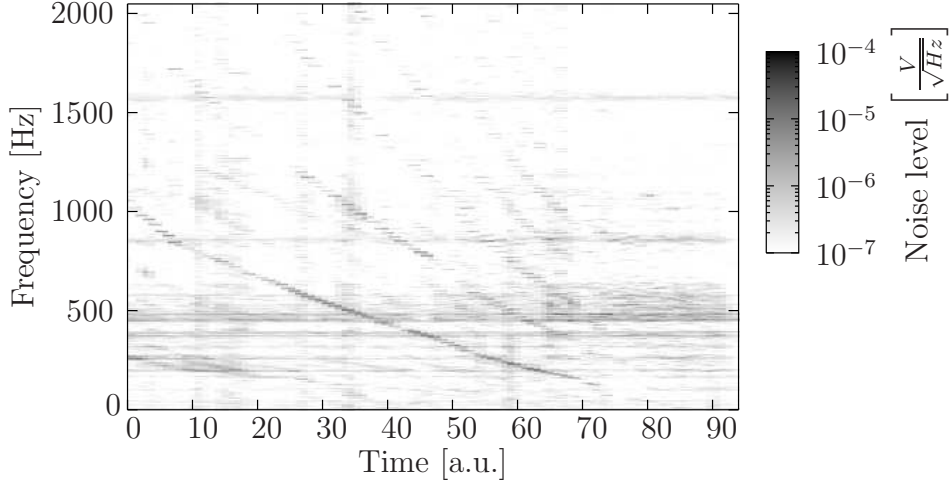


Figure 4.9: Effect of the turbo pump spinning down on the noise spectrum. The noise level is given in $\text{V}/\sqrt{\text{Hz}}$.

it integrates the signal over a certain time constant (a low-pass filter).

In Figure 4.10 an F - Z curve without applying any filtering in the second pre-amplifier stage is shown. The data was taken in vacuum without turning off any pumps or other equipment which would have reduced the vibrational noise. From the right hand side of the figure the force sensitivity of the sensor can be obtained and in this case $2.5 \pm 0.02 \mu\text{V}/\text{nm}$ was measured. The rms-noise levels before and after contact are $26 \mu\text{V}$ and $27 \mu\text{V}$, respectively. This translates into an uncertainty of 11 nm. Figure 4.11 shows the same experiment with a low-pass filter in place at the second pre-amplifier stage and with the turbo-molecular pump closest to the SPM-setup having been turned off. Carrying out the same analysis as above, a more accurate resolution for the force sensitivity of $2.65 \pm 0.005 \mu\text{V}/\text{nm}$ is calculated. The rms-noise level for non-contact and contact mode are 1.1 nm and 2 nm, respectively.

To test the vertical resolution further, a calibrated test sample with lines of 20 nm in height and $3 \mu\text{m}$ pitch were used¹. A line scan over a $8 \mu\text{m}$ wide area can be seen in Figure 4.12 and an image of the whole area is shown in Figure 4.13. These measurements confirmed the vertical resolution measured by the F - Z curve.

¹The samples were made available courtesy of Alvaro San Paulo from the University of California, Berkeley (UCB)

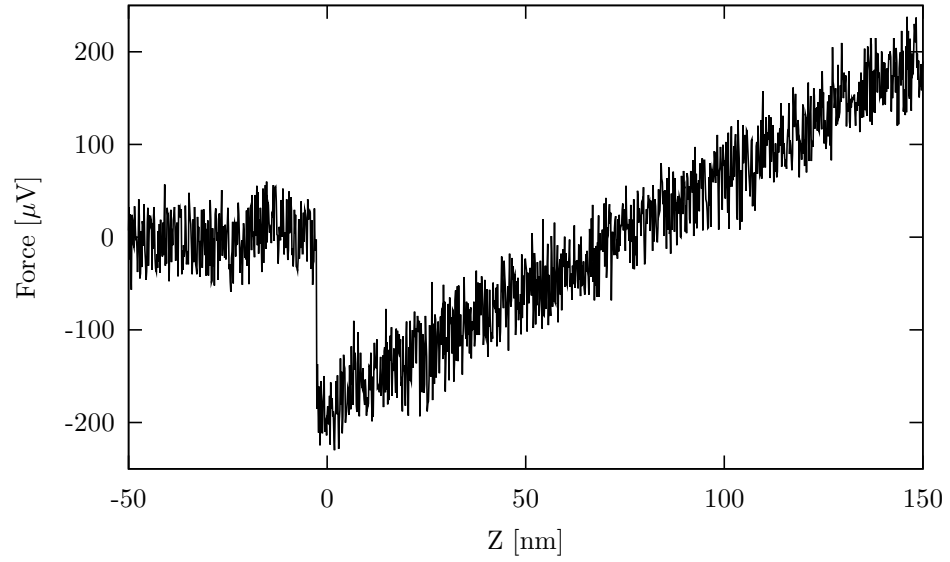


Figure 4.10: Force-distance curve with turbo pump on.

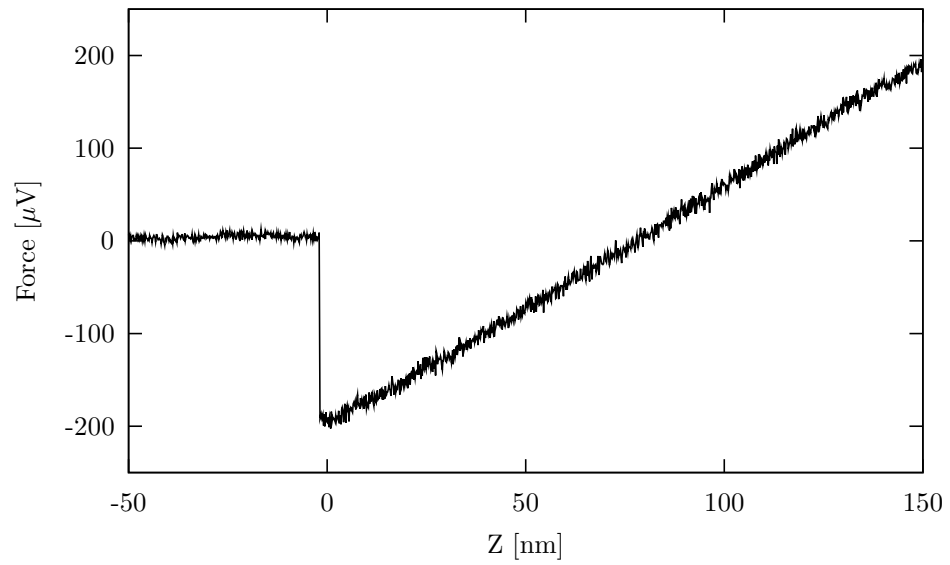


Figure 4.11: Force-distance curve with turbo pump off and filtering of the signal.

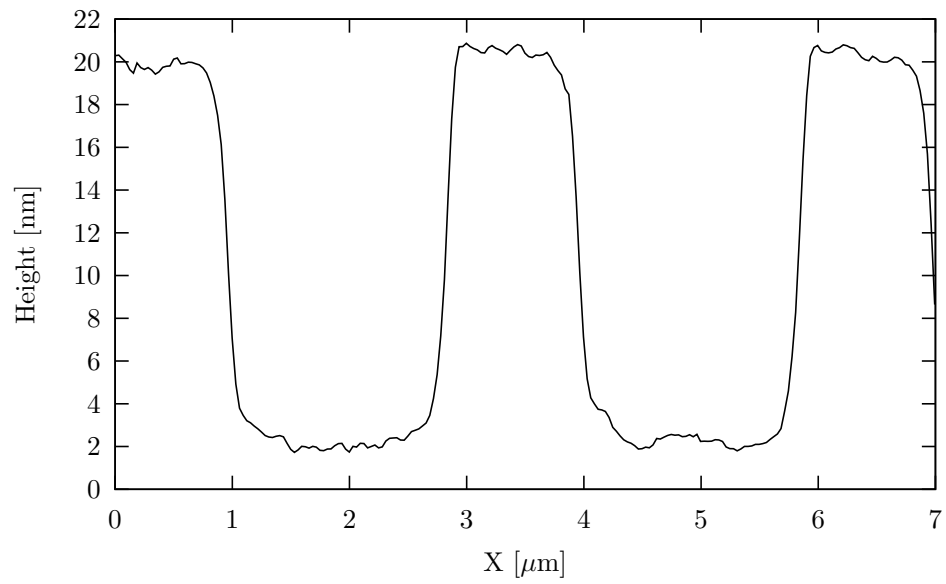


Figure 4.12: Line scan of a calibration sample with 20 nm steps.

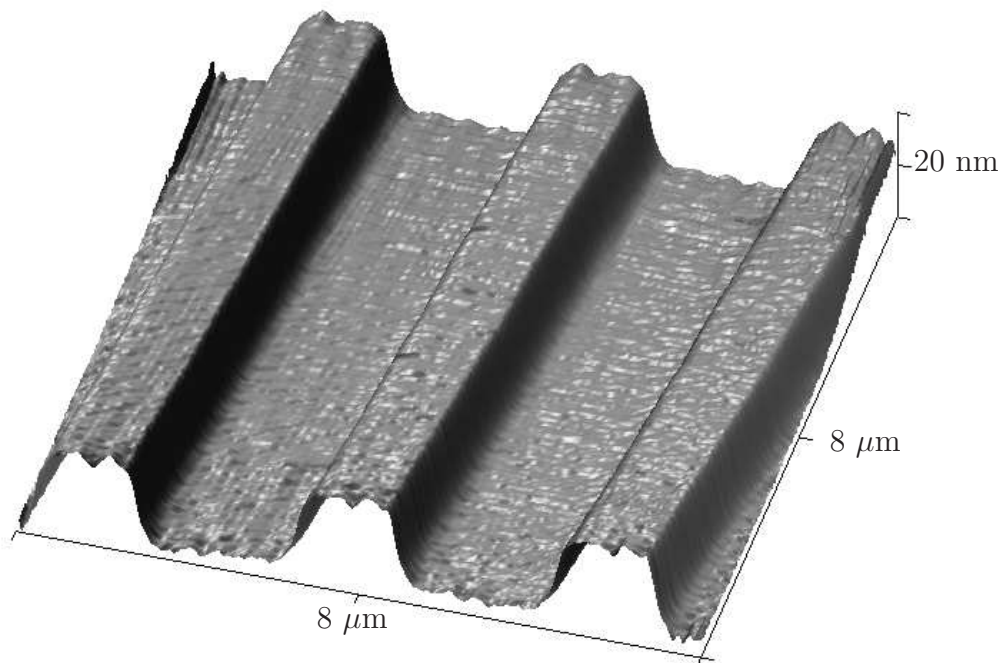


Figure 4.13: 3D-image of a calibration sample.

4.5.3 Lateral resolution

The lateral resolution is harder to test. A common method is to use test samples with gold particles on them, but such test samples were not available. Therefore, the samples at hand were also measured with a gauged commercial AFM for comparison. In Figure 4.14 a cross-section scan of a silicon marker

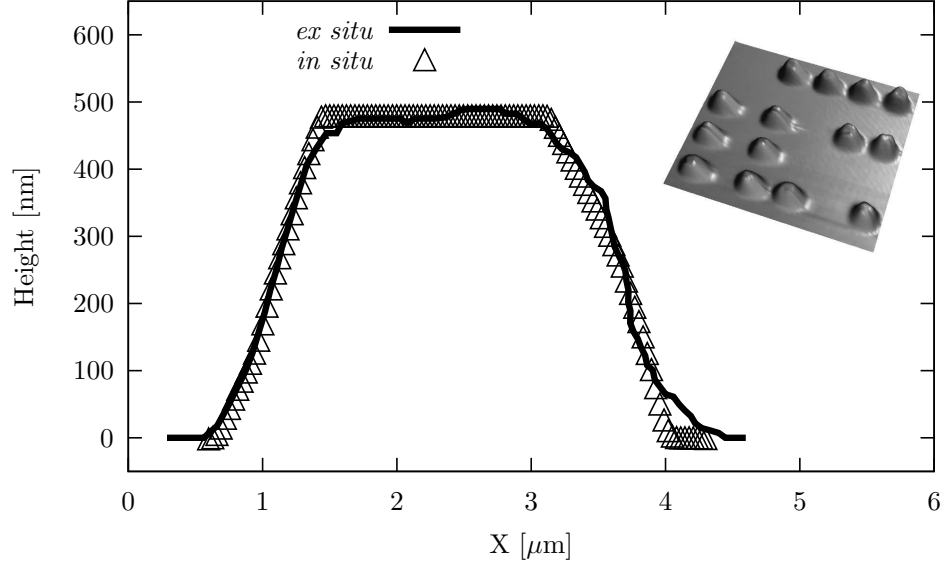


Figure 4.14: Comparison of the lateral resolution of our AFM (*in situ*) with a commercial AFM (*ex situ*). The inset shows a 3D-scan of the sample taken with our AFM.

can be seen. The same marker was imaged at almost the same location with a commercial AFM, a Park Scientific Instruments M5. Both plots are shown in the image. By comparing these two at full width half maximum (FWHM), an agreement in the range of 10 nm is inferred. This shows that our lateral resolution is of about the same order as that of a commercial AFM. Quoting absolute values with this method is, however, not possible as the uncertainty in the location of both scans could vary by several nanometers. As a further test of resolution a sample with 50 nm wide trenches was imaged. The sample was prepared by an imprint technique and a scan of it can be seen in Figure 4.15. The trenches can be clearly identified which demonstrates the high vertical resolution of our AFM.

4.5.4 Drift

To check for possible drift in the setup, the same test sample as for the vertical resolution investigation was used. The tip was set to a position

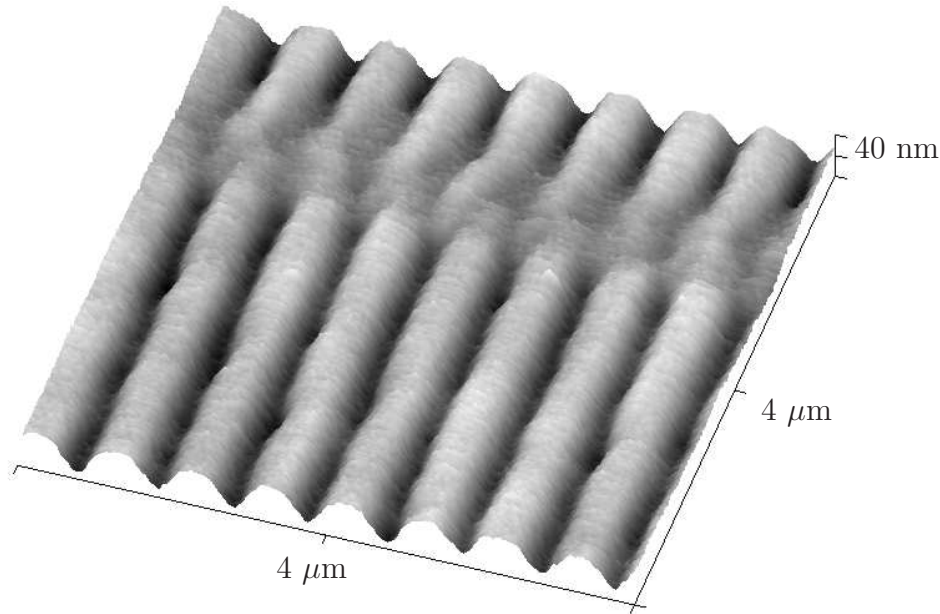


Figure 4.15: 50 nm wide trenches imaged with the our AFM.

where it scanned over several lines of the test sample. With the slow scan direction disabled, the same line was scanned repeatedly. By watching the position of the edge over time information about the drift of the system can be gathered. To obtain long-term information the scan speed was set so that the image was taken over several hours (one line per 64 s). The result can be seen in Figure 4.16. To begin with the edges drifted to the right, which is due to the warming up of the piezo-stage after turning it on. Later, however, the drift decreased and a value of about 20 nm/h ($=3 \text{ Å/min}$) is calculated.

4.5.5 Tip lifetime

Another issue was the lifetime of a tip. Unfortunately, the self-grown platinum tips only lasted several scans and were then no longer useful. This meant that the affected cantilever had to be taken back to the FIB so that a new tip could be grown. The commercial tips had a longer lifetime, being able to be used for several tens of scans, making them our preferred choice. However, even these tips became blunt after a while. Figure 4.17 shows SEM images of a new and a blunt tip. Nevertheless, even the blunt commercial tips could be repaired by the FIB, either by rebuilding or sharpening them again (see also [Vasile *et al.*, 1991]). Figure 4.18 shows the result of sharpening a blunt tip.

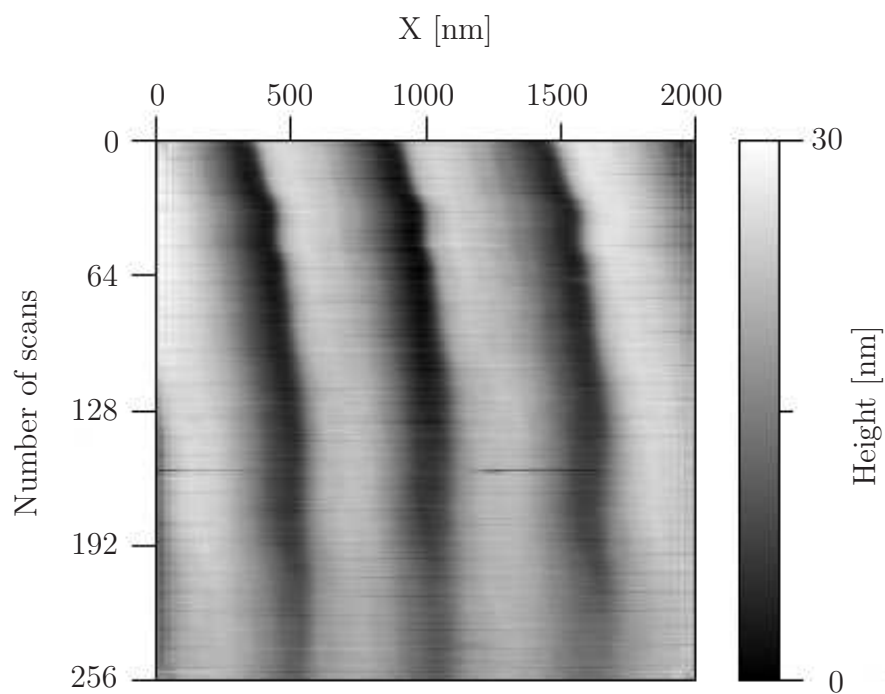


Figure 4.16: Repeated line scan to determine the drift in the setup.

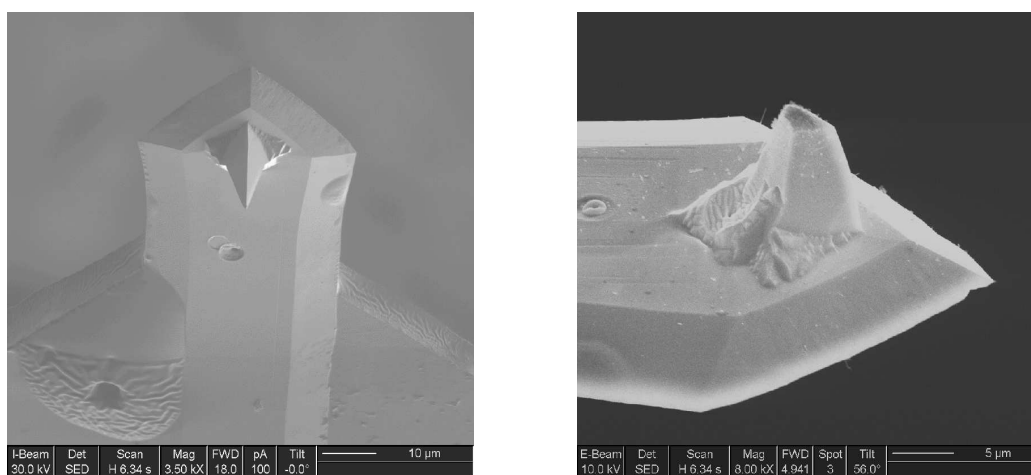


Figure 4.17: Commercial tips: A new tip (left) and a used tip (right).

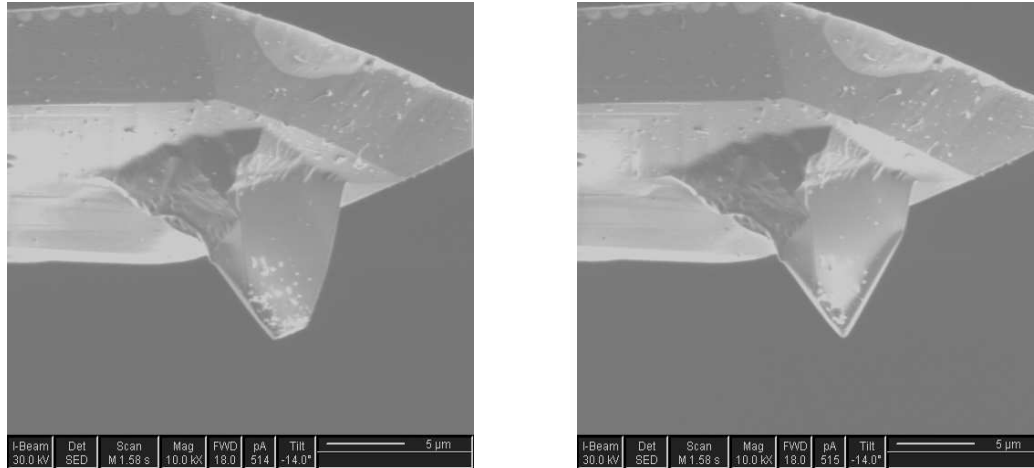


Figure 4.18: A commercial tip before (left) and after (right) refurbishment.

The reason for the relatively short lifetime is the fact that the force with which the cantilever was pressed onto the surface was too great. Compared with a commercial AFM our setup produced around two orders of magnitude higher forces. This problem can be traced back to an offset compensation problem of the Wheatstone bridge. The offset has to be compensated for with the help of an offset adjustment, in our setup this was included in the Stanford model SR560 amplifier. However, the offset correction was applied after the amplification step so that a given offset was amplified before compensation. This limited the range of the usable amplification. A better way would be to apply the offset before the first or the second amplification stage and to then amplify the compensated signal. This feature will be added in future experiments. For the self-grown tips the fact that platinum is a soft material also shortened the lifetime of those tips.

4.6 Summary

For our purposes the SPM works very well, even without vibration isolation. It shows a resolution good enough to be able to align the tip with respect to markers with an accuracy of about 10 nm. The ultimate design goal for this machine is a slightly better alignment accuracy, but the vibration isolation in particular leaves lots of room for improvement. Thus it should not be a big problem to increase the lateral resolution if needed. The vertical resolution is already suitable for the design goal.

Electrical noise pickup is present, but does not limit the resolution. Vibrational modes play a bigger role, especially since no special arrangements have

been made to suppress them. Simple measures can be taken to decrease the vibrational noise level as for example turning off the closest turbo-molecular pump during an experiment or in the long run exchanging these pumps with ion pumps. Nevertheless, the vibrational modes also do not limit the functionality at present.

Chapter 5

Experimental Setup

For the experiments the AFM was integrated into the EBIT beamline. The final setup is described and sample preparation is discussed.

5.1 Final Beamline Section

The SPM is now mounted at the end of the beamline. That is, behind the bending magnet so that only one well-defined charge state is used for experiments. A schematic of the setup from the bending magnet onwards is shown in Figure 5.1. After the magnet the beam passes a small drift section through an iris and a cube where a position sensitive multi-channel plate (MCP)-detector can be inserted. It then passes an Einzel lens and a quadrupole lens, which focus the beam into a 6 in cube that can be used for other experiments, for example ion beam exposures. At the beam entrance to the 6 in cube a beam-limiting aperture of 3 mm in diameter was added for reasons discussed later (see paragraph 6.1.3). The 8 in cube is mounted right after a short drift section incorporating a retractable Faraday cup, behind the 6 in cube. Two sets of turbo-molecular pumps are used for pumping and two valves before and after the bending magnet can be used to close off this section of the beamline so that the vacuum cycle for a change of samples is fast. A telescope is mounted at one end of the magnet, with a line of sight down the beamline, and can therefore be used to check the alignment of the target or beam elements such as slits and movable detectors.

Inside the target cube a set of four deflector plates and a lens assembly is mounted. The last beamline element is a grounded aperture of 1 mm in diameter followed by the SPM setup as shown in Figure 4.2. One port of the cube is used for the micro-manipulators to control the coarse motion of the tip. The opposite port is used for an optical microscope that is used to

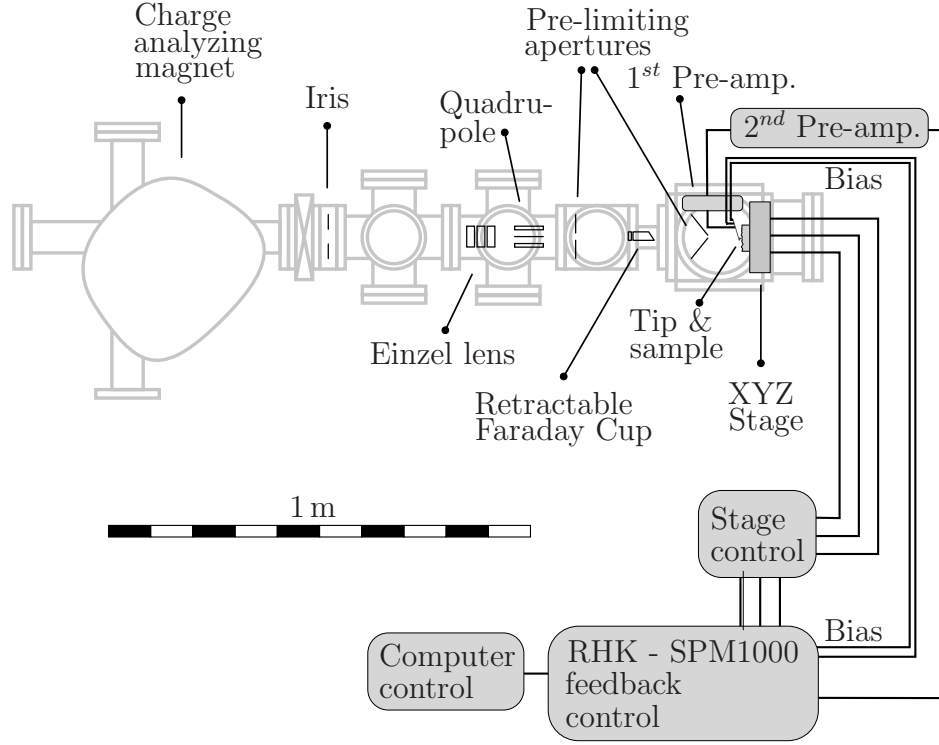


Figure 5.1: Experimental setup.

monitor the tip approach. The bottom flange is used for electrical connection of the deflector plates and lenses and the top one is available for a detector setup. The stage itself is mounted vertically on the last available flange.

5.2 Sample Holder and Sample

Silicon chips coated with a thin resist film were used as samples. The sample is mounted directly onto a nano-stage from Physical Instruments (PI). For ease of sample changing, the sample holder can be removed from the stage without dismounting the stage itself. A convenient sample size is about one square centimeter. The samples were glued onto the target holder with double sided copper tape to prevent them from charging up. However, the target holder is also electrically isolated from the stage, so that the beam current on the target can be measured. To achieve this the holder is connected to a feed-through, which is either grounded or connected to a Keithley 617-electrometer.

5.2.1 Resist

To test the ion implantation two different resists were tested.

Polymethylmethacrylate

Most results were obtained using polymethylmethacrylate (PMMA). PMMA is a very common resist for micro-lithographic processes using electron beams, x-rays or deep ultraviolet radiation. It can also be used for ion beam exposure [Ryssel *et al.*, 1981, Karapiperis *et al.*, 1985]. The resist is normally spun onto a wafer and the thickness of the resist depends on the spin speed, the molecular weight of the resist and the solvent. Common conditions are 495 k or 950 k molecular weight, spin speeds of 1000–3000 rpm and as solvents chlorobenzene or anisole are used with 2–10 % of PMMA. Typical resist thicknesses for these conditions range from 50–1000 nm [MicroChem Corp., 2001].

PMMA is a positive resist, meaning that when it is exposed and developed the area irradiated by the beam is removed. A typical dose requirement for developing with ion beams is of the order of $1 \mu\text{C}/\text{cm}^2$ [Karapiperis *et al.*, 1985].

Hydrogen silsesquioxane

As an alternative resist hydrogen silsesquioxane ($[\text{HSiO}_{(3/2)}]_8$) was used. Its chemical structure is shown in Figure 5.2. This inorganic resist gives a higher

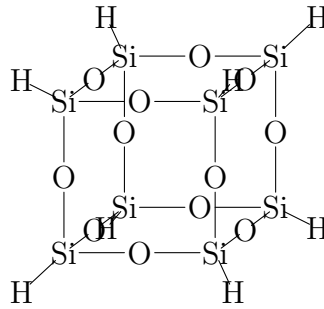


Figure 5.2: The structure of HSQ.

resolution than PMMA, that is, it shows fewer line width fluctuations [Namatsu *et al.*, 1998] and small feature sizes [Word *et al.*, 2003]. Due to these properties hydrogen silsesquioxane (HSQ) is often used for Electron Beam Lithography (EBL).

During exposure of the resist scission of the Si–H bonds occurs followed by cross-linking of two broken bonds with oxygen, producing strong Si–O–Si bonds. Standard HSQ is easily soluble in alkaline hydroxide developers, but

due to the cross-linking the exposed area has a highly reduced solubility so it remains after developing. HSQ is therefore a negative resist.

To produce a thin film, HSQ is diluted with for example methylisobutylketone (MIBK) and spun onto a wafer. Afterwards the wafer is normally baked at a few hundred degrees Celsius for several minutes to remove excess solvent.

As a developer tetramethylammonium hydroxide (TMAH) (for example Shipley LDD26W) is commonly used followed by rinsing in de-ionized water and drying with N_2 gas.

5.3 Additional Ion Source

In addition to the EBIT another ion source was used, a **Physical Electronics Industries, model 04-303** ion gun. This produces a medium current, low charge state, low energy beam and was used here to produce an Ar^{2+} beam, delivering several nA of beam current onto the final target area. Ions are produced in this source via ionization by electrons produced by thermionic emission from a heated filament. The acceleration voltage for the extracted beam can be varied up to 4 kV.

The ion gun is mounted next to the electrostatic bender (see Figure 3.3) and can be used instead of the EBIT if the bender is turned off. The ion beam passes through a mesh in the outer electrode of the bender and then enters the beamline.

The advantage of this ion source is that no cool down is needed and the beam can be turned on within a few minutes. It also produces a higher beam current than the EBIT, which can be advantageous for testing purposes. The disadvantage is that the beam quality is very poor and only low charge state ions can be created. The ion source is thus mostly used for testing new setups before an EBIT run. However, in the case of the SPM setup the ion source was used in most of the experiments reported in this thesis.

5.4 The Experiments

To show the implantation through the hole in an AFM cantilever, patterns were formed in the resist layer of the target. During exposure the tip was either brought into contact or positioned a few micrometer above the surface and then moved to different locations while the ion beam was on. The control software of the SPM allowed the set of coordinates to which the tip should be moved to be defined. A dwell time for each spot and the speed at which the sample should be moved between spots could also be defined. This way, with

a long dwell time and a fast moving speed individual spots can be formed lithographically. In contrast, by using a small dwell time and a slow moving speed lines are formed in the resist.

Chapter 6

Lithographic Results

Patterns formed using the aperture in the cantilever as a mask are now presented and a comparison is made with results from various methods in the literature (see also Chapter 7).

6.1 Lithographic Patterns in Different Resists

Using the low charge state ion source and the two resists described in Section 5.2.1 the same pattern was formed in the both resists.

An argon beam was extracted at 3 kV from the ion source. Ar^{2+} ions were then selected with the bending magnet and the beam was used to create patterns in the resist films. The beam current measured on the target was of the order of 1 nA and a cantilever with a 300 nm wide FIB-drilled hole was used as a mask. The stage was programmed to move to certain pre-defined points and a dwell time of 10 s was selected per spot. The travel time between two spots was set to less than 10 ms and could therefore be neglected. The sample was then taken out of the vacuum chamber, developed, rinsed in isopropanol or water and blown dry with nitrogen.

6.1.1 PMMA

For the experiment PMMA in anisole with a molecular weight of 495 k was first used. The resist was spun onto a 4 in silicon wafer and then pre-baked at 60°C for 1 min, resulting in a 50 nm thick resist film. The wafer was then broken into smaller pieces with dimensions of about 5 mm×10 mm so that they could be mounted on the sample holder. The exposure time was set to 10 s/dot, but the sample was exposed several times (see section 6.1.3), so that the total dose might have been higher. The PMMA was developed using a

1 : 3 composition of MIBK and isopropanol. The developing time was 30 s. An image of the pattern can be seen in Figure 6.1.

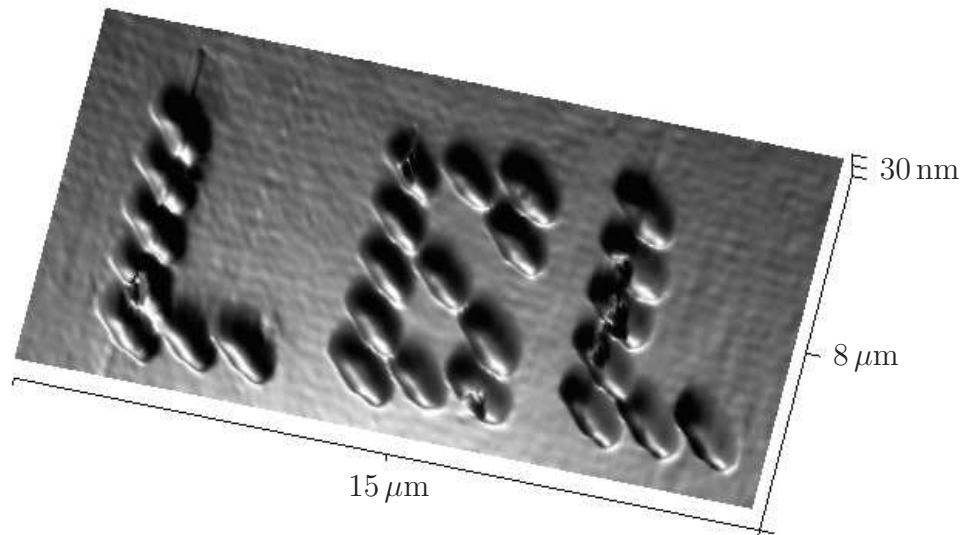


Figure 6.1: *Ex situ* AFM image of a developed lithographically defined pattern using an argon beam in PMMA.

6.1.2 HSQ

The same pattern as in the case described above was also exposed in HSQ resist. As with the PMMA sample each dot was exposed several times, using the same exposure time per dot as for the PMMA. Afterwards the sample was developed for 2 min in LDD26W, which is a standard developer for HSQ. The results can be seen in Figure 6.2.

6.1.3 Beam shape

In both of the exposures the dots formed with the argon beam were oval-shaped. This was due to the large emittance of the argon beam, which made focusing the beam onto the target area difficult. Focusing was made harder still by the fact that the Faraday cup used for tuning was located further up the beamline, so maximizing the current in the cup did not necessarily mean optimizing the beam for the target area. Due to this and the fact that the acceptance for the beam-limiting hole in the cantilever is rather small, sometimes no beam was transported through the hole although a current could

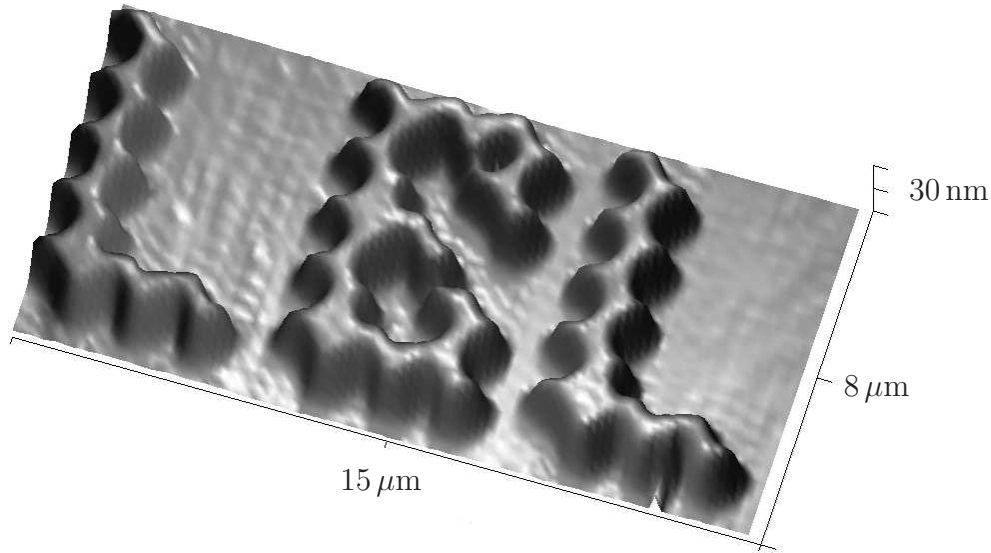


Figure 6.2: *Ex situ* AFM image of a developed lithographically defined pattern using an argon beam in HSQ.

be measured on target. In order to increase the chance of drawing a pattern, each dot was exposed several times under slightly different beam conditions (different settings for the last Einzel lens and the bending magnet). It should be noted, however, that the oval dot shapes were not the result of multiple exposures as they also appeared in single shot exposures. The tuning problem was addressed later by adding another beam-limiting aperture of 3 mm diameter in the 6 in cube, about 40 cm before the target area, allowing better beam alignment. Now even the oval dot shapes disappeared and patterns produced with this improved setup can be seen in the next section.

6.1.4 Higher resolution, smaller features

Finally, the smallest line width achieved with the setup in the time frame of this thesis is presented. For this exposure the same kind of PMMA was used. The film was a bit thinner due to higher spin speed of 4000 rpm during the coating process. The wafer was then pre-baked at 160°C for 15 min, resulting in a 35 nm thick resist film. In Figure 6.3 different patterns can be seen. These patterns were generated with the cantilever shown in Figure 4.7.

In the picture the shape of the end of the cantilever, which was inserted from the right side of the picture, can be clearly seen as a shadow mask on

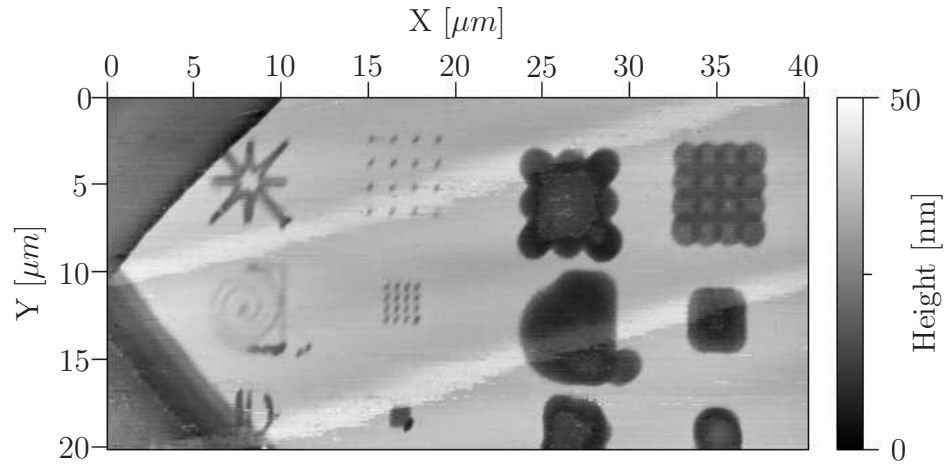


Figure 6.3: Different lithographic images in PMMA resist.

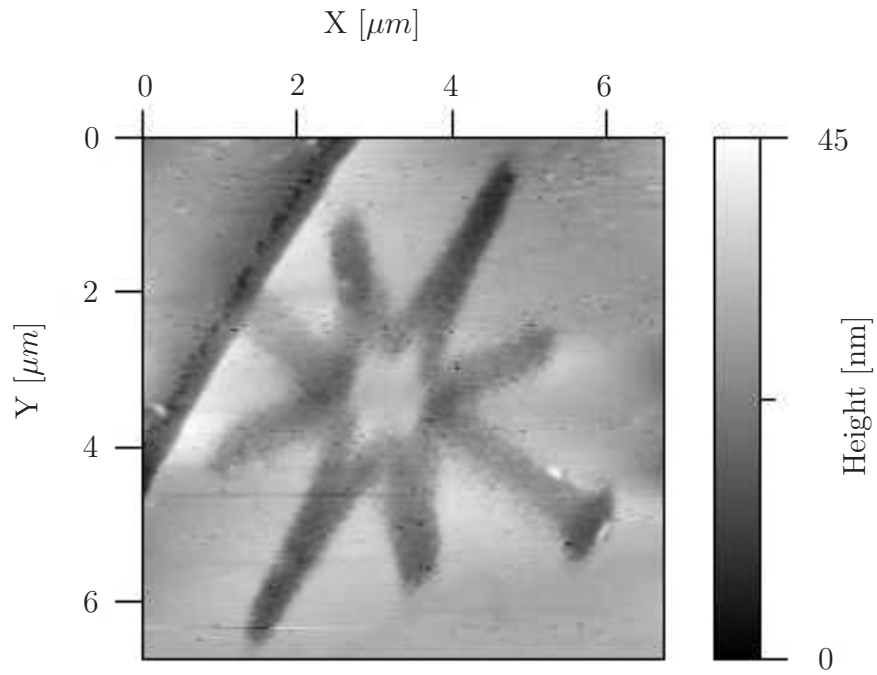


Figure 6.4: Zoom of Figure 6.3 showing a pattern defined by moving the ion beam across the target at a speed of 50 nm/s .

the resist (on the left). The six patterns on the left hand side were formed by the smallest hole in the cantilever which had a diameter of 100 nm. The six patterns on the right hand side were formed with the $3\mu\text{m}$ hole and were exposed at the same time. Due to the large size of this hole the single dots overlap and therefore the dot pattern cannot be easily identified. The patterns exposed through the third hole in the cantilever are not visible in this picture.

In addition to dots, lines were also generated. This was accomplished by using a short dwell time per dot (e.g. ms) and a slow moving speed between dots. Here, 50 nm/s was used to produce continuous lines, see Figure 6.4. For the lines generated with the smallest hole, a line width of down to 120 nm was measured. The line width varies, however, which can be a result of a combination of effects. The most probable causes are the variation in the beam current and emittance, due to the low quality of the ion beam.

6.2 Highly Charged Ions

Creating patterns as shown in the previous section is very hard with HCIs. The reason for this is the low beam current generated by the EBIT source, which is about a factor of thousand smaller than that of the low charge state ion source. For implanting single ions, which is the ultimate goal for the implanter, this is not a problem, especially since at that point a detector for single ion hits needs to be implemented into the setup and a slow implantation rate will be acceptable. However, for generating very small test patterns the time was not available. Therefore in this section larger features of the order of microns will be presented.

Figure 6.5 shows an area of PMMA exposed by xenon ions (Xe^{30+}) extracted at 6.6 kV through a $3\mu\text{m}$ hole in a cantilever. A beam current of 4 pA/mm^2 was used. The exposure time was 1 h. This time was not enough to fully develop the exposed region of PMMA and the black dots in the figure correspond to hits from single ions. The fact that single HCIs create defects on impact was first investigated by Ruehlicke *et al.* [Ruehlicke *et al.*, 1995]. It was then Gillaspy *et al.* at the National Institute of Standards and Technology (NIST) who first used HCIs for lithographic purposes, exposing PMMA. They also found that single hits from HCIs formed large impact craters in PMMA [Gillaspy *et al.*, 1998]. In their experiment they used a fixed stencil mask to create patterns in the resist.

A cross section of a crater generated by a single ion hit is shown in Figure 6.6. The craters are several nanometers deep and have a FWHM of about 60-80 nm. The depth resolution is limited by the AFM tip. In

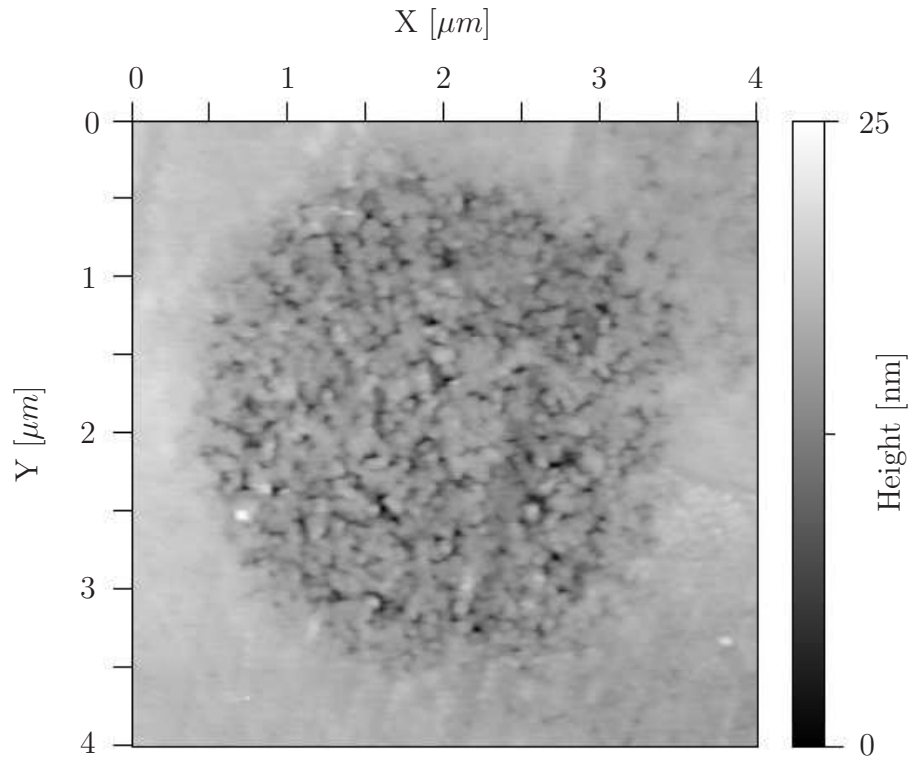


Figure 6.5: Single ion hits of Xe^{30+} implanted through a $3\mu\text{m}$ hole in the cantilever.

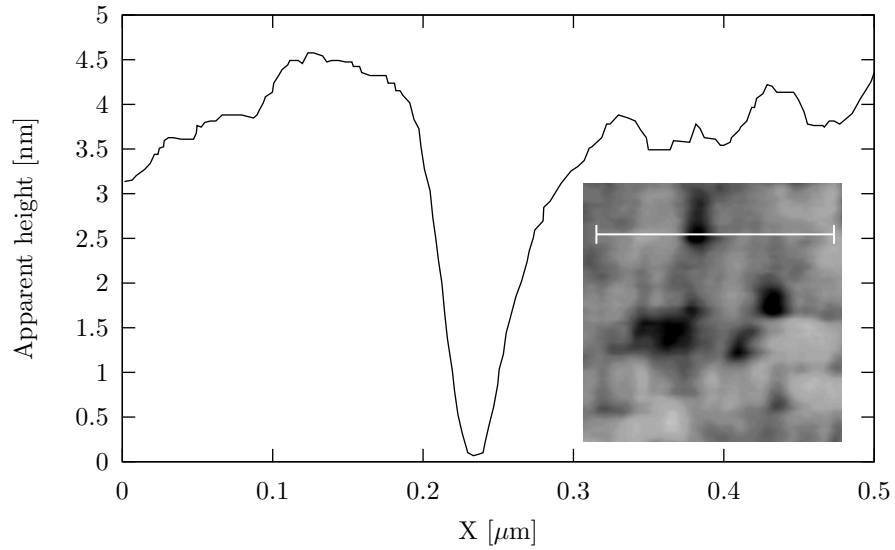


Figure 6.6: Cross section of a single ion hit of a HCl. The insert shows the AFM scan from which the cross section was taken.

contrast to the work by Gillaspy, the implantation here is not done using a fixed stencil mask, but with our SPM approach, so that different patterns can be generated.

Single ion hits from singly charged ions can also be registered. However, because of the smaller surface interaction the craters are much smaller and therefore those single hits are more difficult to image using a standard AFM. Nevertheless, Jamieson *et al.* managed to image craters from single hits of 35 keV gallium ions in PMMA after development [Millar *et al.*, 2005]. Due to the small feature size they needed to utilize a special AFM tip made out of carbon nanotubes, which resulted in better depth profiling of the surface. The craters found had an apparent depth of about 2 nm and a radius of about 10 nm.

The extra damage created by a HCI should not be a problem for the implantation of single ions, since most of the extra potential energy of the HCI is deposited in the first few atomic layers and a sacrificial layer (e.g. a thin SiO₂ layer) can be added to the wafer. For both low and high charge state ions, an annealing step is required to activate the donor atom in the silicon matrix and also to repair damage created during implantation.

Chapter 7

Outlook

This chapter gives a short outlook to the future of the project. First a single ion detection scheme is presented and the current state of the detection system is described. Then some ideas for improvement of the scanning probe setup are presented.

7.1 Integrating Single Ion Detection

The integration of a single ion detection scheme is crucial for the project goal of building qubit test devices. The idea behind using HCIs is to increase the amount of energy deposited in the material to make detection easier, since a HCI not only deposits kinetic energy but also a considerable amount of potential energy, which is the sum of the binding energies of the removed electrons. This extra energy results in more secondary particles being emitted in the surface region and also more energy being deposited inside the material, which creates more electron/hole pairs for detection. These two effects (secondary electrons and electron/hole pairs) present the two main options for detecting the implanted ion and will be discussed in the following.

7.1.1 Secondary electrons

A HCI causes the emission of one to two orders of magnitude more secondary electrons than a singly charged ion, to be more precise the secondary electron production s scales roughly with the charge q as: $s \sim 1.5q$. Each singly charged ion therefore produces of the order of one secondary electron in the low energy range needed for the shallow implants required for a QC, which would make a high detection efficiency using this scheme very hard and for very low ion energies impossible. A HCI on the other hand can produce

20 to 150 secondary electrons depending on the potential energy of the ion (and therefore the charge and species) and the target material. This makes detection of the hits with nearly 100% efficiency possible, even if not all secondary electrons are collected. The problem here lies in the integration with the setup of the scanning probe. To guide the secondary electrons out of the target area a magnetic field generated by permanent magnets has been added. A magnetic field was chosen for this purpose, as it is difficult to get the same effect with electrostatic elements without causing breakdown of the (high) voltage that would be needed to penetrate the area below the cantilever. Figure 7.1 shows a schematic of the setup. The electrons

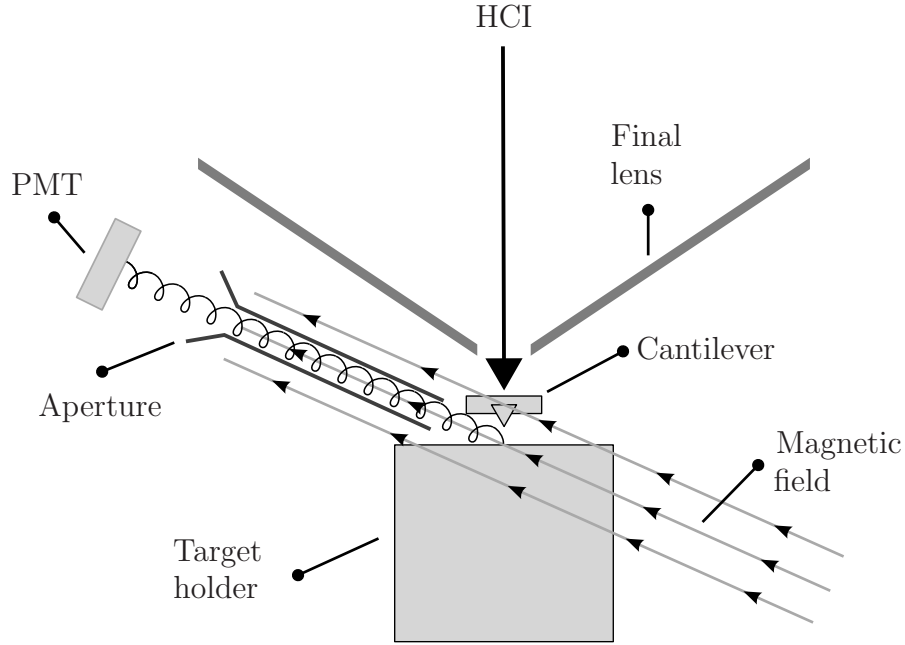


Figure 7.1: Setup for single ion detection with integrated detection.

follow the magnetic field lines and are then accelerated to a phosphorus screen biased at 0-15 kV, where each electron generates a number of photons (approx. 100 photons per 10 keV). These are guided through a Teflon-coated light guide made out of quartz to a photomultiplier tube (PMT) which is mounted outside the vacuum. Here, they create an electric pulse with a pulse height proportional to the number of secondary electrons on the phosphorus screen. In Figure 7.2 two different spectra can be seen. The first curve shows the detector background with the ion beam turned off and the second shows the effect of secondary electrons created by HClIs, here Xe^{37+} ions were used. The clear separation of the latter from the noise is due to multiple electrons

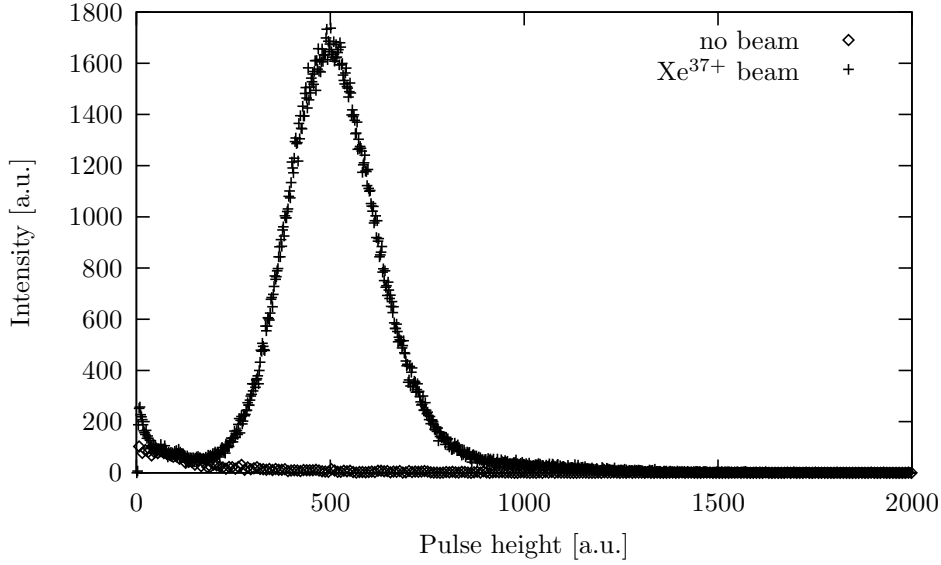


Figure 7.2: Spectrum due to secondary electrons on the PMT without the SPM in place, with the ion beam turned on and off.

hitting the detector at the same time. Therefore the detection efficiency of the highly charged ions is only limited by the overlap of the two curves and for the case shown in the figure an efficiency of $> 96\%$ was achieved. The dead-time of the detector is not an issue, since we are only interested in single hits which, given the beam current and the aperture size, will have a very small event frequency.

Including the cantilever resulted in problems that could not be easily solved, arising from the fact that the electrons are generated below the cantilever from where it is difficult to pull them out. The magnetic field applied to extract the electrons managed to guide some of them out, but not enough to clearly move the peak away from the single electron background that can be seen when the cantilever blocks the whole beam. In Figure 7.3 a spectrum from the PMT can be seen where a cantilever was mounted in the beamline. The graph shows three different measurements: A background noise spectrum with the beam off and two spectra with a bismuth beam, with the cantilever either retracted or in place. A peak from the HCI beam is evident when the cantilever is retracted from the beamline, but with the cantilever in place only events with a smaller pulse height can be seen. We attribute these reduced pulse heights to reduced electron collection from ions hitting the rear (beam-facing) side of the cantilever. To be able to distinguish these events from hits on the target, the pulse height generated on target would need to be increased, that is the collection efficiency would need to be higher. With

the present setup hits from single ions could not be separated from background noise with a high enough detection efficiency. Optimization of the

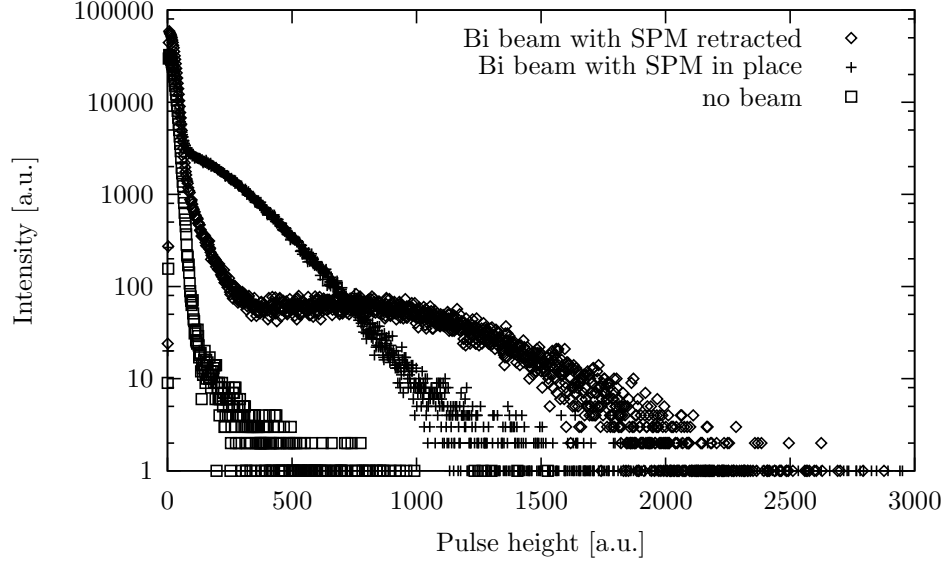


Figure 7.3: Spectrum from the PMT with the SPM setup. Multiple electron events are seen with the SPM retracted, but only single electron events show up with the SPM in place. A background noise spectrum with the beam off is also shown.

setup should be possible, whereby a better alignment of the magnetic field in particular should help. Unfortunately this requires a redesign of a major component of the setup, which was not possible in the given time. Improved shielding of the electrons generated on the rear side of the cantilever would also be helpful, but this requires a redesign of the cantilever itself to include, for example, a hollow pyramid as a tip which would work as an electron shield at the same time.

7.1.2 Transistors

Another option is to look at the electron/hole pairs generated inside the target material. The generation of electron/hole pairs is also enhanced by the use of HCIs, since a considerable part of the HCI potential energy is used to create them (see section 3.2.2). To be able to look at the electron/hole pairs a detector has to be incorporated into the target material. Here the fact that our main target material is silicon provides a relatively easy solution to the problem. A standard Metal Oxide Semiconductor Field Effect Transistor (MOSFET) can be built into the material. Implanting into the channel and

not having a gate deposited (through which one would otherwise have to implant) gives the option to use the source-drain device as an ion beam induced charge (IBIC) detector by biasing the source-drain at a few Volts. This potential difference would be enough to collect the electron/hole pairs and detect the impact of a single ion. A schematic of the idea is presented in Figure 7.4. A similar scheme has already been implemented by Jamieson

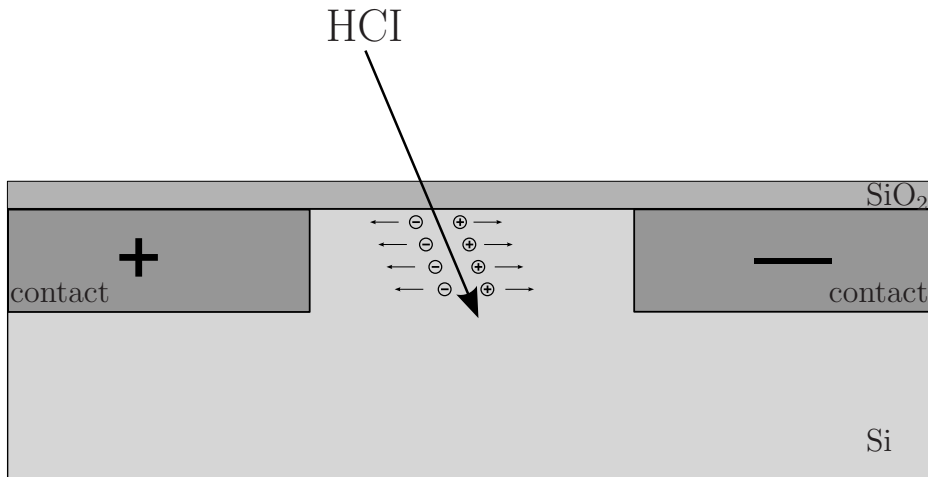


Figure 7.4: IBIC detector using standard MOSFET technology.

et al. [Jamieson *et al.*, 2005]. In their setup two gates are used to collect the electron/hole pairs. On the rear side of the wafer a n-gate is formed and next to the implantation region p-wells are created forming a p-i-n structure. With this setup they were able to detect 14 keV phosphorus ($^{31}\text{P}^+$) ions which were implanted through holes in a resist mask. Although only about a third of the kinetic energy of the ions is used to create electron/hole pairs, which is equivalent to about 1000 electron/hole pairs, they were able to reduce the noise level to a point where 98% detection efficiency was achieved. The challenge in their setup is to be able to address different holes in the resist with a focused ion beam without the use of a scanning probe. This will be particularly challenging if the holes are only about 20 nm apart.

7.2 Possible Improvements of the Scanning Probe

The setup of the scanning probe still has many opportunities for improvement. In the following several are discussed.

7.2.1 Vibration isolation

At the moment no vibration isolation is implemented at all. It is indeed surprising that usable data on the nanometer scale can nevertheless be measured. The ideal situation would be to have the scanning probe completely isolated, but because of the integration into the beamline this is not possible. Also, the mounting of the whole beamline onto a vibration isolated table is not feasible, although in theory doable. Easier to implement is an exchange of the turbo-molecular pumps with ion pumps. Suspending the stage on springs would also be an option which is often used for SPM setups, or the stage could be mounted with some rubber-like material such as Viton to suppress vibrations.

7.2.2 Lock-in read-out

To reduce the electrical noise that is being picked up, the bridge could be read out using a lock-in amplifier. For this the bridge would be biased with an alternating current (AC)-signal rather than a constant voltage. The response of the bridge would then also be a signal with the same frequency and a rms-signal could be generated by a lock-in amplifier, excluding all other frequency components.

7.2.3 Non-contact mode

Implementing non-contact or tapping mode read-out would be another improvement of the SPM. On the one hand it would greatly reduce the force that the tip exerts on the sample and on the other it also provides a way to increase the scan speed. To include non-contact or tapping mode would require some major modifications of the setup. This would start with the need to use cantilevers equipped with actuators which force the beam of the cantilever to oscillate. Furthermore, a supply voltage from a function generator would be needed for the actuator, which would require a redesign of the vacuum connectors. The electronics would also need to be changed and a lock-in amplifier would need to be added to the system.

7.2.4 Smaller feature size

To further reduce the feature size, and therefore increase the resolution of the implanted region, two steps are necessary. Firstly the resist control has to be fine tuned. Factors such as temperature and development time can be optimized and are known to play an important role in achieving high

resist resolution. Secondly smaller holes in the cantilever have to be made and tested. A possible scheme to obtain reproducible high aspect ratio holes with a small diameter is the integration of nanotubes into the cantilever. One way of implementing this is to use a FIB to weld the tubes into a pre-drilled hole. Using the FIB directly would also be possible, although high aspect ratios would not be achievable and drilling reproducible holes would also be a very challenging task.

Chapter 8

Similar Work & Future Developments

SPMs have always been used to not only image surfaces, but also to modify them. Many of these applications use the tip to modify the surface structure or to move, for example, single atoms or molecules on the surface. Often this involves biasing the tip at different voltages and using the electric field that is created for different purposes, for example, to oxidize thin metal layers or remove single hydrogen atoms on a hydrogen-terminated silicon surface.

Other approaches do not rely on the use of the tip, but use a hole in the cantilever as a mask, as done in the experiments described here. In the following some projects using cantilevers as masks are reviewed and some on-going and future experiments are mentioned.

8.1 Scanning Probes without Ion Beams

8.1.1 Material deposition

In 1999 Lüthi *et al.* demonstrated a resistless lithography technique by combining an atomic-molecular beam with a SPM [Lüthi *et al.*, 1999]. They use a standard optical readout for the SPM and an evaporation source that is mounted about 6 cm from the target to create the atomic-molecular beam. Furthermore a 2 mm aperture was used to pre-collimate the beam. By evaporating copper they were able to deposit metal lines onto a silicon wafer with a minimum line width of 70 nm and a height of several tens of nanometers.

Egger *et al.* report a very similar approach [Egger *et al.*, 2005]. Their setup includes several different material sources which enables them to create, for example, copper, nickel and even C₆₀ beams.

8.1.2 Localized etching

Rangelow *et al.* designed a nano-nozzle to transport neutral radicals generated by a plasma discharge to specific points on a surface [Rangelow *et al.*, 2001]. The radicals were used to create localized etching patterns on the target. In addition, the nozzle could be used as an AFM tip. Using this technique fluorine radicals were used to etch 900 nm wide lines into silicon with a nozzle opening of 700 nm.

8.2 Scanning Probes with Ion Beams

The work in this thesis presents the first integration of a SPM with an ion beam. The idea though, is not a new one. The concept of using a scanning probe with an integrated hole as a movable mask was published by Jamieson *et al.* [Jamieson *et al.*, 2003] in the same context as finding a way to implant single ions for building a QC.

In the last years two new ideas were proposed using a scanning probe to position or implant ions or clusters. They are in the process of being realized at the time of writing this thesis and are introduced below. Both of them use the same setup for the scanning probe, but other ion species than HCl⁺s.

8.2.1 Cluster jet

Meijer *et al.* are building a cluster source to be able to place nano particles with a resolution better than 10 nm using a scanning probe approach. This is to be achieved by creating a nano particle ion beam and then using a pierced cantilever to position the very slow particles on a surface [Meijer *et al.*, 2005].

8.2.2 Single atoms via ion traps

Schmidt-Kaler *et al.* at the University of Ulm, Germany are working on using a Paul trap as source of single ions which would then be focused through a pierced AFM tip and implanted into a target material [Meijer *et al.*, 2006]. The idea is to avoid the need for a single ion detector by making sure that the trap is only loaded with a single ion to begin with. The FIB-pierced AFM tip would be used in the same way as in our setup, but the tip would only have the function of positioning the target correctly and not be a beam-limiting aperture. By integrating an Einzel lens into the cantilever, the group showed simulations that would enable an implantation resolution of 1 nm, not including straggling effects from the implantation process.

Chapter 9

Conclusions

The development of a new technique for the alignment of ion beams to areas of interest has been shown. Currently the spot size is limited to 120 nm, however, the ultimate resolution for this approach is a few nanometers. The AFM tip can be aligned with 10 nm precision and this technique enables precision doping of selected areas.

The alignment is achieved by scanning probe technology, which enables imaging of the surface without disturbance of it. In particular, no ions are implanted during imaging, as for example is the case when scanning with the ion beam of a FIB. In addition, the problem of aligning the ion beam with the electron beam, as in the dual beam FIB, does not exist: The ion beam in our setup needs no special alignment and the final resolution is given by just one aperture in close proximity to the surface. Another advantage compared to a FIB is the relative ease of changing the ion species.

Using the tip of the cantilever in contact mode can result in unwanted surface modifications, for example scratching of the surface. This can be avoided by using a lower contact force which is the current limiting factor of the machine. Another option would be to use the scanning probe in non-contact mode or tapping mode, which was already achieved with piezo-resistive cantilevers by periodically heating the cantilever beam to achieve a resonant vibration. In non-contact mode the sample can be scanned and the tip can be positioned without any modification of the sample. Further improvements include better vibration isolation.

In parallel a single ion detection technique for integration into the setup is being developed using either secondary electrons or electron/hole pairs, enabling the implantation of one and only one ion at a precise location. This will not only allow the implantation of single atoms to produce quantum computer test structures as laid out in the beginning chapters of this thesis, but will also open up possible experiments to investigate the effects of the

statistical distributions of bulk implants used in the semiconductor industry. These are starting to play an increasingly important role as the line width in the production of standard transistors becomes smaller and smaller.

In summary, the results of a working prototype of an ion implanter with scanning probe alignment have been shown and the necessary steps for future improvement of the system towards the design goal of an implantation accuracy of several nanometers have been presented.

Chapter 10

German Summary — Zusammenfassung

10.1 Einführung und Motivation

Die Implantation von Ionen ist eine der grundlegenden Techniken in der heutigen Halbleitertechnologie und dient zum Beispiel zur Herstellung von Transistoren. Die Standardverfahren zur lokalen Dotierung von Halbleitern benutzen Diffusion- oder Implantationsverfahren durch eine lokal definierte Maske. Bei beiden Verfahren kommt es hierbei zu einer statistischen Verteilung des zur Dotierung verwendeten Materials. Speziell für die Halbleitertechnologie werden Effekte, die durch die statistische Verteilung der Dotieratome entstehen in naher Zukunft eine immer größere Rolle spielen. Die Fähigkeit, einzelne Atome mit hoher Ortsgenauigkeit in einem beliebigen Material platzieren zu können, ist daher sehr wünschenswert. Weiterhin werden sich dadurch auch neue Anwendungsgebiete erschließen. Es existieren zum Beispiel verschiedene Vorschläge zur Realisierung von Quanten-Computern in Silizium, die die genaue Platzierung einzelner Atome voraussetzen.

Quanten-Computer besitzen die Fähigkeit, bestimmte Probleme, unter anderem die Faktorisierung großer Zahlen, wesentlich schneller lösen zu können als klassische Computer. Weiterhin können Quanten-Computer auch für die Simulation von physikalischen Problemen eingesetzt werden. Zur Realisierung von Quanten-Computern wird die Platzierung von einzelnen Atomen in einem Abstand von ca. 20 nm in zum Beispiel Silizium benötigt. Weiterhin ist es notwendig, dass jeweils nur genau ein Atom implantiert wird.

Das Projekt am E.O. Lawrence Berkeley National Laboratory, an dem diese Arbeit durchgeführt wurde, befasst sich mit der Herstellung von Teststrukturen für Quanten-Computer. Ein Einzelionen-Implantationsverfahren

mit hoher Ortsauflösung ist daher Teil der benötigten Infrastruktur zur Realisierung des Projektes. In dieser Arbeit wird ein Teilaspekt hierzu betrachtet und ein Implantationsverfahren mit einer hohen Ortsauflösung entwickelt. Dabei werden auch schon Aspekte für die spätere Einzelionendetektion berücksichtigt.

10.2 Hochgeladene Ionen

Die Platzierungsgenauigkeit von einzelnen Ionen wird durch die Streuung des Implantationsprozesses limitiert. Um die Streueffekte zu reduzieren, muss die Implantationsenergie gering gehalten werden. Dies führt jedoch gleichzeitig dazu, dass die Detektion einzelner Atome bei der Implantation schwieriger wird, da weniger Energie zur Verfügung steht, die in einem Detektor nachgewiesen werden kann.

Eine elegante Möglichkeit diesem Problem zu entkommen, besteht in der Benutzung von hochgeladenen Ionen, da diese selbst bei geringer kinetischer Energie noch ihre volle potentielle Energie besitzen, die durch die mehrfache Ionisation zustande kommt.

Diese potentielle Energie wird hauptsächlich direkt beim Aufprall, beziehungsweise in den ersten Nanometern innerhalb des Targetmaterials frei. Ein nachfolgendes Aktivieren der Dotieratome ist in der Lage den Schaden im Kristallgitter, der durch die Implantation entsteht, sowie den Schaden, der durch die extra potentielle Energie hochgeladener Ionen entsteht, zu reparieren, wie zum Beispiel Ergebnisse im Anhang dieser Arbeit zeigen. Die potentielle Energie wird dabei, je nach Energie der Ionen, zur Erzeugung von Elektron-Loch Paaren und Fehlstellen im Kristall umgesetzt. Weiterhin werden je nach Material viele Sekundärelektronen an der Oberfläche erzeugt und freigesetzt.

Die Erzeugung hochgeladener Ionen mit einer relativ geringen Energie wird in einer *Electron Beam Ion Trap (EBIT)* realisiert. Dieses Verfahren stellt eine kompakte Anlage dar, höchstgeladene Ionen zu erzeugen. Die prinzipielle Arbeitsweise kann wie folgt zusammengefasst werden: Die Erzeugung hochgeladener Ionen wird durch die wiederholte Stoßionisation von Atomen/Ionen erreicht. Hierzu wird eine Ionenfalle verwendet, in der die Ionen durch einen Elektronenstrahl mit entsprechender Energie durch Stoßprozesse weiter aufgeladen werden. Die Ionenfalle selbst wird dabei durch den verwendeten Elektronenstrahl realisiert, der die Ionen radial einfängt, und durch drei Elektroden, die eine longitudinale Falle erzeugen (siehe Abbildung 3.2, Seite 14). Der Elektronenstrahl wird hierzu durch zwei superleitende Helmholtzspulen gebündelt, um die benötigte Stromdichte zu errei-

chen. Die Extraktion des Ionenstrahles kann nun auf zwei Arten erfolgen: zum einen, kann die Falle durch die drei Elektroden so eingerichtet sein, dass die Ionen, wenn sie genügend kinetische Energie besitzen, bevorzugt durch die obere Elektrode entweichen, oder das Potential an den Elektroden kann so geschaltet werden, dass die Konditionen für eine Ionenfalle kurzfristig aufgehoben werden und alle Ionen durch die obere Elektrode extrahiert werden.

Der Ionenstrahl wird dann durch eine Strahlführung gebündelt und zum Experiment geleitet (siehe Abbildung 3.3, Seite 16). Teil der Strahlführung ist ein 90° Ablenkmagnet, mit dem ein spezifisches Massenladungsverhältnis aus dem Ionenstrahl ausgewählt werden kann. Hierdurch wird sichergestellt, dass nur Ionen eines bestimmten Isotopes und einer bestimmten Ladung für das Experiment verwendet werden.

10.3 Rasterkraftmikroskop

Die benötigte Platzierungsgenauigkeit soll durch die Integration eines Rasterkraftmikroskops erreicht werden. Der Cantilever wird hierbei zu einer bewegbaren Lochblende umfunktioniert. Ähnliche Verwendung von Cantilevern existieren schon (zum Beispiel zur lokalen Materialabscheidung oder zum lokalen Ätzen), die Integration mit einem Ionenstrahl ist jedoch neu.

Der Aufbau des benutzen Rasterkraftmikroskops wird in Abbildung 4.2 (Seite 32) gezeigt. Die Besonderheit dieses Aufbaus ist das Auslesen der Ablenkung des Cantilevers mittels piezoresistiven Elementen im Gegensatz zu dem häufiger verwendeten Aufbau mittels Laserreflektion. Hierbei werden spezielle Cantilever verwendet, die eine Brückenschaltung mit piezoresistiven Widerständen integriert haben. Das Rasterkraftmikroskop wird im Kontakt-Modus betrieben, in dem die Spitze des Cantilevers das Material berührt. Die Brückenschaltung wird dafür vor dem Zustandekommen des Kontakts zwischen Material und Spitze abgeglichen. Das Signal von der Brückenschaltung während der Messung wird durch zwei Vorverstärker in die Steuerelektronik eingespeist. Während der Messung wird das Signal dann durch eine Rückkopplung von der Steuerelektronik konstant gehalten.

Zwei verschieden Typen von Spitzen für die Cantilever wurden benutzt. Zum einen wurden Spitzen von kommerziell erwerblichen Proben benutzt (siehe Abbildung 4.5, Seite 36) und zum anderen eigene Spitzen mittels Platiniumabscheidung in einem *Focused Ion Beam*-System selbst erstellt (siehe Abbildung 4.4, Seite 35). Weiterhin wurden in die Cantilever Löcher mit verschiedenen Radien ebenfalls mit dem *Focused Ion Beam*-System gebohrt. Hierbei wurden Löcher mit Radien bis zu 5 nm Durchmesser erreicht (siehe Abbildung 4.6, Seite 37).

Da das Rasterkraftmikroskop in die Strahlführung der Ionenquelle eingebaut wird, wird die mechanische Isolation des Systems wesentlich erschwert. Normalerweise werden Rasterkraftmikroskope auf vibrationsisolierten Tischen installiert, so dass keine mechanischen Schwingungen die Messung stören kann. Aufgrund einer einfacheren Integration des Mikroskops mit der Strahlführung wurde auf eine mechanische Isolierung verzichtet, so dass mechanische Schwingungen ein größeres Rauschen in dem Signal erzeugen. So ließ sich der Einfluss von zum Beispiel der nächstgelegenen Turbomolekularpumpe deutlich messen. Nichtsdestotrotz konnte ein Rauschpegel von ca. 1 nm in vertikaler Richtung erreicht werden (siehe Abbildung 4.11, Seite 42 und Abbildung 4.12, Seite 43).

Die Messung der lateralen Auflösung konnte nur durch den Vergleich mit einer Messung eines kommerziellen Rasterkraftmikroskops erreicht werden. Hier konnte kein Unterschied in der lateralen Auflösung festgestellt werden und aufgrund der verwendeten Teststrukturen wurde eine laterale Auflösung von ca. 10 nm bestimmt (siehe Abbildung 4.14, Seite 44). Die kleinsten gemessenen Strukturen (Abbildung 4.15, Seite 45) bestehen aus 50 nm weiten Furchen.

Zusammenfassend kann gesagt werden, dass die Auflösung des Rasterkraftmikroskops ausreichend ist, da die Platziergenauigkeit der zu implantierenden Ionen gegeben durch den Lochradius im Cantilever und der Streuungenauigkeit größer ist. Eine Verbesserung des Aufbaus durch eine bessere mechanische Isolierung bietet weiterhin die Möglichkeit die Auflösung wesentlich zu verbessern, falls zukünftige Anwendungen dieses verlangen.

10.4 Experimenteller Aufbau

Für die experimentelle Realisierung des Aufbaus wurde das Rasterkraftmikroskop in die Strahlführung integriert (siehe Abbildung 5.1, Seite 50). Hierzu wurde der Ionenstrahl mittels mehreren Lochblenden auf einen Durchmesser von maximal 1 mm beschränkt. Der Cantilever befindet sich direkt hinter der letzten Lochblende der Strahlführung und kann durch eine Vorrichtung in X, Y und Z genau platziert werden. Ein Stück Silizium wird als Target auf einem Nano-Positionierer, der auch zum Scannen benutzt wird, platziert. Zum Testen der Implantation werden Siliziumstücke mit zwei verschiedenen Photolacken benutzt. Hierbei kamen Polymethylmetacrylat und Wasserstoffsilsesquioxan zum Einsatz. Weiterhin wurde von zwei Ionenquellen Gebrauch gemacht. Zum einen die weiter oben beschriebene Quelle für hochgeladene Ionen und zum anderen eine Quelle für niedrig geladene Ionen mit Energien im Bereich einiger Kilo-Volt. Letztere Quelle fand Verwendung, da der hiermit

erzeugte Ionenstrahl zur Belichtung des Photolackes ausreichend war und die Quelle wesentlich einfacher aufgebaut ist und daher eine höhere Verfügbarkeit hatte (zum Beispiel entfiel das Kühlen mit flüssigem Helium). Der Nachteil der zweiten Ionenquelle besteht in einer wesentlich schlechteren Strahlqualität, die jedoch für diese Versuche ausreichend war.

10.5 Ergebnisse

In beiden Photolacken konnten mittels der Lochblende in dem Cantilever verschiedene Muster mit dem Ionenstrahl definiert werden. Um bessere Ergebnisse zu erzielen wurde eine weitere Lochblende in die Strahlführung integriert, um die Strahlqualität der niedergeladenen Ionenquelle zu verbessern (geringere Winkelstreuung). Es gelang Muster mit minimalen Linienbreiten von 300 nm und 120 nm zu definieren (siehe Abbildung 6.1, 6.2, 6.4, Seite 56 ff.). Weiterhin wurden lokal hochgeladene Ionen implantiert (siehe Abbildung 6.5, Seite 60). Hierbei konnten in dem Photolack direkt einzelne Ionen registriert werden.

10.6 Ausblick

Verschiedene Möglichkeiten bestehen, den existierenden Aufbau zu verbessern. So kann eine Vibrationsisolierung integriert werden, um die Auflösung des Rasterkraftmikroskops zu verbessern. Weiterhin kann das Rasterkraftmikroskop im sogenannten *non-contact* Modus betrieben werden, was eine Beschädigung des Targetmaterials durch die Spitze vollkommen ausschließen würde.

Der Weg zu kleineren Linienbreiten hängt hauptsächlich von der Erzeugung kleinerer Lochblenden in dem Cantilever ab. Hier bietet die Integration von Nano-Röhrchen in den Cantilever eine interessante Alternative zu der verwendeten Methode.

Weiterhin wird an der Integration eines Einzelionendetektors gearbeitet. Hierbei bieten sich zwei Nachweismethoden an. Sekundärelektronen, die beim Auftreffen der hochgeladenen Ionen entstehen, können mittels eines elektromagnetischen Feldes zu einem Detektor gelenkt werden oder die im Material erzeugten Elektron-Loch Paare können zur Detektion benutzt werden. Hierzu müsste eine Diodenstruktur in das Targetmaterial integriert werden.

Zusammenfassend kann gesagt werden, dass eine neue Methode zur lokalen Ionenimplantation bereitgestellt wurde, mit der eine Positionierungsgenauigkeit von 120 nm demonstriert wurde. Eine Verringerung dieses Wertes

zu einigen Nanometern sollte möglich sein, wobei das Limit durch die Streuung des Ions im Targetmaterial gegeben ist. Durch die Integration eines Einzelionendetektors wird unter anderem die Untersuchung von statistischen Effekten in der Halbleitertechnik möglich, was ein weiteres interessantes Anwendungsgebiet erschließen würde.

Appendix A

Spin measurements on implanted samples

Using a single ion implanter to position atoms in silicon for quantum computing is only useful if those atoms can be electrically activated and if the spins of those atoms have a long decoherence time. The decoherence time for donors in silicon is well known and its length is one of the reasons to pursue this approach. However, it is also well known that defects in the material and the presence of other spins close to the donor lead to shorter decoherence times. So the questions are, can each donor be activated and can the damage done during the implantation process be repaired so that the observed long decoherence times are reached for every atom?

In standard CMOS processes the activation is not a critical issue, since the dose can normally be adjusted to achieve a certain number of activated donors. For quantum computing on the other hand this is not an option, since every extra non-activated donor will be a source of decoherence and for the proposals out today one needs to have a very high percentage of activated donors to be able to use the direct neighbor interaction as one of the main sources of information processing. Furthermore, we know from Chapter 3 that HCIs deposit more energy at the surface and in the material than singly charged ions: Will this lead to extra damage that cannot be repaired?

Most of these issues can be resolved by studying bulk implanted samples, that is without the use of a single ion implanter. Therefore, experiments have been carried out to show that high activation and long decoherence times can indeed be achieved using HCIs. In this appendix a very short review of this work is given. Most of the sample preparation was done by our group at LBNL. The Electron Spin Resonance (ESR) experiments themselves were done by Steve Lyon's group at Princeton.

A.1 Quick Review of some ESR Basics

For spin systems there are two important decoherence times. The longitudinal relaxation time, T_1 , and the transverse relaxation time, T_2 . The first describes the spin flip probability of a spin aligned to an external magnetic field and the second can be viewed as a dephasing time for spins rotating in a plane transverse to an external magnetic field.

Both of the decoherence times can be measured using pulsed ESR, in which a strong magnetic field is used to split the energy level of the spin system and then electromagnetic pulses are used to rotate the spins.

Inversion recovery can be used to measure T_1 . In equilibrium the distribution of spins depends on the temperature and the energy gap between different spin states created by the strong static magnetic field. The actual distribution is given by a Boltzmann distribution. By applying the correct electromagnetic pulse this distribution can be inverted and the system will no longer be in equilibrium. The system then relaxes over time and recovers its equilibrium state. If one now applies a second pulse after a certain time τ that rotates the spins in the transverse plane to the magnetic field, an ESR experiment will be able to pick up the amplitude of the sum of the spins (and therefore the difference in population of the energy levels) that now rotate around the magnetic field axis. Due to further decoherence this amplitude will diminish, but nevertheless the amplitude at the time the second pulse was passed can be reconstructed. During the time τ a certain amount of spins will relax back to the lower energy state, the amount of those spin flips is characterized by T_1 . So by mapping the amplitude against the time τ one can measure T_1 . The pulse sequence is shown in Figure A.1.

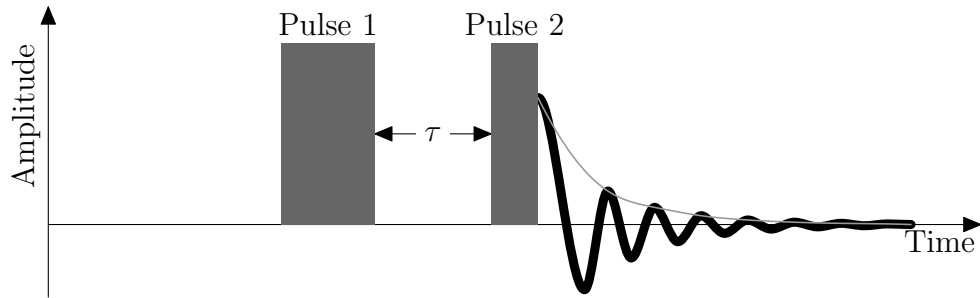


Figure A.1: Measurement of the spin-flip relaxation time T_1 .

The transverse relaxation time is related to the line width of an ESR absorption line. However, just measuring the line width would also include several unwanted decoherence effects, as for example non-uniformity of the applied magnetic field or strain in the material. The so called *spin echo*

technique resolves these issues. Here, spins are rotated into the transverse plane with respect to the magnetic field and after a time τ a second pulse is applied that mirrors the spin in a plane perpendicular to the plane they are in, for example the X or Y plane (assuming a magnetic field in the Z direction). Each spin will rotate at a slightly different angular velocity due, for example, to different g -factors because of strain or slightly different local magnetic fields because of non-uniformities. By applying the second pulse, the pulses that went “too fast” will now suddenly be behind the pulses that were slower and after another time τ the spins will line up again and create a spin echo that can be picked up by the ECR machine. This way all decoherence sources that lead to a different, but static, angular velocity can be excluded and only T_2 will be measured. A schematic of the process is shown in Figure A.2.

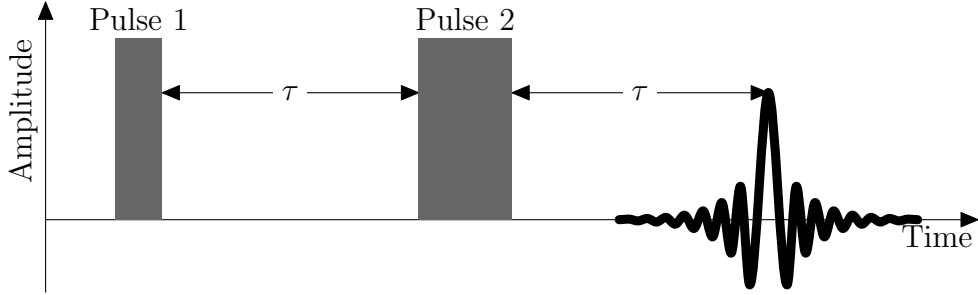


Figure A.2: Measurement of the spin relaxation time T_2 using spin echos.

Apart from the relaxation times, the total number of spins can also be measured and in our case an activation ratio can be calculated from this value.

A.2 Measurements and Results

For the experiment low dose bismuth ($2 \times 10^{11}/\text{cm}^2$) was implanted with the EBIT into isotopically enriched silicon. This was done so that the measured decoherence times are not influenced by ^{29}Si spins. Afterwards the samples were annealed for several seconds at 1000°C . The depth profile before and after annealing was measured by Secondary Ion Mass Spectroscopy (SIMS) and Spreading Resistance Analysis (SRA) and the relaxation times were measured at 5.2 K . The effect of the surface was also analyzed, by stripping the oxide layer and passivating the surface with hydrogen before further ESR measurements. A more detailed description of the experiment can be found in [Schenkel *et al.*, 2005]. The results of the SIMS and SRA measurements are shown in Figure A.3 and Figure A.4 One spin relaxation measurement

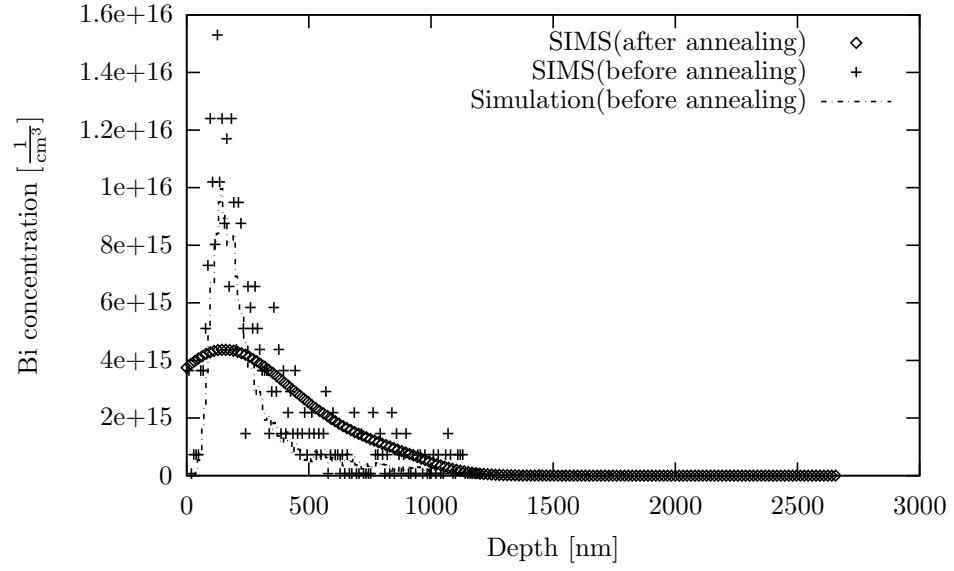


Figure A.3: SIMS measurements of bismuth implanted at 400 keV before and after annealing together with the results of a simulation.

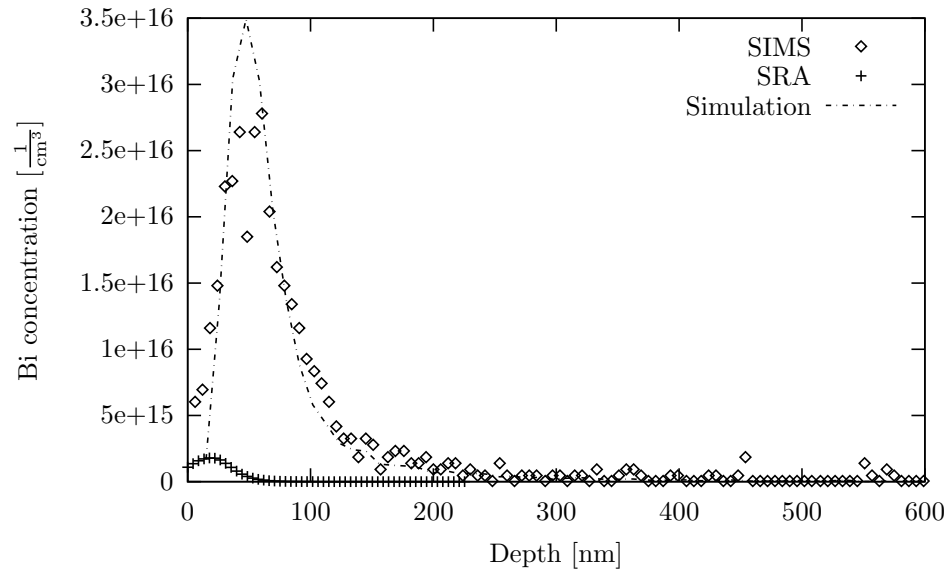


Figure A.4: SIMS and SRA measurements of bismuth implanted at 120 keV after annealing together with a simulation.

is shown in Figure A.5. Here the spin relaxation time T_2 was measured for a 400 keV implant of $2 \times 10^{11}/\text{cm}^2$ bismuth. The sample was annealed under the aforementioned conditions and the measurement was carried out at the spin $M = +\frac{1}{2}$ line at 5.2 K. Over longer periods the measurement becomes unreliable because of instabilities in the magnetic field. As a result the fit was generated from the data with $\tau < 0.6$ ms, and a relaxation time of $T_2 = 2.1$ ms was measured. The results are summarized in Table A.1. As

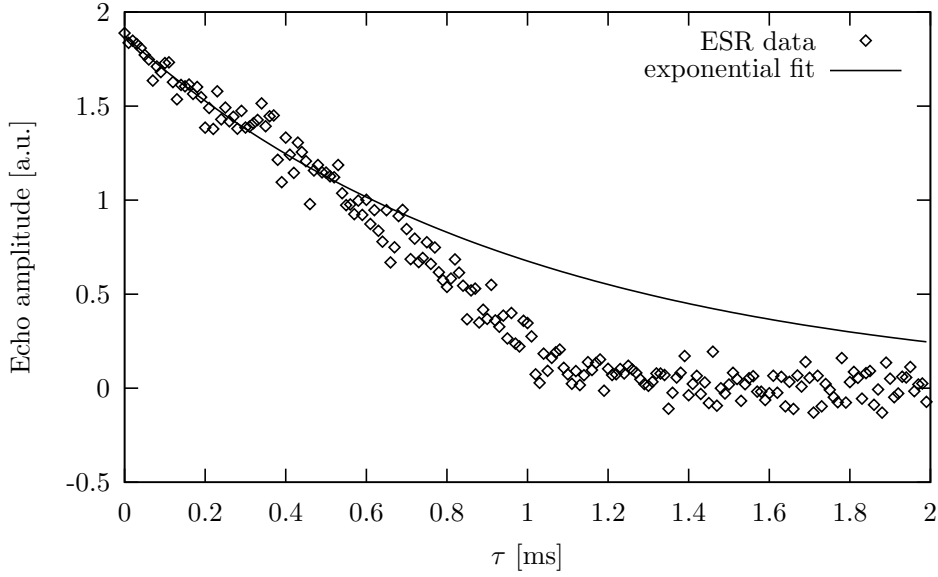


Figure A.5: Spin relaxation time T_2 measurement with ESR on a sample implanted with bismuth at 400 keV.

Interface	Energy [keV]	T_1 [ms]	T_2 [ms]
SiO ₂ /Si	120	14 ± 2	0.30 ± 0.03
H/Si	120	16 ± 2	0.75 ± 0.04
SiO ₂ /Si	400	16 ± 1	1.5 ± 0.1
H/Si	400	14 ± 1	2.1 ± 0.1

Table A.1: Spin relaxation times measured at 5.2 K.

the table shows, long decoherence times were measured for the samples. A surface effect can be clearly seen, which is probably due to defects and traps at the interface. An increase in the decoherence time for the H-Si interface,

which is known to have fewer defects than a SiO_2 -Si interface, also confirms this.

The activation was found to be 100% within the error of the measurements. The SRA analysis for the low energy implant, however, showed almost no activation. This is probably due to ionization of the donors because of band bending near the interface, which can then no longer be measured by SRA but could, on the other hand, be resolved by ESR by using sample illumination.

Defects created during the implantation step should thus not hinder the use of implantation for creating single ion qubits in silicon. Further tests of the influence of gates on the implanted spins are discussed in the paper by Bradbury *et al.* [Bradbury *et al.*, 2006].

List of Figures

2.1	Circuit diagram for the Deutsch-Josza algorithm.	5
2.2	Kane's proposal for a solid state quantum computer using phosphorus spins in silicon. A magnetic field is used to address the spin states and top gates are used to control the interaction.	8
3.1	Concept of an EBIT.	13
3.2	The drift tubes generating the axial trap for the ions in addition to the radial trapping by the electron beam.	14
3.3	The EBIT beamline at LBNL.	16
3.4	Separating different charge states of a bismuth beam extracted at 3.5 kV using the bending magnet.	18
3.5	Two knife-edges are used to measure the emittance of the beam.	19
3.6	Measured emittance of an Ar^{14+} beam.	19
3.7	HCI above a surface.	21
3.8	Potential distribution for a HCI at the critical distance for resonant electron capture close to a metal surface.	22
3.9	Stopping powers of bismuth and phosphorus in silicon.	24
4.1	SPM setup using a laser readout.	29
4.2	Schematic setup of the piezo-resistive SPM.	32
4.3	Photo of the SPM setup in the 8 in. cube taken through one of the viewports in the cube.	33
4.4	Self-grown tip by ion beam assisted deposition.	35
4.5	Piezo-resistive cantilever with a glued on commercial tip.	36
4.6	TEM image of a FIB-drilled hole in a silicon nitride membrane.	37
4.7	Cantilever with three FIB-drilled holes, two of them closed down by local platinum deposition. The sizes of the holes are 100 nm, 3 μm and 300 nm (top to bottom).	38
4.8	A typical noise spectrum taken under high vacuum conditions in contact mode.	40

4.9	Effect of the turbo pump spinning down on the noise spectrum. The noise level is given in $\text{V}/\sqrt{\text{Hz}}$	41
4.10	Force-distance curve with turbo pump on.	42
4.11	Force-distance curve with turbo pump off and filtering of the signal.	42
4.12	Line scan of a calibration sample with 20 nm steps.	43
4.13	3D-image of a calibration sample.	43
4.14	Comparison of the lateral resolution of our AFM (<i>in situ</i>) with a commercial AFM (<i>ex situ</i>). The inset shows a 3D-scan of the sample taken with our AFM.	44
4.15	50 nm wide trenches imaged with the our AFM.	45
4.16	Repeated line scan to determine the drift in the setup.	46
4.17	Commercial tips: A new tip (left) and a used tip (right).	46
4.18	A commercial tip before (left) and after (right) refurbishment.	47
5.1	Experimental setup.	50
5.2	The structure of HSQ.	51
6.1	<i>Ex situ</i> AFM image of a developed lithographically defined pattern using an argon beam in PMMA.	56
6.2	<i>Ex situ</i> AFM image of a developed lithographically defined pattern using an argon beam in HSQ.	57
6.3	Different lithographic images in PMMA resist.	58
6.4	Zoom of Figure 6.3 showing a pattern defined by moving the ion beam across the target at a speed of 50 nm/s	58
6.5	Single ion hits of Xe^{30+} implanted through a $3 \mu\text{m}$ hole in the cantilever.	60
6.6	Cross section of a single ion hit of a HCl. The insert shows the AFM scan from which the cross section was taken.	60
7.1	Setup for single ion detection with integrated detection.	64
7.2	Spectrum due to secondary electrons on the PMT without the SPM in place, with the ion beam turned on and off.	65
7.3	Spectrum from the PMT with the SPM setup. Multiple elec- tron events are seen with the SPM retracted, but only single electron events show up with the SPM in place. A background noise spectrum with the beam off is also shown.	66
7.4	IBIC detector using standard MOSFET technology.	67
A.1	Measurement of the spin-flip relaxation time T_1	82
A.2	Measurement of the spin relaxation time T_2 using spin echos.	83

A.3	SIMS measurements of bismuth implanted at 400 keV before and after annealing together with the results of a simulation. .	84
A.4	SIMS and SRA measurements of bismuth implanted at 120 keV after annealing together with a simulation.	84
A.5	Spin relaxation time T_2 measurement with ESR on a sample implanted with bismuth at 400 keV.	85

List of Tables

4.1	Various existing SPMs (incomplete).	28
A.1	Spin relaxation times measured at 5.2 K.	85

Bibliography

- [ARD, 2004] (2004). A quantum information science and technology roadmap. <http://qist.lanl.gov/>.
- [Aspuru-Guzik *et al.*, 2005] Aspuru-Guzik, A., Dutoi, A., Love, P., and Head-Gordon, M. (2005). Simulated quantum computation of molecular energies. *Science*, 309:1704–1707.
- [Bienoff, 1980] Bienoff, B. (1980). The computer as a physical system: A microscopic quantum mechanical Hamiltonian model of computers as represented by Turing machines. *Journal of Statistical Physics*, 22(5):563–591.
- [Biersack and Ziegler, 2003] Biersack, J. and Ziegler, J. (2003). *SRIM*.
- [Binnig *et al.*, 1986] Binnig, G., Quate, C., and Gerber, C. (1986). Atomic force microscope. *Physical Review Letters*, 56(9):930–933.
- [Binnig *et al.*, 1982] Binnig, G., Rohrer, H., Gerber, C., and Weibel, E. (1982). Surface studies by scanning tunneling microscopy. *Physical Review Letters*, 49(1):57–61.
- [Bradbury *et al.*, 2006] Bradbury, F., Tyryshkin, A., Sabouret, G., Bokor, J., Schenkel, T., and Lyon, S. (2006). Stark tuning of donor electron spins in silicon. *submitted to Physical Review Letters*, cond-mat/0603324.
- [Burgdörfer *et al.*, 1991] Burgdörfer, J., Lerner, P., and Meyer, F. (1991). Above-surface neutralization of highly charged ions: the classical over-the-barrier model. *Physical Review A*, 44:5674–5685.
- [Cirac and Zoller, 1995] Cirac, J. and Zoller, P. (1995). Quantum computation with cold ions. *Physical Review Letters*, 74:4091–4094.
- [Currell, 2003] Currell, F., editor (2003). *The Physics of Multiply and Highly Charged Ions*. Kluwer Academic Publishers.

- [de Sousa *et al.*, 2004] de Sousa, R., Delgado, J., and Sarma, S. D. (2004). Silicon quantum computation based on magnetic dipolar coupling. *Physical Review A*, 70:052304, cond-mat/0311403.
- [Deutsch, 1985] Deutsch, D. (1985). Quantum theory, the Church–Turing principle and the universal quantum computer. *Proceedings of the Royal Society of London: Series A - Mathematical and Physical Sciences A*, 400(1818):97–117.
- [DiVincenzo, 2000] DiVincenzo, D. (2000). The physical implementation of quantum computation. quant-ph/0002077.
- [Donets, 1998] Donets, E. (1998). Historical review of electron beam ion sources. *Review of Scientific Instruments*, 69(2):614–618.
- [Donets *et al.*, 1969] Donets, E., Ilyushchenko, V., and Alpert, V. (1969). Ultrahigh vacuum electron beam source of highly stripped ions. In *Première Conférence sur les Sources d'Ions*, pages 635–642, Saclay, France.
- [Donets and Ovsyannikov, 1981] Donets, E. and Ovsyannikov, V. (1981). Investigation of ionization of positive ions by electron impact. *Journal of Experimental and Theoretical Physics*, 53(3):466–471.
- [Ducrée *et al.*, 1998] Ducrée, J., Casali, F., and Thumm, U. (1998). Extended classical over-barrier model for collisions of highly charged ions with conducting and insulating surfaces. *Physical Review A*, 57:338–350.
- [Egger *et al.*, 2005] Egger, S., Ilie, A., Fu, Y., Chongsathien, J., Kang, D.-J., and Welland, M. (2005). Dynamic shadow mask technique: A universal tool for nanoscience. *Nanoletters*, 5(1):15–20.
- [Feynman, 1982] Feynman, R. (1982). Simulating physics with computers. *International Journal of Theoretical Physics*, 21(6-7):467.
- [Friesen *et al.*, 2003] Friesen, M., Rugheimer, P., Savage, D., Lagally, M., Weide, D. v., Joynt, R., and Eriksson, M. (2003). Practical design and simulation of silicon-based quantum-dot qubits. *Physical Review B*, 67:121301.
- [Gillaspy, 2001] Gillaspy, J., editor (2001). *Trapping Highly Charged Ions: Fundamentals and Applications*. Nova Science Publishers.
- [Gillaspy *et al.*, 1998] Gillaspy, J., Parks, D., and Ratliff, L. (1998). Masked ion beam lithography with highly charged ions. *Journal of Vacuum Science Technology B*, 16(6):3294–3297.

- [Gotszalk *et al.*, 2000] Gotszalk, T., Grabiec, P., and Rangelow, I. (2000). Piezoresistive sensors for scanning probe microscopy. *Ultramicroscopy*, 82:39–48.
- [Gulde *et al.*, 2003] Gulde, S., Riebe, M., Lancaster, G., Becher, C., Eschner, J., Häffner, H., Schmidt-Kaler, F., I.L.Chuang, and Blatt, R. (2003). Implementation of the Deutsch-Jozsa algorithm on an ion-trap quantum computer. *Nature*, 421:48–50.
- [Hägg *et al.*, 1997] Hägg, L., Reinhold, C., and Burgdörfer, J. (1997). Above-surface neutralization of slow highly charged ions in front of ionic crystals. *Physical Review A*, 55:2097–2108.
- [Ivanov *et al.*, 2003] Ivanov, T., Gotszalk, T., Grabiec, P., Tomerov, E., and Rangelow, I. (2003). Thermally driven micromechanical beam with piezoresistive deflection readout. *Microelectronic Engineering*, 67–68:550–556.
- [Jamieson *et al.*, 2005] Jamieson, D., Yang, C., Hopf, T., Hearne, S., Pakes, C., Prawer, S., Mitic, M., Gauja, E., Andresen, S., Hudson, F., Dzurak, A., and Clark, R. (2005). Controlled shallow single-ion implantation in silicon using an active substrate for sub-20-keV ions. *Applied Physics Letters*, 86:202101.
- [Jamieson *et al.*, 2003] Jamieson, D., Yang, C., Pakes, C., Hearne, S., Prawer, S., Stanley, F., Dzurak, A., and Clark, R. (2003). Novel detectors for single atom doping of quantum computer devices.
- [Kane, 1998] Kane, B. E. (1998). A silicon-based nuclear spin quantum computer. *Nature*, 393:113–137.
- [Kane, 2000] Kane, B. E. (2000). Silicon-based quantum computation. quant-ph/0003031.
- [Karapiperis *et al.*, 1985] Karapiperis, L., Dubreuil, D., David, P., and Dieumegard, D. (1985). Ion beam lithography: An investigation of resolution limits and sensitivities of ion-beam exposed PMMA. *Journal of Vacuum Science and Technology B*, 3(1):353–357.
- [Koiller *et al.*, 2001] Koiller, B., Hu, X., and Sarma, S. D. (2001). Exchange in silicon based quantum computer architecture. cond-mat/0106259.
- [Levine *et al.*, 1988] Levine, M., Marrs, R., Henderson, J., Knapp, D., and Schneider, M. (1988). The electron beam ion trap: A new instrument for atomic physics measurements. *Physica Scripta*, T22:157–163.

- [Loss and DiVincenzo, 1998] Loss, D. and DiVincenzo, D. (1998). Quantum computation with quantum dots. *Physcial Review A*, 57:120–126.
- [Lüthi *et al.*, 1999] Lüthi, R., Schlitter, R., Brugger, J., Vettiger, P., Welland, M., and Gimzewski, J. (1999). Parallel nanodevice fabrication using a combination of shadow mask and scanning probe methods. *Applied Physics Letters*, 75(9):1314–1316.
- [Manin, 1980] Manin, Y. (1980). Computable and uncomputable. *Sovetskoye Radio, Moscow*.
- [Marrs *et al.*, 1998] Marrs, R., Schneider, D., and McDonald, J. (1998). Projection x-ray microscope powered by highly charged ions. *Review of Scientific Instruments*, 69:204–209.
- [Meijer *et al.*, 2006] Meijer, J., Vogel, T., Burchard, B., Rangelow, I., Bischoff, L., Wrachtrup, J., Domhan, M., Jelezko, F., Schnitzler, W., Schulz, S. A., Singer, K., and Schmidt-Kaler, F. (2006). Concept of deterministic single ion doping with sub-nm spatial resolution. *Applied Physics A: Material Science & Processing (online issue)*, Feb:1–7, cond-mat/0508756.
- [Meijer *et al.*, 2005] Meijer, J., Wiggers, H., and Rangelow, I. (2005). Cluster-jet addressing of nano-particles to provide functional structures. <http://www.volkswagen-stiftung.de/foerderung/foerderinitiativen/bewilligungslisten/prolcomp.htm>.
- [MicroChem Corp., 2001] MicroChem Corp. (2001). *NANOTMPMMA and Copolymer*. http://www.microchem.com/products/pdf/PMMA_Data_Sheet.pdf.
- [Millar *et al.*, 2005] Millar, V., Pakes, C., Prawer, S., Rout, B., and Jamieson, D. (2005). Thin film resists for registration of single-ion impacts. *Nanotechnology*, 16:823–826.
- [Namatsu *et al.*, 1998] Namatsu, H., Takahashi, Y., Yamaguchi, T., Nagase, M., and Kurihara, K. (1998). Three-dimensional siolcane resist for the formation of nanopatterns with minimum linewidth fluctuations. *Journal of Vacuum Science and Technology B*, 16(1):69–76.
- [Nielsen and Chuang, 2000] Nielsen, M. and Chuang, I. (2000). *Quantum Computation and Quantum Information*. Cambridge Universtity Press.

- [Rangelow *et al.*, 1996] Rangelow, I., Shi, F., Hudek, P., Gotszalk, T., and Grabiec, P. (1996). Fabrication of piezoresistive-sensed AFM cantilever probe with integrated tip. *Proceeding SPIE*, 2879:56–64.
- [Rangelow *et al.*, 2001] Rangelow, I., Voigt, J., and Edinger, K. (2001). Nanojet: Tool for the nanofabrication. *Journal of Vacuum Science and Technology B*, 19(6):2723–2726.
- [Ruehlicke *et al.*, 1995] Ruehlicke, C., Briere, M., and Schneider, D. (1995). AFM studies of a new type of radiation defect on mica surfaces caused by highly charged ion impact. *Nuclear Instruments and Methods in Physics Research B*, 99:528–531.
- [Ryssel *et al.*, 1981] Ryssel, H., Habberger, K., and Kranz, H. (1981). Ion-beam sensitivity of polymer resists. *Journal of Vacuum Science and Technology*, 19(4):1358–1362.
- [Schenkel, 1997] Schenkel, T. (1997). *Zur Wechselwirkung langsamer, hochgeladener Ionen mit Festkörpern: Neutralisation, Energieverlust und Sekundärteilchenproduktion*. PhD dissertation, Johann Wolfgang Goethe-Universität, Frankfurt am Main and Livermore.
- [Schenkel *et al.*, 1999a] Schenkel, T., Barnes, A., Niedermayer, T., Hattass, M., Newman, M., Machicoane, G., McDonald, J., Hamza, A., and Schneider, D. (1999a). Deposition of potential energy in solids by slow, highly charged ions. *Physical Review Letters*, 83:4273–4276.
- [Schenkel *et al.*, 1999b] Schenkel, T., Hamza, A., Barnes, A., and Schneider, D. (1999b). Interaction of slow, very highly charged ions with surfaces. *Progress in Surface Science*, 61:23–84.
- [Schenkel *et al.*, 2003] Schenkel, T., Radmilovic, V., Stach, E., Park, S., and Persaud, A. (2003). Formation of a few nanometer wide holes in membranes with a dual beam focused ion beam system. *Journal of Vacuum Science and Technology B*, 21(6):2720–2723.
- [Schenkel *et al.*, 2005] Schenkel, T., Tyryshkin, A., de Sousa, R., Whaley, K., Bokor, J., Liddle, J., Persaud, A., Shangkuan, J., Chakarov, I., and Lyon, S. (2005). Electrical activation and spin coherence of ultra low dose antimony implants in silicon. *Applied Physics Letters*, 88:112101, cond-mat/0507318.
- [Schneider *et al.*, 1990] Schneider, D., DeWitt, D., Clark, M., Schuch, R., Cocke, C., Schmieder, R., Reed, K., Chen, M., Marrs, R., Levine, M.,

- and Fortner, R. (1990). Ion-collision experiments with slow, very highly charged ions extracted from an electron-beam ion trap. *Physical Review A*, 42(7):3889–3895.
- [Shor, 1994] Shor, P. (1994). Algorithms for quantum computation: discrete logarithms and factoring. In *35th Annual symposium on Foundations of Computer Science*. IEEE Press, Los Alamitos, CA.
- [Shor, 1997] Shor, P. (1997). Polynomial-time algorithms for prime factorization and discrete logarithms on a quantum computer. *SIAM Journal on Computing*, 26:1484–1509, quant-ph/9508027.
- [Skinner *et al.*, 2002] Skinner, A. J., Davenport, M. E., and Kane, B. E. (2002). Hydrogenic spin quantum computing in silicon: a digital approach. quant-ph/0206159.
- [Tortorese *et al.*, 1991] Tortorese, M., Yamada, H., Barrett, R., and Quate, C. (1991). Atomic force microscopy using a piezoresistive cantilever. In *Solid-State Sensors and Actuators, International Conference on Transducers '91*, pages 448–451.
- [Tyryshkin *et al.*, 2003] Tyryshkin, A., Lyon, S., Astashkin, A., and Rait-simring, A. (2003). Electron spin relaxation times of phosphorus donors in silicon. *Physical Review B*, 68:193207.
- [Vandersypen *et al.*, 2001] Vandersypen, L., Steffen, M., Breyta, G., Yannoni, C., Sherwood, M., and Chuang, I. (2001). Experimental realization of Shor’s quantum factoring algorithm using nuclear magnetic resonance. *Nature*, 414:883–887.
- [Vasile *et al.*, 1991] Vasile, M., Grigg, D., Griffith, J., Fitzgerald, E. A., and Russell, P. E. (1991). Scanning probe tips formed by focused ion beams. *Review of Scientific Instruments*, 62(9):2167–2171.
- [Vrijen *et al.*, 2000] Vrijen, R., Yablonovitch, E., Wang, K., Jiang, H., Balandin, A., Roychowdhury, V., Mor, T., and DiVincenzo, D. (2000). Electron-spin-resonance transistors for quantum computing in silicon-germanium heterostructures. *Physical Review A*, 62:012306.
- [Word *et al.*, 2003] Word, M., Adesida, I., and Berger, P. (2003). Nanometer-period gratings in hydrogen silsesquioxane fabricated by electron beam lithography. *Journal of Vacuum Science and Technology B*, 21(6):L12–L15.

Acknowledgments

Here is a (by no means complete) list of people who helped make my stay in Berkeley and this thesis possible and made my whole time in California a lot of fun:

First of all Jürgen Klabunde from GSI in Darmstadt and Ka-Ngo Leung from LBNL, who made it possible for me to work at LBNL. All my colleagues at LBNL: Sami Hahto, Sari Hahto, Frederic Gicquel, Igor Villareal, Jani Reijonen, Hanna Koivunora, Joakim Nilsson, Tak Pui Lou, Qing Ji, Ximan Jiang, Micheal King, Martha Condon, Darlene Hawkins, Parish Epps, Bret van der Akker, Taneli Kalvas, Hannes Vainionpää, Lili Ji. A special thanks to all the people in the EBIT group: Thomas Schenkel, Joon Park, Dieter Schneider, Joe McDonald, Joe Holder, Andreas Krämer, Jason Shangkuan, Arunabh Barta. I would also like to thank Horst Schmidt-Böcking for making it possible to join his group in Frankfurt and for all the warm welcomes in his group. Then there are all the people I met in Berkeley outside the lab. Lots of jugglers and Thursday-night gamers: Theresa Chow, Jeff Zerger, Erika & Lance Thornton, Joe Di Salvo, Marc Hertlein, Sean Brennan, Tom Holub, Peter Ralph, Eva Rittweger, Scott Morrison, Chris Tuffley, Gidon Felsen, Scott McCarey, Jacob Tonski. My landlords Purnima Jha, Maya and Danny Baldonado. The MCB-frisbee bunch: Bryan Lewis, Clinton Wakefield Epps, Sarah Burke, Merek Siu, Joseph Subotnik, James Carl Scott, Daniel Ceperley, Hubert Ho.

Finally my parents Parry & Renate Persaud, my sister Mira Persaud and Frances Allen.

Curriculum Vitae

Personal Data

Name Arun Persaud
D.o.B. 15.3.1975, Frankfurt am Main

Higher Education/ Work experience

2005– Research Associate, Institute of Nanostructure Technologies and Analytics, University of Kassel
2000–2006 Visiting Scholar, E.O. Lawrence Berkeley National Laboratory (LBNL)
2001–2005 Graduate student, Goethe Universität Frankfurt (Prof. H. Schmidt-Böcking)
1995–1999 Student trainee, Gesellschaft für Schwerionenforschung (GSI), Darmstadt
1994–2000 Diplom, Physics at the Tech. Universität Darmstadt
1994–1996 Vordiplom, Mathematics and Physics at the Tech. Universität Darmstadt

Education

1985–1994 Abitur, Augustinerschule Friedberg (Hessen)

Languages German and English

Membership

Microfabrication Laboratory at the University of Berkeley (UCB)
American Physical Society

Computer Experience

Unix, Linux, Windows

C, Fortran(66–95), python, LabView, Php, elisp, SQL

Simion, GPIB programming

Patent

US-Patent-Nr. 6768120 *Focused electron and ion beam systems*

Publications

Arun Persaud, Ka-Ngo Leung, and Jani Reijonen. Compact electron beam focusing column. In *SPIE's 46th Annual Meeting International Symposium on Optical Science and Technology*, page 88, San Diego 4510, 2001.

S. Hahto, K.N. Leung, A. Persaud, and J. Reijonen. A multiaperture electron filter for volume type H^- ion source. *Review of Scientific Instruments*, 73:967–969, 2002.

J. Reijonen, Q. Ji, T.J. King, K.N. Leung, A. Persaud, and S. Wilde. Compact focusing system for ions and electron beams. *Journal of Vacuum Science and Technology B*, 20(1):180–184, 2002.

T. Schenkel, A. V. Hamza, J. P. Holder, K. Krämer, J. W. McDonald, A. Persaud, and D. H. Schneider. Extraction of highly charged ions from the electron beam ion trap at LBNL for applications in surface analysis and materials science. *Review of Scientific Instruments*, 73(2):663–666, 2002.

T. Schenkel, A. Persaud, S. J. Park, J. Meijer, J. R. Kinglsey, J. W. McDonald, J. P. Holder, J. Bokor, and D. H. Schneider. Single ion implantation for solid state quantum computer development. *Journal of Vacuum Science and Technology B*, 20(6):2819–2823, 2002, cond-mat/0201549.

T. Schenkel, J. Reijonen, A. Persaud, A. Krämer, K.N. Leung, R.A. Gough, W.A. Barletta, and E.A. Blakely. A

focused heavy-ion beam system for high-LET studies of cells. *Radiation Research*, 158(3):368, 2002.

T. Schenkel, A. Persaud, S.J. Park, J. Nilsson, J. Bokor, J.A. Liddle, R. Keller, D.H. Schneider, D.W. Cheng, and D.E. Humphries. Solid state quantum computer development in silicon with single ion implantation. *Journal of Applied Physics*, 94(11):7017–7024, 2003.

T. Schenkel, V. Radmilovic, E.A. Stach, S.J. Park, and A. Persaud. Formation of a few nanometer wide holes in membranes with a dual beam focused ion beam system. *Journal of Vacuum Science and Technology B*, 21(6):2720–2723, 2003.

S.J. Park, J.A. Liddle, A. Persaud, F.I. Allen, J. Bokor, and T. Schenkel. Formation of 15 nm scale Coulomb blockade structures in silicon by electron beam lithography with a bilayer resist process. *Journal of Vacuum Science and Technology B*, 22(6):3115–3118, 2004.

S.J. Park, A. Persaud, J.A. Liddle, J. Nilsson, J. Bokor, D.H. Schneider, I.W. Rangelow, and T. Schenkel. Processing issues in top-down approaches to quantum computer development in silicon. *Microelectronic Engineering*, 73–74:695–700, 2004, cond-mat/0310195.

A. Persaud, F.I. Allen, F. Gicquel, S.J. Park, J.A. Liddle, Tzv. Ivanov, K. Ivanova, I.W. Rangelow, J. Bokor, and T. Schenkel. Single ion implantation with scanning probe alignment. *Journal of Vacuum Science and Technology B*, 22(6):2992–2994, 2004.

A. Persaud, S.J. Park, J.A. Liddle, I.W. Rangelow, J. Bokor, R. Keller, F.I. Allen, D.H. Schneider, and T. Schenkel. Quantum computer development with single ion implantation. *Quantum Information Processing*, 3:233, 2004.

T. Schenkel, I.W. Rangelow, R. Keller, S.J. Park, J. Nilsson, A. Persaud, V.R. Radmilovic, P. Grabiec, D.H. Schneider, J.A. Liddle, and J. Bokor. Open questions in electronic sputtering of solids by slow highly charged ions with respect to applications in single ion implanta-

tion. *Nuclear Instruments and Methods in Physics Research B*, 219–220:200–205, 2004.

A. Persaud, J.A. Liddle, J. Bokor, Tzv. Ivanov, I.W. Rangelow, and T. Schenkel. Ion implantation with scanning probe alignment. *Journal of Vacuum Science and Technology B*, 23:2798–2800, 2005.

A. Persaud, S.J. Park, J.A. Liddle, J. Bokor, I.W. Rangelow, and T. Schenkel. Integration of scanning probes and ion beams. *Nanoletters*, 5(6):1087–1091, 2005.

T. Schenkel, A.M. Tyryshkin, R. de Sousa, K.B. Whaley, J. Bokor, J.A. Liddle, A. Persaud, J. Shangkuan, I. Chakarov, and S.A. Lyon. Electrical activation and spin coherence of ultra low dose antimony implants in silicon. *Applied Physics Letters*, 88(11):112101, 2005, cond-mat/0507318.

F.I. Allen, A. Persaud, S.J. Park, A. Minor, M. Sakurai, D.H. Schneider, and T. Schenkel. Transport of multiply and highly charged ions through nanoscale apertures in silicon nitride membranes. *Nuclear Instruments and Methods in Physics Research B*, 244(2):323–326, 2006.

T. Schenkel, J.A. Liddle, J. Bokor, A. Persaud, S.J. Park, J. Shangkuan, C.C. Lo, S. Kwon, S.A. Lyon, A.M. Tyryshkin, I.W. Rangelow, Y. Sarov, D.H. Schneider, J. Ager, and R. de Sousa. Strategies for integration of donor electron spin qubits in silicon. *Microelectronic Engineering*, 83(4–9):1814–1817, 2006.

2006-12-12 Berkeley, California & Kassel, Germany,